A Photo and Thermally Stimulated Luminescence Study of $BaCl_2:Eu^{2+}$ with Application to Neutron Imaging

By

Jeremy Robinson

A thesis
submitted to Victoria University of Wellington
in fulfilment of the
requirements for the degree of
Master in Science
in Physics

Victoria University of Wellington
2008

Abstract

This thesis presents the results of a photo and thermally stimulated luminescence study of europium-doped barium chloride in relation to its potential application as a storage phosphor in glass ceramics for radiation imaging, particularly for neutron imaging. Previous work done on lithium borate (LiBO) glasses containing $BaCl_2:Eu^{2+}$ nanocrystals at Victoria University of Wellington had demonstrated comparable imaging capability with commercially available $BaFBr:Eu^{2+}$ based imaging plates, though the sensitivity and spatial resolution were inferior to that material, and there was a substantial afterglow during the read-out process which degraded any image. These problems are addressed here.

The effect of various different co-dopants on the storage properties was examined using the thermally stimulated luminescence (TSL) technique, with dopants primarily chosen from the alkali and alkaline earth elements. The resulting glow curves have been analysed to determine the activation energies associated with the various traps, and tentative assignments of structural defects to the various glow curve peaks are proposed. It was found that Li^+ and Na^+ gave small increases (20% and 50% respectively) in efficiency, though other dopants tended to reduce the overall output. In particular, K^+ and Rb^+ were found to substantially reduce the output efficiency. It was found that Li^+ co-doped $BaCl_2:Eu^{2+}$ contained thermally unstable traps which at room temperature could result in the observed afterglow in $LiBO/BaCl_2$ glass ceramics through a read-out induced phototransfer process. The experimental measurements required substantial hardware and software development of the existing VUW facilities for TSL, and these improvements are also described here. The most significant improvements are an extension of the operating range at the lower end of the existing TSL spectrometer to -50 °C through a cooled gas flow system, and the engineering of a completely new system to record TSL from 25 K to 400 K.

Acknowledgements

A number of different people have provided me with invaluable support during my time as a Masters student. I would like to especially thank my supervisor A/Prof. Andy Edgar for his support and knowledge in what was initially a brand new subject for me. Also, I'd like to thank Chris Varoy and Dr. James Quilty for their help in different aspects of my work, most significantly in sample preparation and help with the TSL respectively.

Outside of the Radiation and Imaging Group, I'd like to thank J. McClymont for help with anything electrical, A. Rennie and M. Pouajen-Blackiston for the manufacture (and repair!) of a variety of pieces of equipment.

I'd like to thank my family for being there and providing support, especially to my parents who have always encouraged me to chase the things that fascinate me and provided support (and food!) when needed.

I'd like to thank my friends and colleagues at SCPS, especially anyone who has had the good fortune of sharing the 4th floor office with me over the years. I'd like to thank my friends who have had to put up with me during my work and especially to Shelley for all your encouragement and support.

Contents

List of Figures

List of Tables

Chapter 1

Introduction and Background

1.1 Radiation Imaging

Radiation imaging is a projection or shadow imaging technique that can be traced back to the discovery of x-rays by Röentgen in 1895. The traditional method has used a sheet of scintillating material in contact with a photographic film to record an image, representing the spatially distributed radiation intensities that arise when the object to be imaged is placed in an x-ray beam. As atomic number Z is increased, the absorption of x-rays by an element increases, meaning that high-Z (heavy metal elements etc.) are easily distinguished from low-Z light elements) such as carbon, nitrogen, and oxygen). The scintillating material converts the incident x-ray photons into visible light photons which in turn interact with the photographic film, darkening it in areas of high radiation flux. This technique offers a relatively good spatial resolution but suffers from low sensitivity, low dynamic range, and the need for chemical development, which results in each film being single use, increasing long term costs.

Neutron imaging is a newer technique, but is traditionally based on a similar method with photographic film now coupled to a neutron converter material, rather than a scintillator. Incident thermal neutrons interact with the converter material, which typically consist of a neutron-converter isotope such as ^{6}Li, ^{10}B or $Gd^{155/157}$. The nuclear reactions possible are:

$$
\begin{aligned}
^{6}\mathrm{Li} + \mathrm{n} &\rightarrow {}^{3}\mathrm{H}(2.74\mathrm{MeV}) + \alpha(2.05\mathrm{MeV}) \\
^{10}\mathrm{B} + \mathrm{n} &\rightarrow {}^{7}\mathrm{Li}(1.0\mathrm{MeV}) + \alpha(1.8\mathrm{MeV}) \quad (7\%) \\
^{10}\mathrm{B} + \mathrm{n} &\rightarrow {}^{7}\mathrm{Li}(0.83\mathrm{MeV}) + \alpha(1.47\mathrm{MeV}) + \gamma(0.48\mathrm{MeV}) \quad (93\%) \\
^{155}\mathrm{Gd} + \mathrm{n} &\rightarrow {}^{156}\mathrm{Gd} + \gamma(7.9\mathrm{MeV}) + \mathrm{ce's}(0.04\mathrm{MeV} - 0.25\mathrm{MeV}) \\
^{157}\mathrm{Gd} + \mathrm{n} &\rightarrow {}^{158}\mathrm{Gd} + \gamma(8.5\mathrm{MeV}) + \mathrm{ce's}(0.03\mathrm{MeV} - 0.23\mathrm{MeV}) \quad (1\text{-}1)
\end{aligned}
$$

(ce's are resulting conversion electrons)

The secondary radiation (alpha particles, electrons and gamma rays) produced through the nuclear reaction then interacts with the film, again darkening areas in which more radiation is incident. The same problems of low sensitivity etc are present for this system.

Whereas x-ray imaging increases in sensitivity with increasing atomic number, neutrons show substantial sensitivity to lighter elements, especially hydrogen. For materials with large water or oil components this sensitivity is very useful, as x-rays will not provide high contrast images for materials made from low-Z elements. Other common hydrogen-rich materials such as plastics are also amenable to neutron imaging. When used in conjunction with x-ray imaging, the different sensitivities of the two techniques often give complimentary information on the material or object being imaged.

Several newer techniques have been developed to improve neutron imaging, with the goal being to address the problems with photographic film. The technique that is relevant in this study is the use of imaging plates, which use the phenomenon of Photostimulated Luminescence (PSL) to record the image in plates and which show the PSL-generated "Storage Phosphor" effect [1-5].

Current commercially available imaging plates consist of a plastic substrate coated with powdered storage phosphor crystals (for x-ray imaging) or a mixture of storage phosphor and neutron converter (for neutron imaging) distributed evenly over the front surface using an organic binder. For x-ray detection, the incident x-rays

produce electron-hole pairs in the storage phosphor material. Some of these electrons and holes may be left (post-irradiation) in stable 'traps' within the material, where the concentration of the trapped charges represents a latent image of the object of interest.

Neutron imaging with imaging plates works on a similar principle to x-ray imaging, but the powdered storage phosphor is mixed with a neutron converter, typically Gd. Instead of interacting directly with the storage phosphor, incident neutrons react with the converter isotopes producing secondary radiation which then interacts with the storage phosphor material, producing the latent image.

The PSL effect is used to obtain the real image from the latent image recorded on the plates. The imaging pate is placed into a read-out instrument, which uses a raster scanned red or green laser to excite the trapped charges (usually electrons) out of the traps, which then may recombine with holes via a deliberately added luminescent centre, such as Eu^{2+}, producing a shorter wavelength luminescence that may be filtered from the scattered red or green stimulating light. The intensity of this luminescent light is proportional to the original radiation intensity, and the resulting image is recorded digitally. Imaging plates may be erased and re-used many times and require no development chemicals.

Current commercial x-ray and neutron imaging plates use the storage phosphor $BaFBr:Eu^{2+}$ [1], where the electrons are trapped at F^- and Br^- vacancies within the crystal, and the recombination energy is converted to ~400 nm luminescent light via an internal transition of the Eu^{2+} ion. The hole centres have not been unambiguously identified. $BaFBr:Eu^{2+}$ based imaging plates have much better dynamic range (several orders of magnitude better) and slightly better sensitivity than photographic film, but show a decreased spatial resolution due to scattering of the read-out beam by the powdered storage phosphor material. The birefringent nature of the BaFBr makes it impossible to match the refractive index of the organic binder to the phosphor, and the resulting unavoidable mismatch in refractive index causes

scattering of the incident laser beam, meaning a larger area of the imaging plate is excited than intended.

In an effort to reduce the scattering effect and therefore improve the spatial resolution (essentially the sharpness of the image), imaging plates have recently been designed in which the storage phosphor crystals are grown inside a glass matrix. If the crystals are small enough (in the nanometer range) the glass-ceramic is transparent or translucent. Work at Victoria University of Wellington (VUW) has resulted in unique designs for glass-ceramic imaging plates for both x-ray and neutron imaging [5-9].

1.2 Lithium Borate Neutron Imaging Plates

Appleby [7, 9] produced "LiBO" (lithium borate) glass ceramic imaging plates at VUW for use in neutron imaging. The choice of lithium borate glass was based on the relatively large neutron capture cross-section of ^{6}Li (7.5% natural abundance) and ^{10}B (18.8% natural abundance). Since the glass matrix is composed of the neutron converter material, close contact between converter and the incorporated $BaCl_2:Eu^{2+}$ crystals phosphor is ensured. Though the neutron capture cross-sections of ^{6}Li and ^{10}B (941 and 3838 barns respectively) are lower than that of Gd (61000 barns for ^{155}Gd and 255000 barns for ^{147}Gd), the sensitivity of the lithium and boron to gamma rays is also much lower, which is a distinct advantage since most neutron sources are also substantial sources of gamma radiation.

The Fujifilm company produces a $BaFBr:Eu^{2+}$ based imaging plate known as BASND (http://home.fujifilm.com/info/products/science/nd/index.html), where the phosphor powder is mixed in a 1:1 ratio with Gd_2O_3 powder which acts as a neutron converter. There are two neutron sensitive isotopes of Gd, Gd^{157} and Gd^{155}, which together represent roughly 30% of naturally occurring Gd, and both show high sensitivity to neutrons. The BASND powder layers are therefore able to be relatively

thin, which is an advantage for PSL readout as a thinner layer leads to less light scattering.

BASND is a popular neutron imaging option as it shows improvements in all major characteristics except for spatial resolution when compared to photographic film. The reduced spatial resolution is a problem also present in BaFBr based x-ray imaging plates, and is believed to be due to scattering of the stimulating light during image read-out. The high atomic number of Gd and Ba in BASND results in a high sensitivity to gamma rays, and gamma rays originating from the same source as the neutrons may give a ghost image on the plate. To overcome this, significant shielding is usually incorporated when making images using BASND and usually a second image will be made with a Li or B based neutron absorbing screen filtering out incident neutrons, so only the gamma image is present which can then be subtracted from the neutron image.

Glass ceramic neutron imaging plates have the potential to improve on some of the BASND deficiencies, in particular the spatial resolution and gamma ray sensitivity.

1.3 Current Limitations of Lithium-Borate Glass Ceramics

Prototype imaging plates of $BaCl_2:Eu^{2+}$ dispensed in lithium-borate glasses were prepared at Victoria University of Wellington by Appleby. Neutron irradiation was done on these samples at the NEUTRA facility at the Paul Scherrer Institute, Switzerland. Several different lithium-borate imaging plate compositions were used as well as a BASND plate for comparison purposes [6, 7].

When compared to the BASND image, the glass-ceramic imaging plates were found to be limited by two main problems. The first was a decreased resolution, contrary to expectation, when compared to BASND, though the extent of this was different for different samples. This is thought to be in part a result of the increased thickness of the glass-ceramic imaging plates (500μm) when compared to the thickness of the

crystal layer of BASND (135μm). This leads to a larger scattering of the stimulating laser beam, causing a greater area than that of the focused laser beam being activated and undergoing PSL. The glass-ceramic imaging plates offering the highest resolution were those with the smallest $BaCl_2:Eu^{2+}$ crystal sizes within the glass matrix. This can be understood as being due to the smaller crystals causing less scattering of the laser beam within the glass. The trade-off in this case is reduced PSL efficiency due to the lower concentration of storage phosphor.

To improve the resolution of the glass-ceramic imaging plates, the size and concentration of the $BaCl_2:Eu^{2+}$ storage phosphors can be decreased, or the thickness of the imaging plate can be reduced. Both approaches lead to a reduced imaging efficiency, as less storage phosphors leads to smaller PSL signals and thinner plates lead to reduced neutron capture probability. Enriching the plates with the neutron sensitive isotopes of the glass material (^{6}Li and ^{10}B) can significantly improve the neutron capture fraction of the glass, partially counteracting the effect of a thinner plate.

The second problem encountered with lithium-borate neutron imaging plates is a clearly visible afterglow effect [6], as shown in figure 1-1.

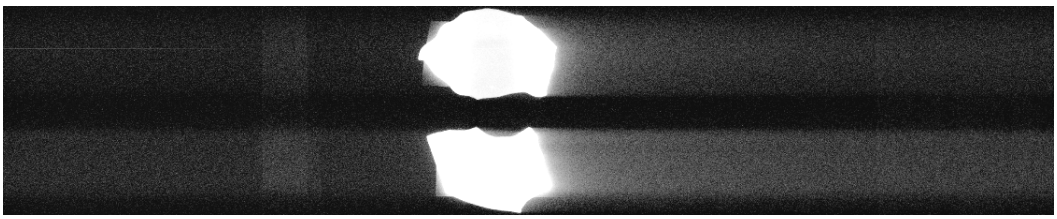

Figure 1-1: Afterglow problem with VUW produced LiBO glasses.

The afterglow effect is a severely limiting factor for the use of $BaCl_2:Eu^{2+}$ based imaging glasses. The effect is seen as a streaking of light (to the right of the image in figure 1-1) indicating that the image pixels are still glowing after the stimulating laser has moved past. This means the light from one pixel is being picked up when

other pixels are being measured. This effect is detrimental to obtaining high quality images.

A possible explanation of this behaviour which is investigated in this thesis is as follows: during stimulation, it is possible that thermally unstable traps are being populated as a phototransfer side effect of the process. When the stimulating light is removed, these newly populated traps will depopulate with a characteristic lifetime. If this lifetime is of the order of the scanning rate of the system, then an afterglow effect will be seen.

The motivation for this work is based on the two issues discussed:

- Improved Sensitivity: By improving the sensitivity of the $BaCl_2:Eu^{2+}$ phosphors, it should be possible to reduce the crystal sizes while still maintaining a useful level of image quality. The smaller crystal sizes should in turn lead to more transparent glasses that will reduce the scattering of the stimulation laser beam. This should give higher resolution images than is currently possible.

- PSL Afterglow: The afterglow problem is important as it poses a limiting factor in the image plate read-out process. Reducing the scan rate of the image read-out instrument so that the afterglow has subsided from one pixel before the next is read would remove the streaking effect on the images. This solution is unfavourable as high read-out speeds are considered an important feature of imaging plate technologies. Therefore, the ideal situation is to reduce the afterglow effect to acceptable levels.

1.4 Structural Characteristics of the Phosphor $BaCl_2$

The known phases of $BaCl_2$ are of orthorhombic, hexagonal and cubic symmetries, with the orthorhombic phase being the stable structure at room temperature. The

Ba^{2+} cation is smaller (ionic radius 1.49Å) than the Cl^- anion (1.67Å) [10] but the difference is not large. This enables the Ba^{2+} to have high co-ordination, with a co-ordination of 9 for the orthorhombic and hexagonal structures.

Anhydrous barium chloride is a hygroscopic material and will absorb environmental moisture with a half-time of roughly 30 minutes in normal laboratory conditions. This means special care must be taken when handling $BaCl_2$ to ensure the material is exposed to atmospheric conditions as little as possible. When dried in an oven at 200 °C it has been reported that both the orthorhombic and hexagonal forms of the material are produced [11]. The melting point of barium chloride is 965 °C, with an orthorhombic to cubic phase transition at 925 °C.

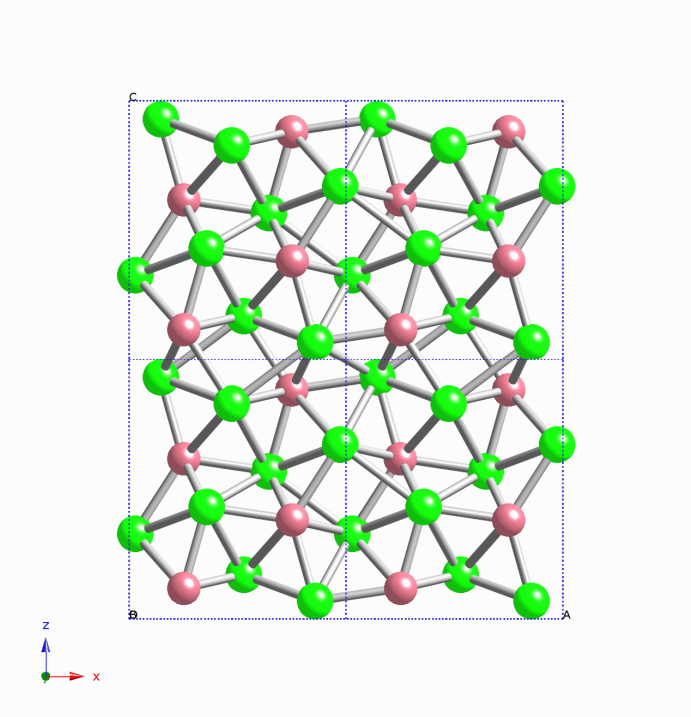

Figure 1-2: The orthorhombic phase of $BaCl_2$. The structure is plotted in the ac plane for four unit cells, only one cell deep in the b plane. Barium ions are brown, chlorine green.

This work is concerned primarily with the orthorhombic phase of $BaCl_2$ (figure 1-2), as previous work had found it to be the important phase for imaging plate

applications, and it is the only phase produced in the materials synthesis reported here. The orthorhombic phase has a space group symmetry of Pnma with unit cell constants a = 9.333 Å, b = 7.823 Å, and c = 4.705 Å [11], and the structure comprises planes containing Ba and Cl atoms lying perpendicular to the b axis, as shown in figure 1-2. The barium ion has a point group site symmetry of C_s, and an anion co-ordination of nine, with three Cl ions located on the same crystallographic mirror plane, and three each on the equivalent mirror planes located above and below. There are two distinct chlorine sites, both with C_s symmetry; one with four barium nearest neighbours and the other with five.

For storage phosphor applications, the possible defects in a crystal are important. For $BaCl_2:Eu^{2+}$ phosphors, electron trapping is believed to primarily occur at chlorine vacancies within the material [12]. The vacancies act as if there were a positive charge located at the site, with an electric potential which can be modelled as a hydrogen-like potential. When an electron is trapped at one of these vacancies, the resulting structure is referred to as an F centre (from the German word Farbe, meaning colour). Since there are two different chlorine sites within the material, it is expected that there should be two different F-centres. Previous studies have suggested that only one of these possible sites is actually PSL sensitive, and therefore only one site is active during image read-out [8]. The hole centre in europium doped barium chloride has not been unambiguously identified, but may be the europium ion itself.

Impurities incorporated into the lattice may change the nature of the traps within a material. A cation impurity may substitute in for a barium ion, causing a local distortion in the lattice. A chlorine vacancy next to (or close to) the impurity will result in a F_A-centre, which will experience a different potential to that of an F-centre. This will be most prominent in $BaCl_2$ when the impurity cation is an alkaline ion. The difference in charge between the barium (+2) and the alkaline (+1) ion will result in an effective negative potential next to the chlorine vacancy, and therefore will cause a significant change in the effective potential of the electron trap.

1.5 Preview of Thesis

This work is an investigation of $BaCl_2:Eu^{2+}$ as it applies to imaging plate applications, with specific reference to lithium-borate neutron imaging plates.

The main experimental techniques used for this are photostimulated luminescence (PSL) and thermally stimulated luminescence (TSL). All imaging plate technology incorporates the process of PSL in its operation, so the PSL experiments are directly relevant to the material's application as a storage phosphor. TSL is an experimental technique that can be used to obtain information about the nature of crystal defects within a material. In this way, TSL is ideal for examining the nature of the traps within the storage phosphor, which are responsible for the storing of imaging data.

As well as performing experiments, there are several discussions about the design and improvement of equipment. A TSL instrument at Victoria University underwent operational and design improvements to give more accurate and flexible operation. This included software modification, hardware modification and the subsequent testing and calibration of the incorporated changes.

A new TSL experiment was also designed using completely new components to perform low temperature measurements. This experiment is unusual for TSL in that a phototransfer mechanism must be included to make actual TSL measurement possible.

Chapter two discusses the underlying theory behind the TSL and PSL effects. Chapter three presents the experimental methods which have been used for sample preparation and characterisation, and the development of software and hardware for the TSL spectrometer systems. Chapters four and five present the experimental results of the thesis, describing the TSL experiments and the dependence of the PSL on co-doping respectively. Finally, chapter six gives a summary and some suggestions for further investigations. The appendices include a published paper on

the TSL spectrometer development, and a listing and description of the software which has been developed for the spectrometer.

Chapter 2

Theory

2.1 Photostimulated Luminescence

2.1.1 Photoluminescence

In photoluminescence (PL), light is absorbed by a material (or a photoactive centre in a material), which then emits light of a longer wavelength. Photoluminescence is discussed in many standard texts, for example [13].

The materials considered in this study are based on orthorhombic $BaCl_2$ doped with Eu^{2+} and possibly another dopant. It is the Eu^{2+} ion which is responsible for the luminescence. This type of luminescence centre is known as extrinsic due to the fact it is added to the original material, and localised because the luminescence occurs at a centre rather than as a direct result of dispersed electron-hole recombination.

Incident UV-light is able to excite the Eu^{2+} ion from the $4f^7$ ground electronic configuration into a $4f^6 5d^1$ configuration as shown in figure 2-1. This is an allowed transition as the f→d transition has $\Delta l = -1$ thus obeying Laporte's rule that optically induced electronic transitions must result in $\Delta l = \pm 1$ (here l is the orbital angular momentum quantum number). The time scale of the electronic transition is of the order of 10^{-16} s which is significantly faster than the nuclei vibration period, around 10^{-13} s.

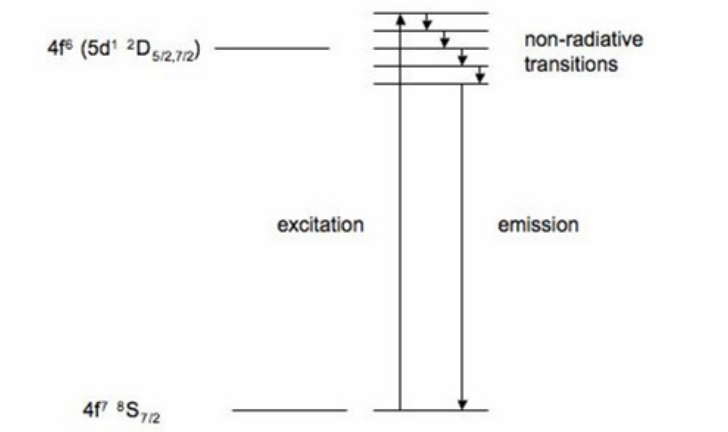

Figure 2-1: Energy level diagram of Eu^{2+}, showing the ground $4f^7\ ^8S_{7/2}$ state and the free ion excited $4f^6\ (5d^1\ ^2D_{5/2,7/2})$ state (left) with crystal field induced splitting (right).

The radiative lifetime of the excited state of the Eu^{2+} ion is of the order of 10^{-6}s. Since this is much longer than the lattice vibration period, the ion is able to decay to the lowest state of the excited multiplet long before the return to the $4f^7$ state. This is achieved through the creation of lattice phonons in a non-radiative decay process. This loss of energy is what causes the shift to longer wavelengths of the emitted light, and is known as the Stokes' shift. Since the 5d shell extends further from the Eu nucleus than other shells, electrons excited to this shell interact strongly with the crystal field. Therefore, the $5d^1$ 5-fold degenerate energy level is split into 5 separate energy state levels in a low symmetry crystal field. Because of this, and the simultaneous excitation of phonons, there tends to be quite a broad range of energies associated with the $4f^65d^1$ configuration resulting in a relatively broad emission spectrum. The emission occurs from the lowest of the crystal field split levels.

2.1.2 Photostimulated luminescence

When a material is exposed to ionising radiation, it can be left in an excited state where electrons and holes are trapped at various different types of defects in the crystal, with energies located within the band gap of the pure material. The trapped charges may be liberated using a light source, for example an LED or laser, and if

there exists a luminescent electron-hole recombination pathway, then the sample may show photostimulated luminescence (PSL), where the luminescent light is of higher energy (shorter wavelength) than the stimulating light (figure 2-2) [14].

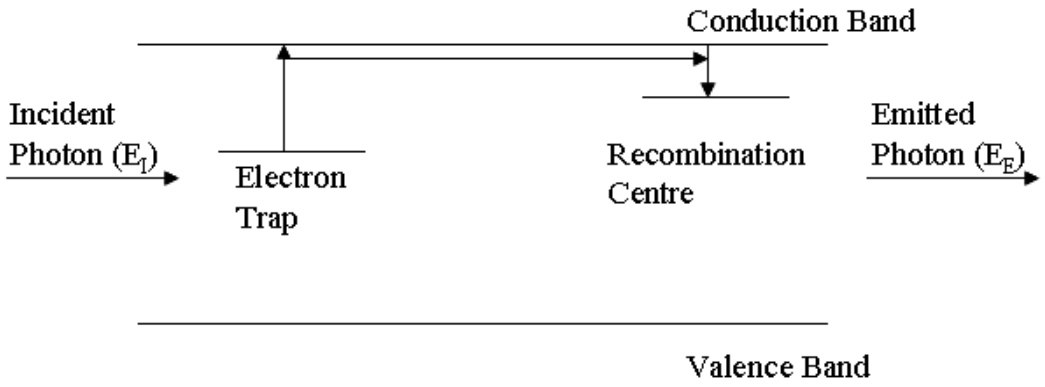

Figure 2-2: Simplified PSL energy level diagram. An incident photon excites an electron from a trap, and recombination with a hole occurs via a recombination centre, with the associated emission of a photon. The emitted photon is of higher energy than the incident photon ($E_E > E_I$).

In $BaCl_2$ it is believed that the electron trapping occurs at F-centres, for which there are two unique sites in orthorhombic $BaCl_2$. An F-centre is an anion vacancy in the lattice, and can either be intrinsic or induced during irradiation. The absence of the anion gives the vacancy an effective positive charge. The effect of this is to provide a hydrogen-like potential that an electron may become trapped at. The system has a similar energy level structure to hydrogen in this case, but the actual energies will be different and dependent on the surrounding ion distribution.

Electrons may be excited out of these traps by the incident excitation beam. The mechanism that results in PSL at this stage is under debate. Most research has been done [15-17] into the storage phosphor $BaFBr:Eu^{2+}$ rather than $BaCl_2:Eu^{2+}$ though the mechanism for PSL is likely to be similar to (at least) one of those discussed below

One possibility, proposed initially by Takashi et al. [15], is that holes are trapped at the Eu ion, resulting in a change from Eu^{2+} to Eu^{3+}. Under this scheme, electrons are excited out of the F-centre and into the conduction band. These now mobile electrons are able to recombine at the Eu ion with the trapped hole, resulting in an excited Eu^{2+} ion, $(Eu^{2+})^*$. This excited ion is then able to return to its ground state in the same way as discussed for PL, emitting a short wavelength photon. An important feature of this scheme is that the F-centres and Eu^{2+} ions do not need to be spatially correlated for PSL to occur.

The second option is more complicated and was proposed by Von Seggern et al. [16]. This interpretation allows for various different ways for the electrons and holes created during x-ray irradiation to be captured at their associated traps. Overall though, an important feature of the methods discussed is that the Eu ions and trapped electrons are spatially correlated.

In both mechanisms, during optical stimulation, the electrons are excited in the F-centres, undergoing a 1s→2p transition, where the 2p level is also located within the band gap. From here, the lattice relaxes due to the change in charge distribution, bringing the electron into an energy state close to the conduction band. The electron may then either return to the 1s level, be thermally excited to the conduction band and then recombine with the hole at the Eu ion, or tunnel to the adjacent Eu ion, resulting in recombination. For $BaFBr:Eu^{2+}$ Von Seggern et al. [16] found supporting evidence for tunnelling being the primary mode for recombination.

Since the luminescent ion is the same for both PL and PSL in $BaCl_2:Eu^{2+}$, it is expected that the luminescent spectra in both cases should be similar. This is confirmed in figure 2-3, recorded in this work, which compares the two luminescent spectra. The intensities have been normalised to give the same maximum intensity, as the PL process produces more intense luminescence than the PSL process. The emission spectra have maxima at approximately 410 nm.

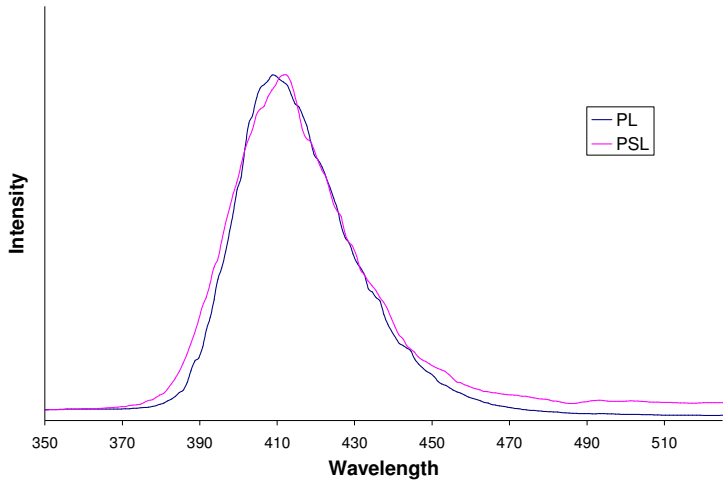

Figure 2-3: Comparison of the PL and PSL spectra of $BaCl_2:Eu^{2+}$.

2.2 Thermally Stimulated Luminescence

In thermally stimulated luminescence (TSL) trapped charges are released by thermal energy. For luminescence to occur there must be a recombination path back to the ground state that involves the emission of a photon (as opposed to phonon related processes). The temperature of the sample is increased at a linear rate, and the output light intensity measured as a function of temperature.

As the temperature is increased, more thermal energy becomes available for the de-trapping of charges (figure 2-4). Boltzmann statistics suggest that initially de-trapping is a rare event that becomes exponentially more probable as the temperature increases. This results in an increase in light output. This effect is negated by the fewer remaining trapped charges, so the light intensity reaches a maximum and then begins a steep decline. This resulting light intensity as a function of time is called a glow curve.

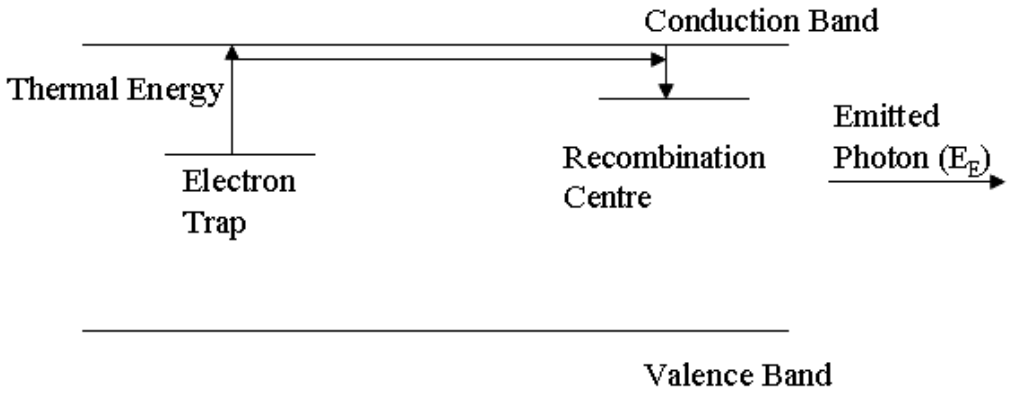

Figure 2-4: Simplified TSL energy level diagram. An increase in thermal energy increases the likelihood that a trapped electron will be excited out of its trap, and recombination with a hole occurs via a recombination centre, with the associated emission of a photon. The emitted photon is of higher energy than the incident photon ($E_E > E_I$).

Charges are trapped at lattice defects. There are a large variety of different defects that are possible in any crystal, both intrinsic and extrinsic. For example, if a site in a material that would normally contain an ion is vacant, this is called a Schottky defect. In this case, each vacancy will have a potential associated with it that is dictated by the ions around it. In this way, defects located at different lattice sites will have different trap energies.

Since there will almost always be more than one type of defect in a crystal (i.e. traps with different energies), it can be expected that there will be more than one glow curve peak observed in a TSL experiment. Depending on the material, there may also be more than one luminescence centre. This means that different peaks in the TSL curve may have different wavelengths associated with them. TSL is therefore detected using either photomultiplier tubes for maximum signal intensity without spectral information or via spectrometers for spectral resolution but with reduced sensitivity.

The nature of thermoluminescence means that the position and shape of the glow curves can give information about the nature of the trap, in particular the trapping energy and the frequency factor which may be simply thought of as how often a trapped charge will attempt to leave a trap.

Analysis of the de-trapping process involves some approximations. The first assumption usually is that the concentration of electrons in the conduction band during the heating stage is always much less than the number of trapped electrons. The second assumption is that the rate of electrons entering or leaving the conduction band is small compared to the rate at which traps are being emptied or refilled. These assumptions can be summarised as:

$$n_c << n \qquad \frac{dn_c}{dt} << \frac{dn}{dt} \tag{2-1}$$

where n is the concentration of trapped electrons and n_c is the concentration of electrons in the conduction band.

During heating, liberated electrons are able to return to the same trap ("retrapping") or recombine with trapped holes. If it is assumed that the retrapping process is much less likely than the recombination process, then the resulting glow curve is known as a "First-Order" curve. If on the other hand the retrapping rate is considered to be comparable with the rate of recombination, the resulting glow curve is known as "Second-Order". Theoretical models have been developed for situations between these two, and these are known as "General-Order" or "Mixed-Order" depending on how the models are developed.

In practice, the vast majority of glow curves are found to be of the "First-Order" variety [18, 19]. Using the approximations of equation 2-1 the following equation is

found from analysing the appropriate rate equations (assuming a linear temperature ramp with time) [20]:

$$I(T) = sn_0 \exp(-\frac{E}{kT}) \exp\left[-\frac{s}{\beta} \int_{T_0}^{T} \exp(-\frac{E}{kT'}) dT' \right] \tag{2-2}$$

Here I(T) is the intensity of the TSL as a function of temperature, s is the frequency factor, n_0 is the initial concentration of trapped electrons, E the energy of the electron trap, T the temperature, β is the temperature ramp rate, T_0 is the initial temperature and T' is a dummy variable used for the integration.

In the second order case, analysis leads to the following equation [21]:

$$I(T) = n_0^2 s' \exp(-\frac{E}{kT}) \left[1 + (\frac{n_0 s'}{\beta}) \int_{T_0}^{T} \exp(-\frac{E}{kT'}) dT' \right]^{-2}$$

$$s' = \frac{s}{N} \tag{2-3}$$

Here N is the concentration of available electron traps.

A method to determine whether a sample is first order or second order is required to allow the correct TSL analysis to be performed. Glow curve fitting is usually not conclusive enough by itself, but analysis of equations 2-2 and 2-3 provides useful insight. For 1st order curves, the term n_0, representing the initial concentration of trapped charges, only appears as a pre-exponential scaling term. This means that the initial concentration of trapped charges, and therefore the initial radiation dose, will have no effect on the position of the glow curve. For second order, not only does the n_0 term appear as a scaling term, it also appears inside the denominator term as part

of the exponent. This will mean that the maximum of the glow curve may appear at different temperatures for different n_0, i.e. different doses.

Therefore, the order of the particular glow curve may be identified by performing several experiments on a sample using the same temperature ramp rate but different initial doses. If the maximum of the glow curve occurs at the same temperature for each experiment, then the sample is first order, whereas if the peak maximum moves with temperature, then the sample is second order or not first order.

Figure 2-5 shows simulations of 1^{st} and 2^{nd} order glow curves respectively, using arbitrary but representative parameters. The simulations include various dose amounts, illustrating the varying position of the peak maximum for 2^{nd} order as opposed to the invariant peak position of 1^{st} order glow curves.

When analysing glow curves, there are a large variety of techniques available with their own advantages and disadvantages. Two methods were employed in this study, and they shall be examined here.

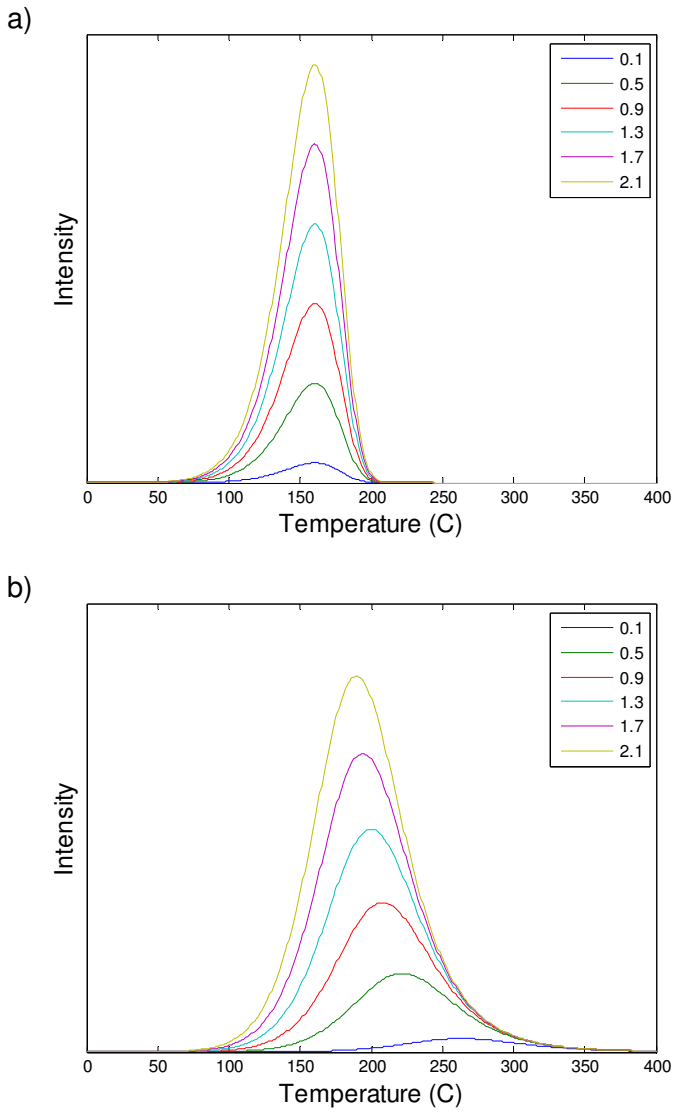

Figure 2-5: Simulations of 1st (a) and 2nd (b) order TSL glow curves. The parameters used are E = 0.8 eV, s = 10^8 s^{-1}, n_0=0.1, 0.5, 0.9, 1.3, 1.7, 2.1, β = 1 K/s.

2.2.1 Glow curve deconvolution

The first analysis method is known usually as (Computerised) Glow Curve Deconvolution (CGCD or GCD). The general principle is to fit an approximation to the theoretical glow curve functions to the data using several parameters.

The equations used for the deconvolution are described by Kitis et al. [22]. In both first and second order kinetics, the integral

$$F(T,E) = \int_{T_0}^{T} \exp(-\frac{E}{kT'})dT' \tag{2-4}$$

must be evaluated as is clear from equations 2-2 and 2-3. There is no analytical solution for equation 2-4 so Kitis et al. [22] developed the following approximation:

$$F(T,E) = \frac{kT^2}{E}\exp\left(-\frac{E}{kT}\right)\left(1-\frac{2kT}{E}\right) \tag{2-5}$$

For first order glow curves, this approximation is used to develop the following expression for the intensity as a function of temperature (where T_m is the temperature corresponding to the maximum intensity of the glow curve):

$$I(T) = I_m \exp\left[1+\frac{E}{kT}\frac{T-T_m}{T_m}-\left(\frac{T}{T_m}\right)^2 \exp\left(\frac{E}{kT}\frac{T-T_m}{T_m}\right)(1-\Delta)-\Delta_m\right] \tag{2-6}$$

Here the function Δ(T) is defined as

$$\Delta(T) = \frac{2kT}{E} \text{ and } \Delta_m = \frac{2kT_m}{E} \tag{2-7}$$

For second order glow curves, the following expression is obtained:

$$I(T) = 4I_m \exp\left(1 + \frac{E}{kT}\frac{T - T_m}{T_m}\right)\left[\left(\frac{T}{T_m}\right)^2 (1-\Delta)\exp\left(\frac{E}{kT}\frac{T - T_m}{T_m}\right) + 1 + \Delta_m\right]^{-2} \tag{2-8}$$

The free parameters for use when curve fitting are T_m, I_m and E, corresponding respectively to the temperature at the peak maximum, the intensity of the peak maximum and the corresponding energy of the trap associated with the glow peak.

I_m is dependent only on the number of traps populated by the external radiation source. E is dependent only on the particular defect. T_m depends both on experimental parameters (β) as well as the properties of the electron trap in the sample (E, s). Kitis et al. [22] give equation 2-9 as the relationship between T_m and other parameters for first order glow curves, and equation 2-10 as the relationship for second order glow curves.

$$\frac{\beta E}{kT_m^2} = s\exp\left(-\frac{E}{kT_m}\right) \tag{2-9}$$

$$\frac{\beta E}{kT_m^2} = s\exp\left(-\frac{E}{kT_m}\right)(1-\Delta_m) \tag{2-10}$$

In most, if not all, samples there exists more than one electron trap and sometimes more than one luminescent recombination option. Therefore, glow curves typically consist of multiple overlapping peaks. In this case, the GCD technique uses a linear combination of several functions of I(T) to account for the multiple number of peaks. If two peaks are very close, then GCD techniques will fail to provide unique solutions.

For this work, curve fitting was done using the MATLAB software from MathWorks. The particular MATLAB call used for curve fitting was the *lsqcurvefit* function, which performed multiple parameter least squares fitting on the supplied data, using a user specified fitting function.

2.2.2 Modified GCD analysis

Since several measurements at different temperature ramp rates and for different samples of the same composition were made, it was decided to attempt to fit glow curves using common parameters. This technique was only applied to the analysis of first order glow curves. As discussed in the previous section, the parameters used for fitting using the method of Kitis et al. [22] was to fit I_m, T_m and E. The maximum intensity, I_m, is a parameter which is dependent more on the experiment setup and sample preparation than any intrinsic property of the material, and so could not be common between different data sets. E is an intrinsic property (as the trap depth should be the same independent on ramp rate, amount of sample, sample surface area etc) of a material, and therefore only one energy parameter is used instead of one per TSL experiment.

However, the parameter T_m is made up of a combination of an intrinsic parameter (the frequency factor, s) and an extrinsic parameter (the ramp rate, β). Since for each sample the ramp rate was known (as this of course is set in the experimental setup) then the parameter T_m could essentially be treated as an intrinsic parameter. To do this, the curve fitting method had to be modified so the frequency factor, s, is used as a parameter instead of T_m. T_m could then be calculated for every iteration of the curve fitting from s, using the relationship shown in equation 2-9.

There were two major issues with implementing this approach to curve fitting. The first was that the frequency factor takes a wide range of values, from unity to $> 10^{14}$ s^{-1}. The curve fitting algorithm was found to be unable to deal with this range

properly so instead of using the frequency factor directly, the logarithm $p = \log_{10} s$ was used instead.

The second problem was caused by the fact that equation 2-9 for obtaining T_m from the parameters E, s and β cannot be solved analytically for T_m. For each step of the curve fitting process, T_m must be calculated numerically for the current values of E and s (which change each step, whereas β is constant throughout the curve fitting process).

2.3 General Rate Equations

Some experiments reported here involved a room temperature irradiation of a sample before cooling the sample to 25K, and then irradiating with a red laser before applying a linear temperature ramp. After the room temperature irradiation, low temperature traps were thermally bleached. In order to populate these traps once more, a phototransfer technique was employed at low temperatures; this is the reason for the red laser irradiation. This phototransfer process is a more complex one than simple TSL and so requires a more comprehensive analysis than that presented earlier. This experiment is referred throughout this work as the LT-TSL experiment (low temperature TSL).

The general rate equations for a system with shallow and deep traps are described below [23]. A shallow trap can loosely be thought of as a trap that may be thermally emptied within the time scale of the experiment, whereas a deep trap can be considered to be thermally stable with a 'de-trapping' time constant much longer than the observation time.

$$\frac{dn_c}{dt} = g + \sum_{i=1}^{N_e}\left(n_c f_i + n_i s_i \exp\left(-\frac{E_i}{kT} \right) - n_c (N_i - n_i) A_i \right) - n_c \sum_{j=1}^{N_h} m_j A_{mj}$$

$$\frac{dn_i}{dt} = -n_i f_i - n_i s_i \exp\left(-\frac{E_i}{kT} \right) + n_c (N_i - n_i) A_i$$

$$\frac{dm_j}{dt} = n_v (M_j - m_j) B_j - n_c m_j A_{mj}$$

$$\frac{dn_v}{dt} = g - n_v \sum_{j=1}^{N_h} (M_j - m_j) B_j$$

(2-11)

The terms in the above equation have the following meanings:

g is the rate of electron-hole pairs being produced by the ionising radiation
n_c is the concentration of electrons in the conduction band
n_i is the concentration of electrons in the ith trap
N_i is the concentration of available electron traps of type i
f_i is the rate of electrons being excited by the ith trap
s_i is the frequency factor for the ith trap
E_i is the energy of the ith trap
A_i is the probability of an electron being trapped in the ith trap (from the conduction band)
n_v is the concentration of holes in the valence band
m_j is the concentration of holes in the jth trap
M_j is the concentration of available hole traps of type j
B_j is the probability of a hole being trapped at the jth trap (from the valence band)
A_{mj} is the probability of an electron-hole recombination occurring at the jth hole trap
N_e is the number of unique electron traps
N_h is the number of unique hole traps

This model assumes that the hole traps are deep and so thermally stable. If it is assumed that luminescence occurs during recombination at a hole trap, and that only

some of the hole traps are radiative (some may disperse the energy via other means, for example thermally), then the luminescence is proportional to:

$$I = -\sum_{j_o} \frac{dm_j}{dt} \tag{2-12}$$

where j_o are traps where radiative recombination may occur.

Simplifications can be made to the rate equations for the system being examined here. These are based on assumptions that have been made after observing normal TSL and PSL behaviour.

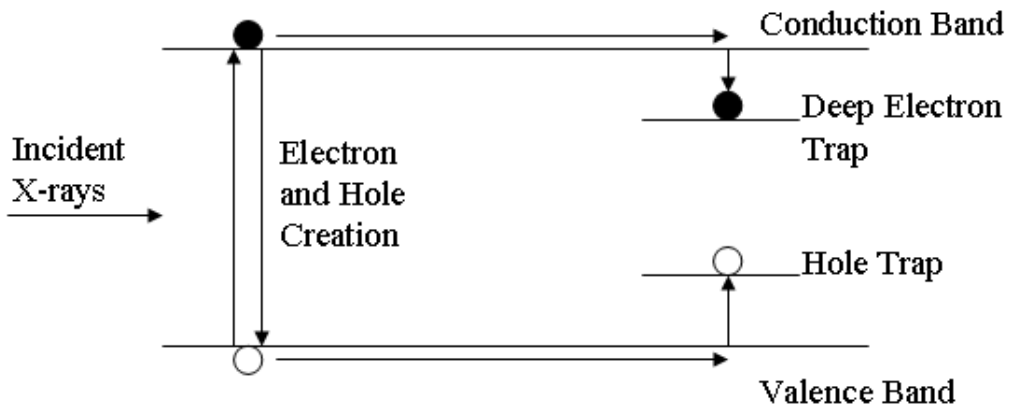

Figure 2-6: Simulated irradiation system. Incident ionising radiation creates electron-hole pairs, which are able to be trapped at lattice defects.

During x-ray irradiation (which is done at room temperature) it can be assumed that there is one deep trap in operation, trap i=1 (there are actually more, but this has little effect on the observations), and that the shallow traps that are important for later parts of the experiment are empty. Also, for convenience it will always be assumed there is just one hole trap, trap j=1. The equations thus become (figure 2-6):

$$\frac{dn_c}{dt} = g - n_c(N_1 - n_1)A_1 - n_c m_1 A_{m1}$$

$$\frac{dn_1}{dt} = n_c(N_1 - n_1)A_1$$

$$\frac{dm_1}{dt} = n_v(M_1 - m_1)B_1 - n_c m_1 A_{m1}$$

$$\frac{dn_v}{dt} = g - n_v(M_1 - m_1)B_1 \tag{2-13}$$

The initial conditions and probability values for the system will be discussed in the experimental section but it can be assumed that all concentrations are zero prior to irradiation.

After irradiation, the system is in a room temperature stable state. The sample is then cooled from room temperature (~295 K) to 25 K in a cryostat. This removal of heat energy has no effect on the trapped charges, since it is assumed that only stable traps are filled.

$$\frac{dn_c}{dt} = \sum_{i=1}^{N_e}(n_c f_i - n_c(N_i - n_i)A_i) - n_c m_j A_{mj}$$

$$\frac{dn_i}{dt} = -n_i f_i + n_c(N_i - n_i)A_i$$

$$\frac{dm_1}{dt} = n_v(M_1 - m_1)B_1 - n_c m_1 A_{m1}$$

$$\frac{dn_v}{dt} = n_v(M_1 - m_1)B_1 \tag{2-14}$$

Once the sample is at 25 K, a red laser is used to excite electrons out of trap 1. These are then transferred through the conduction band to either another deep trap, a

shallow trap which is now thermally stable, or (most probably) a recombination centre – modelled as a hole trap. This system can be modelled using (figure 2-7):

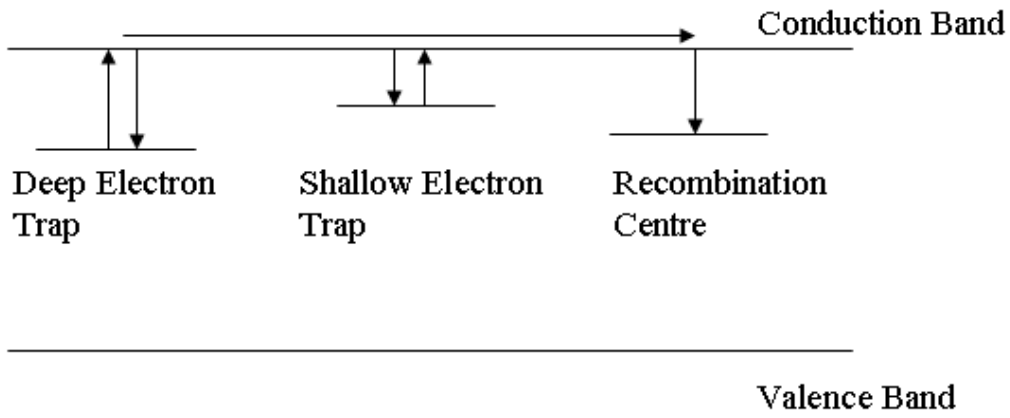

Figure 2-7: Low temperature photo-transfer diagram. Electrons in deep traps can be transferred to shallow traps, though some will end back in the deep traps or will undergo recombination, removing them from the system.

The initial conditions for this stage are simply taken as the final values for the previous step, with $n_{i\neq1} = 0$. Once again the thermal terms are ignored. This is based on the assumption that any traps still thermally unstable at 25 K will have depopulated before the laser is used.

The final stage is a normal TSL experiment, where the temperature is ramped at a linear rate. For normal TSL experiments, numerical integration of the rate equations is unnecessary, as the glow curve equations 2-2 and 2-3 suffice. The rate equations are used to incorporate the phototransfer stage of the low temperature TSL experiment into the model.

2.3.1 Simulation of LT-TSL using rate equations

Basic simulation of the LT-TSL experiment was performed using simplified versions of the rate equations described in the previous section. The system is described as consisting of a two electron traps and one hole trap, where the hole trap acts as the luminescent recombination centre.

The electron traps are set up so that one represents the deep, room temperature stable trap while the other represents the shallow, room temperature unstable trap. The parameters used are based on those used by McKeever et al. [23], even though the materials of interest were different. The deep trap is treated as if it is always completely thermally stable.

The shallow trap assumed to have negligible population during high temperature stages, which is equivalent to stating the following

$$n_s = 0, \frac{dn_s}{dt} = 0 \tag{2-18}$$

For the low temperature stages, it is treated in the same way as the deep trap, as if it were completely thermally stable. These approximations remove the need to include the thermal terms in the simulation.

The system is labelled as D is the deep trap, S is the shallow trap and H is the hole trap. The parameters used are:

$N_D = N_S = 10^{17}\ m^{-3}$
$M_H = 2 \times 10^{17}\ m^{-3}$
$A_D = A_S = B_H = 10^{-16}\ m^3 s^{-1}$
$Am_H = 10^{-16}\ m^3 s^{-1}$

$f_D = f_S = 10^{-2}\ s^{-1}$
$g = 10^{16}\ m^{-3}s^{-1}$

The first stage of the simulation is run for 1000 s, with 0.1 s steps, to simulate the x-ray irradiation stage of the LT-TSL. During this process, no stimulating light is used so both f_D and f_S are set to 0.

The second stage of the simulation is also run for 1000 s, and is used to represent the period of time between x-ray irradiation and the red laser irradiation. The parameters g, f_D and f_S are set to zero.

The final stage is the most relevant for the LT-TSL experiment. Here, the sample is irradiated with a red laser after being cooled to 25 K to populate the shallow trap. The parameter g is set to zero as there is no x-ray irradiation, and therefore no electron-hole production, and the shallow trap is now included into the simulation. Figure 2-8 shows the concentration of trapped charges in the three different trap types (shallow electron, deep electron and hole). As expected, the hole trap population is equal to the sum of the two other traps, and the shallow trap initially begins filling before proceeding to empty along with the other two traps.

Several approximations are made in this model in an effort to simplify the calculations. The most notable approximations are that both electron traps have the same probability of interacting with the stimulating light source, as well as the temperature approximations which could have an effect on the different emptying rates.

The simulations show that there is an initial rise in the concentration of electrons in shallow traps before levelling off and the concentration begins to decrease. This is expected, as during the stimulating stage, there is the competing process of recombination occurring which removes electrons from the system, therefore the long term trap concentrations should tend to zero.

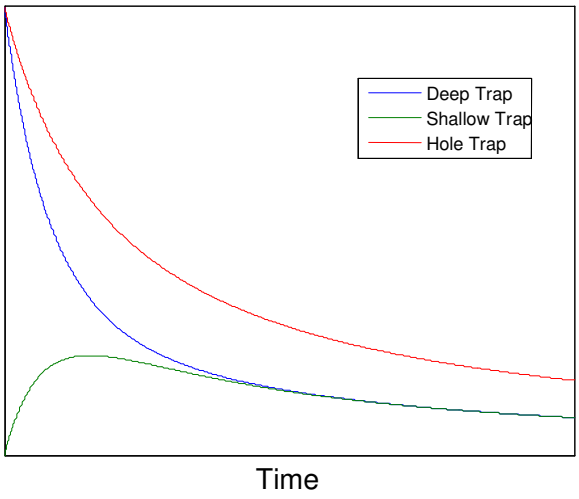

Figure 2-8: The concentrations of the three different traps (shallow electron, deep electron and hole) during the red laser stimulation stage of the LT-TSL experiment. Initially, the shallow electron trap is empty, while the deep electron and hole traps have the same concentrations.

Chapter 3

Experimental

3.1 Sample Preparation

$BaCl_2$ is a hygroscopic material requiring all sample preparation to be done under dry conditions to avoid the formation of the hydrate, $BaCl_2.2H_2O$.

Two glove boxes were available for sample preparation, a custom VUW designed box and a commercial box acquired during the project. The VUW designed and built box used a continuous flow of nitrogen gas through it, and an evacuable transfer port for material insertion/removal. The relative humidity was typically less than 1%.

Attached to this glove box were two furnaces (figure 3-1), a horizontal resistance based tube furnace using a Kanthal element, giving a maximum operating temperature of approximately 1100 °C, and a RF furnace capable of at least 1400 °C. Both contained a quartz tube that was used to house the sample and allow for a controlled atmosphere during heating. The atmosphere used was 99.99% pure (instrument grade) argon. The samples were contained inside glassy carbon crucibles with glassy carbon lids from the HTW Company, Germany.

The heating regime was to heat the (dry) samples at 1000 °C, well above the melting point of $BaCl_2$ (963 °C), for 2 hrs and then cool to 890 °C and hold there for at least 1 hr to ensure the phase of the material was orthorhombic ($BaCl_2$ shows a phase transition to the cubic phase above 925 °C). The samples used for the high temperature TSL measurements (discussed below) were prepared in the resistance furnace. Later, when PSL and low temperature TSL measurements were to be made,

new samples were prepared in the RF furnace to avoid possible contamination from residual spilt chemicals in the resistance furnace.

Figure 3-1: The two furnaces used for the preparation of $BaCl_2$ samples. The top furnace is the RF furnace, the bottom furnace is the horizontal resistance based furnace.

The second glove box, made by High Vacuum Technologies, Melbourne, was much larger than the VUW box and was tall enough to house a 6 digit balance contained within a draft shield to minimise errors due to atmospheric gas turbulence. The atmosphere of this box was argon, which could be dried using a system based on a molecular sieve and copper absorber. The relative humidity was typically less than 0.1%. The samples prepared during the later stages of the project were prepared in this box to take advantage of the more accurate balance, and the more comfortable work space. After preparation, the samples were sealed and removed from this glove box to the VUW box since the two furnaces were still attached only to the VUW glove box. The short distance between the two units meant that the samples were not at risk of any significant hydration during transfer.

3.2 TSL Rig

The requirements for a TSL measurement are an ionising radiation source, and the ability to take intensity measurements whilst applying a controlled temperature ramp to the sample. The equipment used for TSL measurements described in this section is a unique design developed at VUW, and has been recently been reported in the literature ([24] and also appendix A). During this work, substantial modifications were made to the equipment to allow for greater flexibility and reliability of measurement. This work involved software design, testing and hardware modification of the system.

3.2.1 Irradiating the sample

An x-ray beam was used to irradiate the samples. The x-rays were generated from a Philips PW1720 X-ray generator using a tungsten tube running at 50 kV and 20 mA, with a 1.6 mm thick aluminium filter. Since samples were small, dose calculations are difficult. Assuming a normal cross-section area of 5 mm^2, the dose the samples received with the aluminium filter was approximately 1100 mSv/min. Different irradiation times were used depending on the measurement taking place and the equipment performing the measurement.

The sample was placed on a holder (figure 3-2) that was also used for TSL measurements and is described in more detail in the next section. The advantage of this system is the sample did not need to be moved between irradiation and measurement. The samples were used in powdered form, and only a few hundred micrograms were used (the exact amount was not a precisely controlled quantity).

3.2.2 TSL measurement – rig design

A VUW custom designed TSL rig was used to make measurements between -50 °C and 450 °C, the components of which are a sample holder that acts as the heat source (figure 3-2), a thermal control unit, a light detector that was either a photomultiplier or CCD spectrometer, and a computer for experimental control and data storage. The schematic for this equipment is shown in figure 3-3.

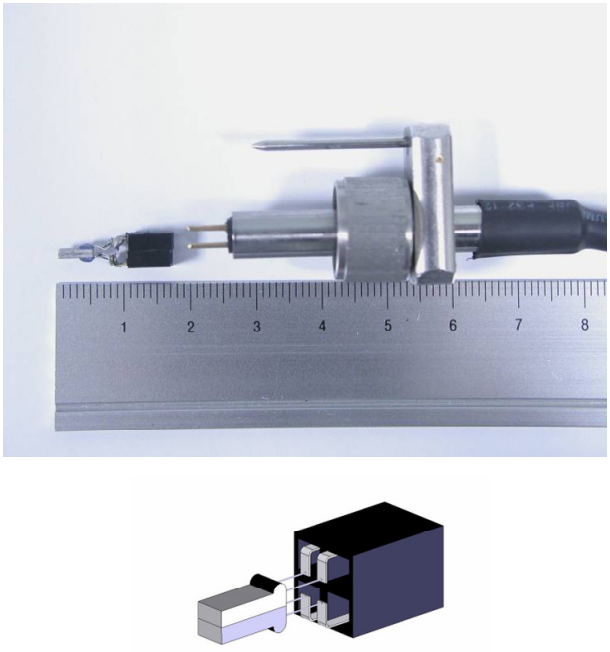

Figure 3-2: TSL holder and temperature control component. Top: Photo of actual device, showing the separate holder and hot finger. Bottom: 3d drawing of the hot finger component. The sample is placed on the top face of the top PT-100 resistor.

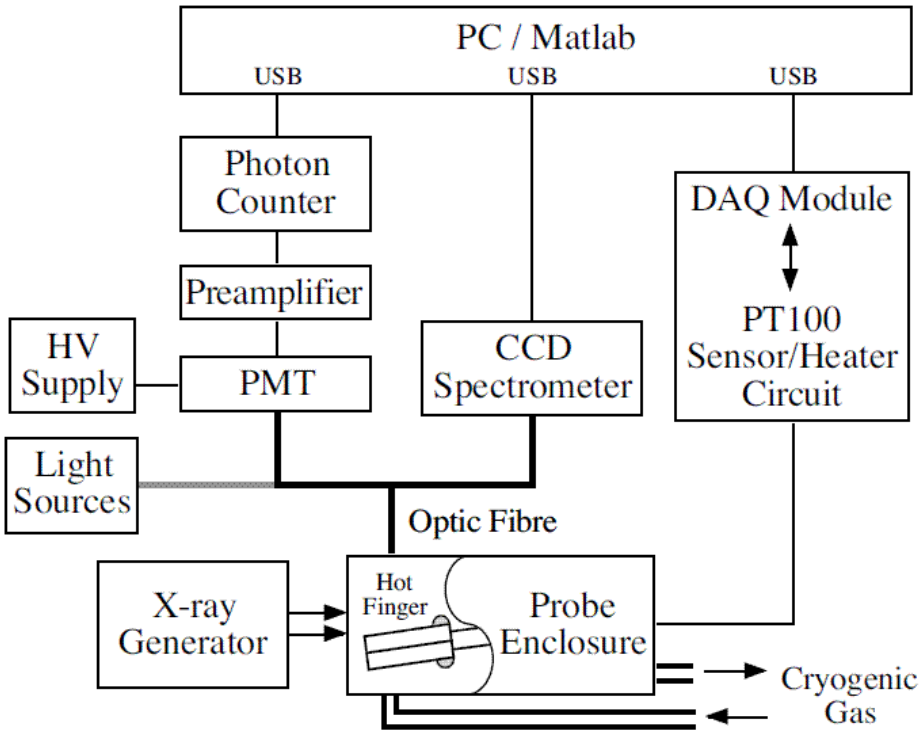

Figure 3-3: Schematic diagram of the VUW TSL rig.

The sample holder (finger) consists of two flat film PT-100 (100 Ω) resistors evaporated onto ceramic substrates (Labfacility Ltd. product code DM503); the substrates are joined together along their bases. The join is made using an organic binder (Ultra High Temperature Hot Paint made by Plasti-Kote) that is capable of working over the required temperature range (i.e. up to 500 °C). The finger is oriented such that one of the resistors provides a surface to hold the sample. This resistor is used as a temperature sensing element; the other resistor is used as a heating element. The plane of the PT-100 units is held at a slight angle to the incident x-ray beam, and during TSL the emitted light is collected by an optical tube mounted just above the top surface and a small (3-5 mm) distance away from it.

The advantage of using this configuration is that the sensing element is directly in contact with the sample, allowing for minimal difference between sensor temperature and sample temperature.

The resistors are coupled to a plastic connector via their leads. The plastic connector is made from gluing together two modified PCB jumpers – the modification being that the wire connecting the two sides of the jumper is cut, isolating the two sides. The leads are soldered onto one end of the jumper.

The connector is designed to plug into a custom made mount which uses PCB pins to hold the connector. The bottom two pins are connected to one wire each that runs down the shaft of the mount, whilst the top two pins connect to two wires each. The reason for connecting these to two wires each is for a 4-terminal resistance measurement of the sensor component of the finger.

The finger is connected electronically via a cable to a custom-built temperature control/measurement box. This in turn is connected via USB to a PC running custom software in the MATLAB environment. The temperature control is a combination of digital and analogue electronics. The digital interface is through a National Instruments USB-6900 DAQ (Data AcQuisition) and the analogue circuitry is an in-house design.

The control circuitry measures the resistance of the sensing PT-100 resistor in a 4-terminal fashion. A constant current is applied across the resistor from one pair of wires and the voltage difference is measured by another pair. The constant current source is maintained at 5.5mA through circuitry located in the temperature control/measurement box. This gives a maximum self-heating power of the PT100 resistor of 8 mW (corresponding to a self heating of approximately 0.16 °C). The voltage drop across the resistor is fed into a differential amplifier and the output scaled to a pre-set range corresponding to the -50 °C to 450 °C temperature range of the device.

The desired temperature is set by having the DAQ output a voltage between 0 and 10 V which is scaled to the same range as the sensor voltage. These are then compared and if the required temperature is greater than the current temperature then

current is applied to the heating element of the PT100 finger. The heating circuitry uses both proportional and integral control.

The sensor voltage is also acquired digitally by the DAQ and stored by a PC. The DAQ has two 14-bit ADCs, though only one is used for the TSL.

For a TSL measurement, the temperature must be ramped in a linear fashion. To achieve this, a PC running MATLAB is used to provide periodic increments in the temperature set-point of the heating circuitry. The temperature is typically updated every 0.1 s giving a nearly smooth ramp over the entire heating range, up to heating rates of 5 K/s. For below ambient temperature starting conditions, cooled dry-N_2 gas is passed over the sample. A copper coil is submerged in pre-cooled isopropanol and the N_2 gas is passed through the coil, reducing the gas temperature.

This gives a TSL range with cooling of -50 °C – +150 °C though this may be extended at the upper end by turning off the gas flow after the unit reaches room temperature. The disadvantage of this technique is there tends to be a slight non-linearity in the sample temperature when the gas is switched off. Another technique for heating rates > ~0.5 °C/s is to turn the gas flow off before beginning the temperature ramp. As long as the natural warming rate of the unit is less than the ramp rate, this procedure gives good linear results.

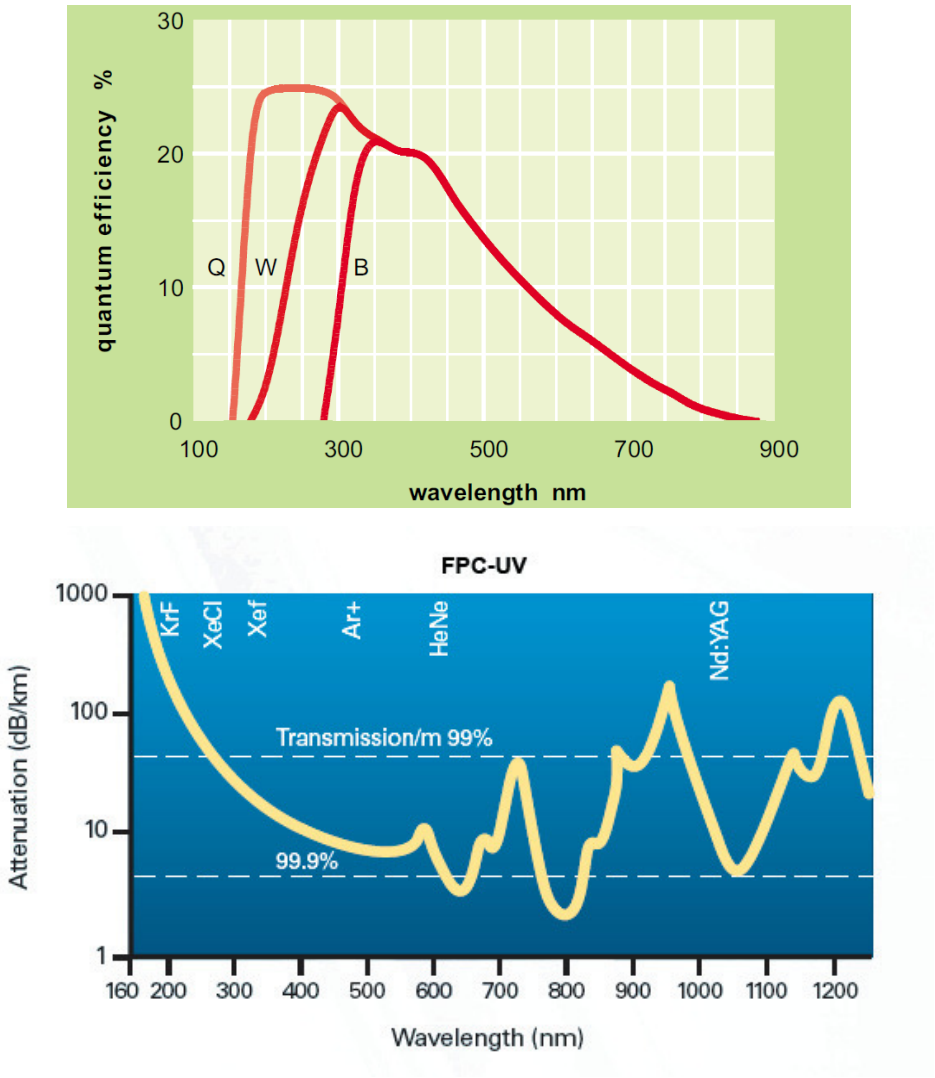

Figure 3-4: Top: Spectral responsivity of the Electron Tubes Ltd 9558QB PMT, the line marked Q is for this model. Bottom: Attenuation of the fibre optic cable as a function of wavelength. These specifications are from their respective datasheets.

During the heating process, measurements are made on the light output of the sample, and this was done either using a photomultiplier tube (PMT) or a CCD spectrometer. The photomultiplier available was a Peltier-cooled Electron Tubes Limited 52 mm 9558QB PMT (whose spectral resposivity is shown in figure 3-4) with a Stanford SR445A preamplifier and a Stanford SR400 two-channel gated photon counter. For normal operation for this work, where $BaCl_2:Eu^{2+}$ and variants

were being measured, a BG-12 filter was placed in front of the PMT window as this reduces most background light while still allowing the Eu^{2+} luminescence to enter the PMT. The CCD spectrometer available was an Ocean Optics USB2000 with a 600 lines/mm grating (figure 3-5) and 200 µm slit, which provides a measurement range of 340-1025 nm with a resolution (FWHM) of 8 nm. The instruments were coupled to the sample using a fibre optic cable (typically a B&W Tek FPC Series Fibre Patch Cord of length 1.5 m, diameter 1 mm, numerical aperture 0.22 with a pure silica core – see figure 3-4 for spectral attenuation data) with one instrument used at a time, though it is possible to perform simultaneous measurements using a bifurcated fibre optic cable. The fibre was positioned directly above the sample with a gap of 3 – 5 mm.

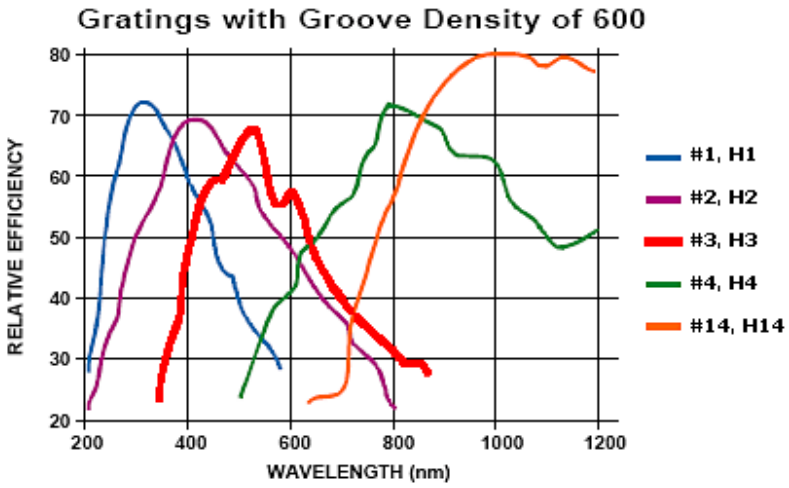

Figure 3-5: Efficiencies of the CCD spectrometer diffraction gratings. The grating used for this work was the #3 grating blazed at ~500nm.

The MATLAB software was also used to control and log the intensity data from the optical detectors. This was done simultaneously with the heating control, with all three components run asynchronously. Typical integration times were 0.5 - 0.7 s for the PMT and 0.1 - 1.5 s for the CCD spectrometer.

3.2.3 TSL measurement – process

After irradiation, the sample is left on the PT100 finger. Storage phosphors may glow for some time after irradiation. This can be monitored by taking optical measurements after irradiation. Once the afterglow has reduced to an acceptable level (usually less than 500 photon counts over 0.5s), the TSL experiment is started. The experimental parameters are entered into the PC software and then the linear ramp and optical acquisition begins. Experimental parameters are the temperature ramp rate, starting and finishing temperatures as well as the integration time for the photon counter or CCD spectrometer.

The MATLAB software was redeveloped over the course of this work to produce more linear temperature ramps and greater customisation of the experiments. Originally the software followed a fairly basic, script based operation. This involved incrementing the desired temperature to the next value in the ramp, and then instructing the detector (PMT and/or CCD) to begin integration. The PC would then wait until the integration times were over, instruct the instruments to send the acquired data and wait until this process had completed. The data was then stored in an array and the software incremented to the next temperature value and begun the process again.

The problem with this was that typically 700 ms integration times (PMT) or > 1 s (CCD) were used for measurement. Adding the serial data transfer time meant that the shortest period for updating the required temperature was about 1s. This lead to non linear ramps as the time it took for the sample to be heated to the next temperature step was typically much shorter than 1 s, resulting in a crude, step-like approximation to a linear temperature ramp.

Over several months, the software was substantially changed to allow for easier operation. The PMT and CCD were setup to run asynchronously in MATLAB. This allowed MATLAB to continue to execute instructions whilst the instruments were taking measurements. After the integration was over, the instruments then signalled

they were finished and passed the data into buffers in MATLAB. It is only after the buffers were full that MATLAB had to return to the instruments, acquire the buffered data into arrays and send out instructions to begin the next measurement.

The advantage of this process is for the rest of the time, MATLAB is free to run other instructions. The main process implemented during this time was the updating of the linear temperature ramp and the recording of the temperature data. The temperature was now able to be updated much more frequently – usually every 0.1 s, a factor of 10 increase in update frequency. The temperature was also sampled at this rate, allowing for a much higher resolution of the actual sample temperature during the run. A second, less important process that was implemented was the real time graphing of the PMT data as a function of temperature. If there are problems during the experiment, they can in this way be identified immediately, instead of after the experiment is complete. CCD data cannot be displayed in real time. The MATLAB software is included in this thesis in the envelope CD (appendix A).

During TSL measurement, the laboratory lights are turned off, as the equipment is sensitive to background light. Once the experiment has finished, the acquired data is processed and displayed on screen. The data at this stage may be saved to a file for later analysis.

Previous studies on LiF:Mg,Ti (TLD-100) found that the acquired glow curves may change depending on the thermal history of the sample [25]. The samples of TLD-100 were annealed before irradiation, and the intensity of some of the peaks was found to increase as the heating and cooling rate during the anneal stage was increased. This suggests that samples should be subject to the same initial bleaching and thermal conditions between each experiment.

One problem with the TSL instrument design relates to the PT-100 probe used as a sensor and holder for the sample. The probe, as well as the sample, is subjected to the x-ray beam during irradiation. There is a clear, insulating layer on top of the

platinum element which shows TSL. The TSL is much less intense than the typical result due to $BaCl_2:Eu^{2+}$ crystals, but is still a concern in general, especially as the TSL rig is designed to be used for TSL measurements of any sample.

The TSL signal from the PT-100 is centred just below 700 nm, and during TSL shows itself as a single peak centred between 100 °C and 200 °C. Fortunately this is a quite different wavelength than the luminescence wavelength of the $BaCl_2:Eu^{2+}$ luminescence, which exhibits a spectral maximum at approximately 400 nm. Also, the signal is relatively weak, and will only cause problems for materials with weak TSL. Measurements made with the PMT are done with a BG-12 optical filter which cuts out the TSL due to the PT-100 probe completely. When such a filter is inappropriate for the sample being measured, the PT-100 probe can be spray painted black using high temperature black paint. This gives good results but the paint typically does not survive sample removal and has to be replaced between uses. This delay can be minimised by preparing multiple holders at a time.

3.2.4 TSL analysis

Analysis is performed on the data using data analysis software developed using the MATLAB language.

3.3 PSL Measurements

Storage phosphors work on the principle of Photostimulated Luminescence (PSL), which is described in detail in chapter 2. To make PSL measurements, a sample must be prepared, irradiated and then the luminescence caused by the stimulation of the sample by light must be measured. Irradiation was done using the same x-ray equipment as for the TSL experiments.

The apparatus designed and made at VUW by Florian Kienle was used for PSL measurements. It consists of a red solid state laser for photostimulation and a PMT for measuring the PSL intensity. The laser is mounted at a 90° angle to the PMT, and

a BG-12 glass filter is used to both reflect the laser by 45° to direct it onto the sample, and to separate the blue luminescence from the reflected red light. This setup is shown in figure 3-6.

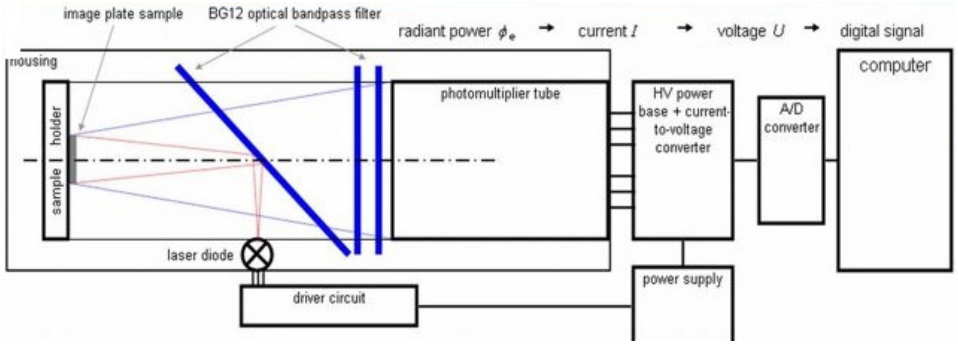

Figure 3-6: Schematic diagram of the VUW portable PSL unit.

The PMT used is an Electron Tubes 9111WB (non-cooled) model, which is sensitive from visible wavelengths down into the UV. The laser diode can be operated in constant stimulation (laser always on) mode or pulsed at frequencies up to 100 kHz, with two different optical stimulation intensities available.

A sample may be mounted either directly onto a holder, inside a glass capillary or inside an air-tight holder. The output of the PMT is scaled to give a -10 – 0 V range, with the measured intensity being proportional to -voltage. The output is sampled by a PC through either an ADC-100 or ADC-16 from Pico Technology Ltd using the PicoLog program from the same company.

PSL typically shows an exponential like decay with time, though most, if not all, real materials have PSL that cannot be fitted using a single exponential decay function. For storage phosphors, the important qualities of the material can be inferred from the decay time of the signal and the number of photons produced, which is proportional to the area under the decay curve (minus the background reading). Constant stimulation mode was used for storage phosphor measurements.

3.3.1 Sample preparation for PSL measurements

One of the goals for this project was to compare the storage efficiency of $BaCl_2:Eu^{2+}$ crystals doped with various impurities. In order to standardise the PSL measurements to allow comparisons, samples were prepared according to the same procedure.

A PSL measurement is dependent on several factors to give the overall measured intensity. The phototube efficiency, sample distance and stimulation intensity were constant for all experiments since the PSL instrument was not changed between experiments.

The luminescent output of the phosphors is related to the total surface area of phosphor that is exposed to the excitation beam. In order to standardise this surface area, the samples were fabricated as pellets with a diameter of 11 mm. The X-ray beam was collimated to produce an irradiation spot of diameter 7 mm, intentionally smaller than the diameter of the pellets. This is because the edges of the pellets tended to be less mechanically strong and were prone to crumbling, so by not irradiating these regions this effect on the luminescence intensity was avoided.

The samples were housed in an air-tight measurement holder to minimise changes in storage efficiency brought on by the absorption of atmospheric moisture into the crystal structure.

For a single sample several repeat measurements were made. Before irradiating the sample, the sample was bleached to remove any residual PSL from the material. Bleaching was simply done by placing the sample under a tungsten bulb with a red filter blocking out short wavelengths. The reason for the red filter is to avoid any possibility of defect creation due to short wavelength light. The bleaching time was 30 minutes.

After bleaching, the sample was taken to the x-ray unit, covered in a black cloth to avoid any possible excitation effects from UV light. The sample was then irradiated for 30 seconds using 50 keV, 20 mA x-rays, the dose the samples received was approximately 1100 mSv. The sample was then moved to the PSL measurement unit, again under black cloth. This was especially important as any tungsten or fluorescent lighting would begin bleaching the sample, reducing the measured intensity of the PSL effect.

The PSL measurements were recorded using the PICO ADC-16 data acquisition device. Samples were taken once a second at 16-bit resolution for 30 minutes. Of the two intensity options available for the red excitation laser on the unit, the lower 1mW setting was used. This is because the higher, 10 mW power setting tended to give a strong PSL signal at the start of the measurements, causing the ADC to clip the signal at 2 V.

Since the output of the PMT unit was scaled to 0 to -10 V, the output had to be put through a 1:5 voltage divider to reduce the output to within the limits of the ADC, which was -2 V to +2 V. Since the output of the PMT was unipolar, half of the ADC range was wasted, reducing the effective resolution to 15-bit.

3.4 Custom TSL Rig – Ultra Low Temperature

It was found by analysis of the TSL data that the trap energies and frequency factors of the peaks within the TSL rig's temperature range were giving much longer time constants than expected from the afterglow effects observed during image plate read-out as described in chapter 1. It was therefore necessary to explore the lower energy traps, which would only be apparent at much lower temperatures.

A cryogenic unit with a variable and controllable temperature range was available but in a different room to the x-ray set. This meant that low temperature irradiations were not possible. Therefore, a new method for populating the low energy traps was

developed, the theory for which is presented in chapter 2. The new design consisted of a cryogenic unit (RMC-22 continuous flow cryostat) capable of generating linear temperature ramps from as low as 10 K up to ~380 K, the unit combining a PMT and red laser source used for PSL studies and a data acquisition unit.

The cryogenic unit was found to only be able to produce reliable linear temperature ramps up to a little more than 10 K/min for a temperature range of 25 - 300 K. This meant much slower temperature ramps were to be used when compared to that possible with the standard TSL rig.

The sample was mounted on a small strip of copper using GE Varnish as a binding material. Due to this method, 5 – 30 mm^3 aggregates of material had to be used rather than grinding the crystals into powder. This in theory has an effect on the thermal gradient across the sample, but this was minimal due to the slow heating rate of the cryogenic unit. The sample was then placed in the same hermetic sample holder used for the PSL measurements and mounted in the x-ray unit. 50 kV, 20 mA x-rays were applied to the sample for roughly 30 minutes.

It is important to note that irradiation was done at room temperature, and therefore the thermally unstable traps that were to be examined were empty after irradiation. To fill these low energy traps, a phototransfer technique was employed.

The sample was then taken to the cryogenic unit, under dark conditions (sample covered during transport, lights out in the lab with the cryogenic unit), and mounted on the cryogenic unit's cold finger. The cold finger consisted of a block of copper connected to the refrigerator. The cryogenic chamber was then evacuated down to a pressure of the order of $2x10^{-5}$ kPa.

The sample temperature was lowered to 25 K. Lower temperatures were possible but not considered necessary or stable enough to use. The cryogenic system was left on for the entire measurement, providing a heat sink at the base of the copper finger. A

heating coil, wrapped around the base of the copper finger, was used to heat the sample to the required temperature. The sensor connected to the cryostat temperature control unit is at a distance of 5 cm from the sample on the hot finger and so the temperature at the sample needed to be measured independently. A LakeShore low temperature diode (DT-670A-CU) was attached next to the position of the sample (approximately 5 mm distant) to provide an accurate measurement of the temperature at the actual sample using a 4-terminal technique. A constant current source (10 μA) is used to activate the diode and the resulting voltage drop across the diode is sampled simultaneously to the TSL measurements. The same ADC-16 that is used to sample the PMT output is used to record the voltage drop across the diode, using a different channel. The voltage to temperature conversion is done on the fly by the PicoLog recording software, using a 5^{th} order polynomial fit to the calibration tables.

A red laser was then used to irradiate the sample, exciting electrons from the (room temperature) thermally stable deep traps. This causes a PSL type effect, where electrons are able to recombine with holes, causing the emission of shorter wavelength light. However, some of the electrons are retrapped, at any of the thermally stable traps. After a short time, this process reaches equilibrium and the shallow traps are populated with as many electrons as possible using this process. This process allowed for low temperature TSL measurements without needing the x-ray source to be in close proximity to the cryogenic unit.

Figure 3-7 shows two trial TSL experiments performed on a sample of $BaCl_2:Eu^{2+}$, Sr^{2+} that was done during the design and testing stages of the low temperature TSL experiment. The blue plot describes the TSL run done without the stimulation of the sample with the red laser and shows no TSL signal. The green plot is the sample prepared under the same conditions but including the red laser stimulation. Here there is a TSL signal, which demonstrates the effectiveness of the phototransfer process for low temperature TSL.

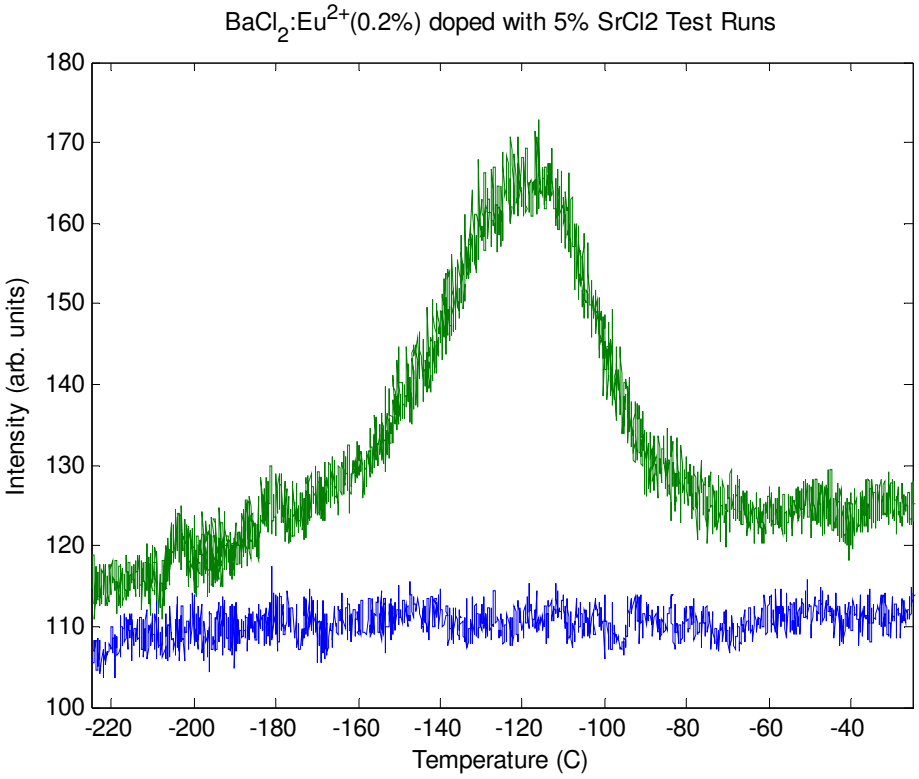

Figure 3-7: Two consecutive TSL measurements on $BaCl_2:Eu^{2+},Sr^{2+}$ using the LT-TSL system. The only difference is the green line represents a run where the red laser induced phototransfer effect is used, and the blue line this stage is omitted. As can be seen, there is a clear TSL signal after phototransfer.

3.4.1 Temperature linearity and accuracy

The temperature controller has a resolution of 0.1K, and provides good linear ramps over a range of ramping rates. Graphs of the temperature ramp are shown in figure 3-8 demonstrating the linearity of the ramp.

Due to the weak signal from the PMT, significant analogue amplification is employed. This is done in two stages, the first by electronics housed inside the PMT and then this 0-10 V signal is amplified 100x to provide a suitable signal for the ADC-16. The ADC-16 accepts a -2 to +2 V input, so it is important to not have the

amplification running with any significant light sources present. Despite the high levels of amplification, the signal to noise ratio of the data is more than acceptable, even at ramp rates as low as 0.5K/min. The noise level inferred from figure 3-8 is ±5 mV, which over a potential range of 0 to 2 V gave a typical signal to noise of approximately 0.25% for the trial experiments.

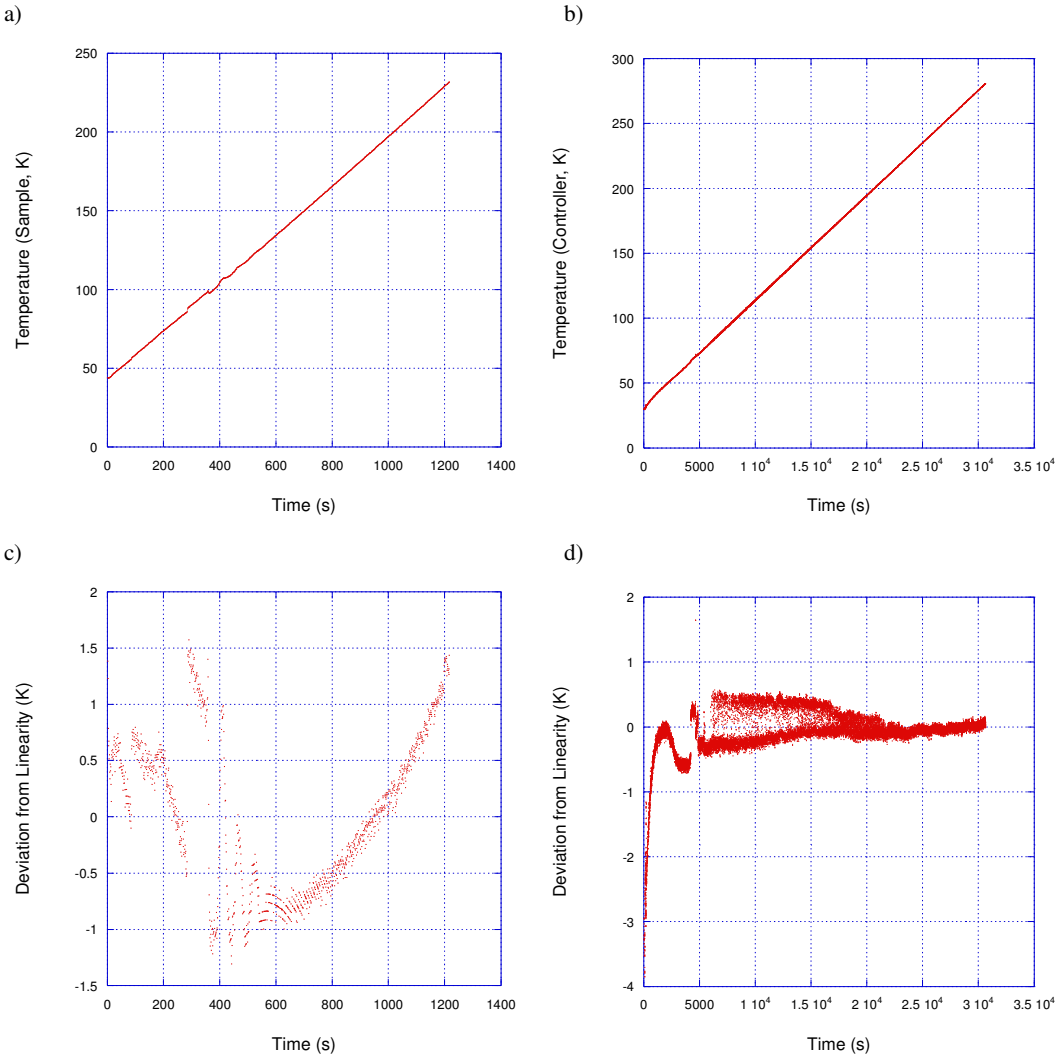

Figure 3-8: Plot of temperature data over time for a ramp rate of a) 10 K/min and b) 0.5 K/min. The respective plots c) 10 K/min, d) 0.5 K/min of deviation from linear, where linear is taken from a line of best fit through the central data points.

The data from the ADC-16 is acquired using the program “Picoscope”. The data is processed on the fly, allowing for real-time display of the temperature. The light intensity is simply measured as a voltage. The data can be loaded into the same analysis routines as the data from the HTTSL rig, and processed in the same way.

Chapter 4

Results and Analysis: Thermally Stimulated Luminescence of $BaCl_2:Eu^{2+}$ with Co-Dopants

4.1 Motivation

The lithium-borate glass ceramic neutron imaging plates containing europium (II) doped barium chloride crystals made at VUW by Appleby et al. [6] appeared to suffer from an afterglow problem during image read-out (see Chapter 1). A possible cause for this afterglow is the presence of shallow electron traps within the barium chloride crystals such that any trapped electrons are not thermally stable at room temperature.

Assuming Boltzmann statistics, a formula for the lifetime of an electron trap at temperature T is given by:

$$\tau = \frac{1}{s}\exp\left(\frac{E}{kT}\right) \tag{4-1}$$

Where s is the frequency factor and E is the energy of the trap. Both these parameters are characteristic of the particular trap.

During irradiation any shallow traps (E « kT) within the material are emptied before read-out occurs. This means only deep traps (E » kT) will be full. During read-out, it was found that light was still being emitted from a phosphor pixel after the stimulating laser had moved on to the next pixels. The scanning rate of the scanner

was of the order of 40 ms per line, and the streaks were lasting about one line before dying out, indicating that the lifetime of the glow decay of the storage phosphor was of the same order.

The purpose of this part of the research was to examine $BaCl_2:Eu^{2+}$ crystals using TSL to see if there are traps which may be associated with a time constant of the order of 10s of milliseconds which may explain the streaking effect. A second motivation was to generate a portfolio of data regarding the effect of co-dopants on trap creation which can be of use in further glass-ceramic design for radiation imaging.

4.2 Thermally Stimulated Luminescence (TSL) Study

Since TSL was a new technique to the Radiation Imaging and Detection research group at VUW, some preliminary experiments were first performed to refine the local methodology, including the application of glow curve deconvolution techniques.

Samples were irradiated at room temperature using 50 kV, 20 mA x-rays from a tungsten tube for 45 s. The TSL scheme was for a temperature ramp rate of 1 K/s, with a photon counting time of 700 ms. The temperature range was set to 40 °C to 400 °C. Samples were prepared as described in chapter 3. Figure 4-1 shows representative TSL glow curves for measurements made under these conditions.

It is encouraging that the TSL glow curves for different concentrations of the same dopant show the same general pattern and roughly reflect the dopant concentration. It is also readily apparent that different co-dopants (Na and Ca in this case) clearly generate different trap structures.

However there is a high signal to noise ratio, particularly for the 1% doped samples. This is a result of the small samples which are necessary for TSL measurements (to

minimise the effect of temperature gradients across the sample) and the short irradiation time.

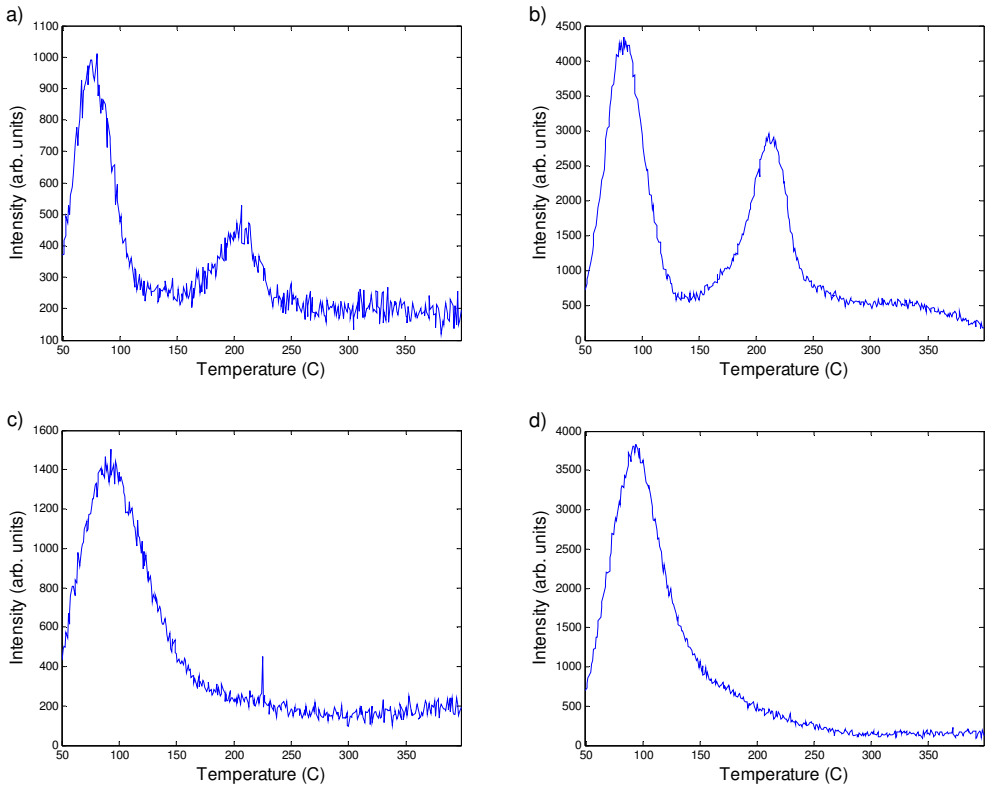

Figure 4-1: TSL measurements of $BaCl_2:Eu^{2+}$ co-doped with a) 1% NaCl, b) 5% NaCl, c) 1% CaF_2 and d) 5% CaF_2. Irradiation time was 45 s, ramp rate 1 K/s with a 700 ms photon counting time.

Representative GCD analyses of the $BaCl_2:Eu^{2+}$(0.2%), Na^+(5%) TSL glow curves are shown in figure 4-2. With GCD, it is necessary to decide on how many peaks to fit to the data, and this is not always obvious from visual inspection of the glow curve. This is because overlapping peaks can appear to be one peak, with a maximum intensity located at a temperature between the peak maxima.

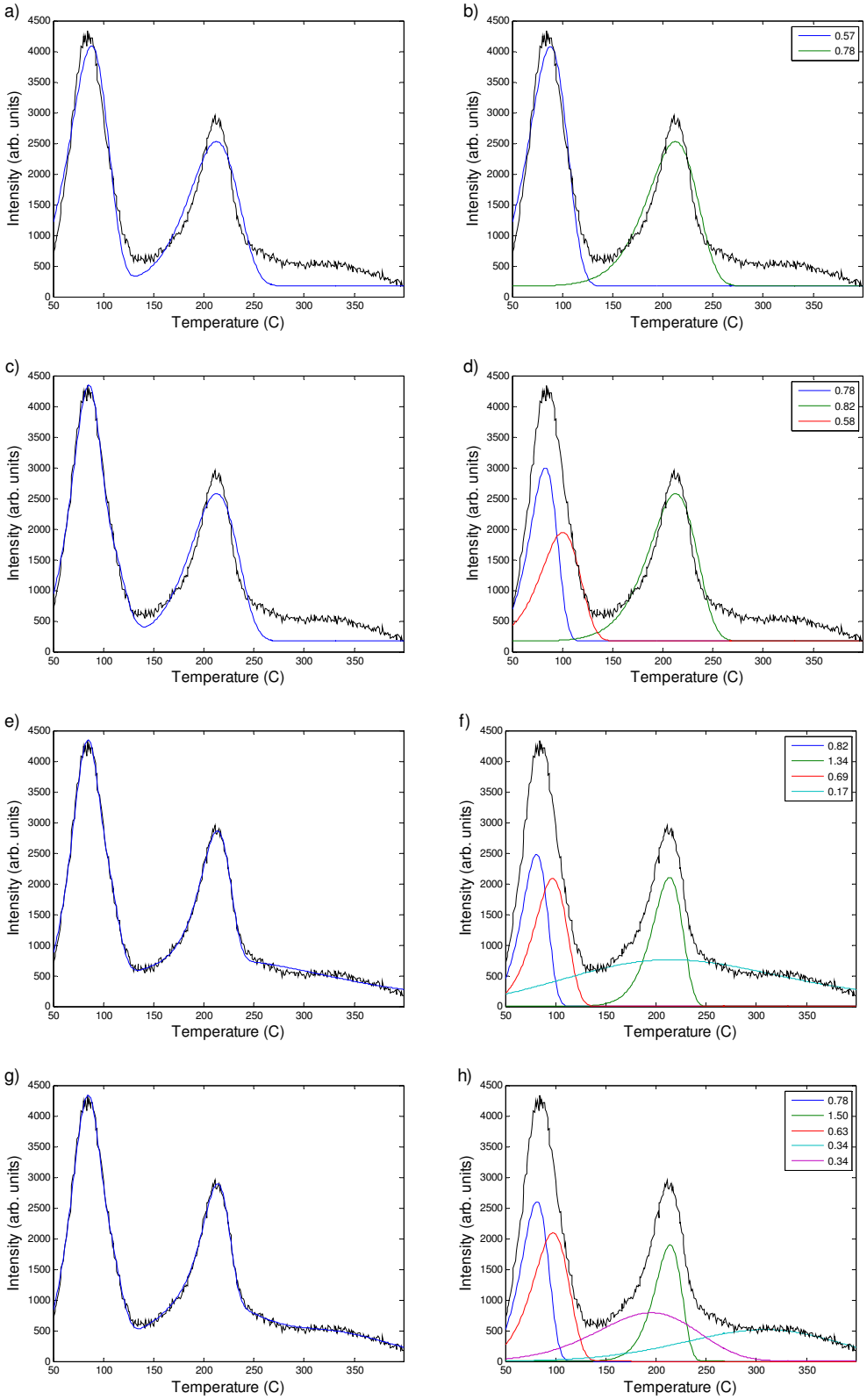
a)
b)
c)
d)
e)
f)
g)
h)
Intensity (arb. units)
Temperature (C)
0.57
0.78
0.78
0.82
0.58
0.82
1.34
0.69
0.17
0.78
1.50
0.63
0.34
0.34

Figure 4-2 (left): GCD curve fitting to a TSL glow curve of $BaCl_2:Eu^{2+}$ doped with 5% NaCl, using different numbers of fitted peaks. The complete fit is shown for a) 2 peaks, c) 3 peaks, e) 4 peaks and g) 5 peaks, while the component peaks are shown for b) 2 peaks, d) 3 peaks, f) 4 peaks and h) 5 peaks. The measurements were made at 1 K/s.

Peaks	I_{max} (arb.)	T_{max} (°C)	E (eV)	s (Hz)	FOM (%)
2	3910	88	0.57	$4.0x10^{6}$	20.4
	2360	212	0.78	$5.2x10^{6}$	
3	2830	83	0.78	$6.8x10^{9}$	16.9
	1770	100	0.58	$3.7x10^{6}$	
	2400	213	0.82	$1.3x10^{7}$	
4	2480	81	0.82	$3.6x10^{10}$	4.5
	2080	97	0.69	$1.5x10^{8}$	
	723	181	0.17	$7.6x10^{-1}$	
	2100	213	1.34	$4.6x10^{12}$	
5	2600	81	0.78	$9.3x10^{9}$	3.9
	2090	97	0.63	$2.3x10^{7}$	
	789	192	0.34	$9.7x10^{1}$	
	1900	214	1.50	$2.4x10^{14}$	
	513	300	0.34	$1.3x10^{1}$	

Table 4-1: Curve fitting parameters for a sample of $BaCl_2:Eu^{2+}$, Na^{+} for different numbers of fitted peaks.

For this work, the Figure of Merit (FOM) is defined as follows:

$$FOM\,(\%) = \frac{\sum |y_{data} - y_{sim}|}{\sum y_{data}} \times 100 \qquad (4\text{-}2)$$

As expected the goodness of fit increases as more glow curves are added, but care must be taken not to over-parameterise the fitting. In pure orthorhombic $BaCl_2$ there are two unique Cl^- sites within the unit cell. Either of these may be vacant, leaving an F-centre vacancy, so at least two peaks are justified.

Table 4-1 serves to illustrate the sensitivity of the extracted parameters E and s to the fitting process. For the 4 and 5 peak fits, it seems physically unlikely that there will be a range for the s (attempt frequency) parameters of the order of 10^{13}.

4.2.1 TSL with longer irradiation times

In order to improve the signal to noise ratio and hence the reliability of the fitting, measurements were taken with longer irradiation times. During irradiation, it is believed that F-centres and other defects are formed as a result of the radiation damage to the crystal, in addition to the defects present before irradiation. Incident x-ray photons, with relatively large momentum are able to displace ions within the lattice creating more vacancies and therefore F-centres. In this way, not only do longer irradiation times cause more excited electrons (therefore allowing for more to be trapped), but also provide a higher trapping probability.

The new irradiation time was 4 minutes, with the same 50 kV, 20 mA settings. Due to the difficulties in producing the same sample size on the TSL hot finger, direct comparison between TSL intensities of different samples is not possible, but the trap properties can be compared. Figure 4-3 shows some results for different dopants.

The improvement in the signal to noise ratio compared to figure 4-2 is immediately obvious. The problem encountered here is that the single temperature ramp rate TSL for use with solely GCD analysis is incapable of giving unique, or reliable, results for trap depths etc. This is possibly a result of the ramp rate being too high, since this will cause individual glow peaks to essentially group together. If a measured glow curve is in fact a superposition of multiple peaks, the GCD technique tends to

fail to uniquely determine the individual peak properties. To improve the analysis, multiple ramp rate measurements were made.

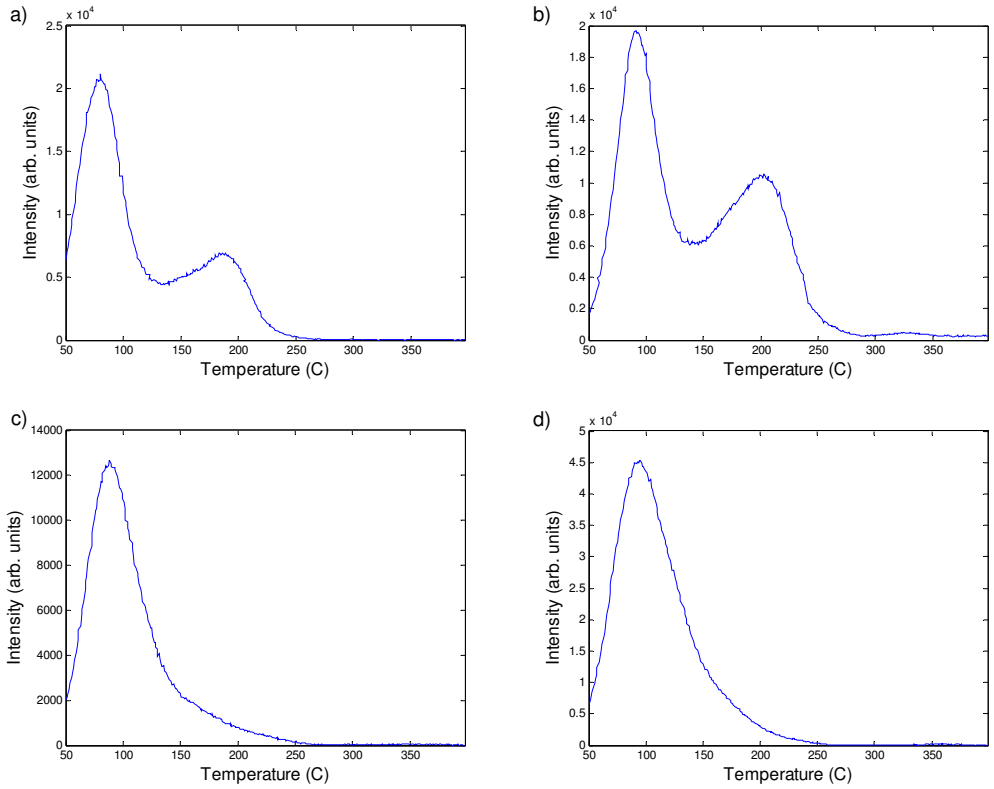

Figure 4-3: TSL measurements of $BaCl_2:Eu^{2+}$ co-doped with a) 1% NaCl, b) 5% NaCl, c) 1% CaF_2 and d) 5% CaF_2. Irradiation time was 4 minutes, ramp rate 1 K/s with a 700 ms photon counting time.

4.2.2 Multiple temperature ramp rate studies

With improvements in the TSL equipment, the ability to produce linear ramps at different rates with high data sampling rates was made possible. This enabled TSL experiments to be run with a variety of ramp rates for each sample. The advantage of a variety of ramp rates is the extra parameter allows for improved accuracy determining the trap energy and frequency factor for each trap.

Using the modified GCD deconvolution technique discussed chapter 2, multiple data sets may be analysed simultaneously, as long as the ramp rate information for each data set is supplied. Data with duplicate ramp rates are allowed with these routines. The advantage here is that the energy and frequency factor parameters are common between each data set, representing the expected physical situation where the same sample should contain the same traps. The measured trap properties should not of course depend on the temperature ramp rate.

From the trap energy, frequency factor and ramp rate information the temperature of the peak maximum can be calculated, giving parameters which may be compared to normal GCD analysis.

A sample of $BaCl_2:Eu^{2+}$ doped with 5% $CaCl_2$ is used to illustrate the advantages of using multiple ramp rate data. Figure 4-4 shows the 1 K/s TSL of this sample, indicating one major peak.

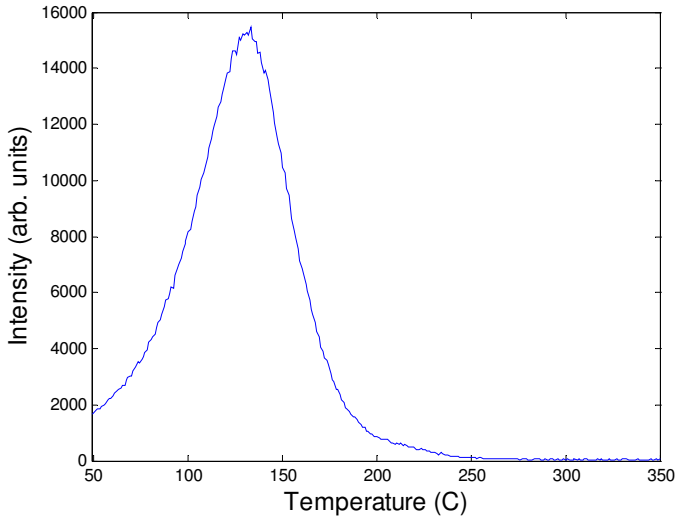

Figure 4-4: Glow curve for $BaCl_2:Eu^{2+}$, Ca^{2+}, 4 minute irradiation, 1 K/s ramp rate.

The question arises as to whether the peak observed in the glow curve is the result of a single trap, or the superposition of glow curves from several traps within the sample.

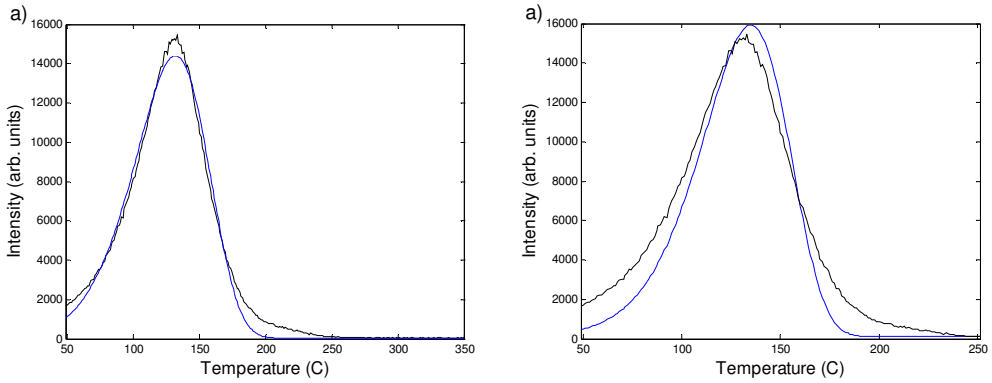

Figure 4-5: TSL peak fitting of a sample of $BaCl_2:Eu^{2+}$, Ca^{2+}, where a) is the result of single peak, single ramp rate GCD peak fitting and b) is the result of single peak, multiple ramp rate GCD peak fitting. The two displayed graphs were measured at 1 K/s.

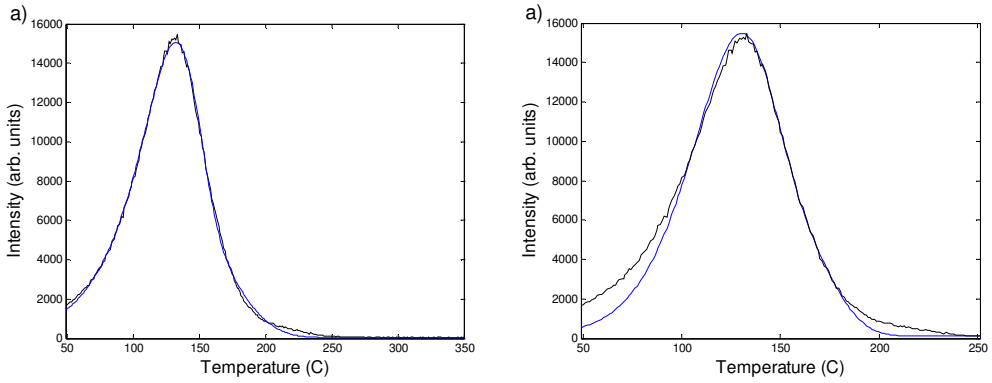

Figure 4-6: TSL peak fitting of a sample of $BaCl_2:Eu^{2+}$, Ca^{2+}, where a) is the result of two peak, single ramp rate GCD peak fitting and b) is the result of two peak, multiple ramp rate GCD peak fitting. The two displayed graphs were measured at 1 K/s.

The ramp rates used for analysing this sample are 0.50, 0.75, 1.0, 1.5, 2.0, 2.5 and 4 K/s. Figure 4-5 represents a comparison between fitting a single peak to only the 1

K/s glow curve, and the 1 K/s data when fitting a signle peak to all the glow curves simultaneously. Figure 4-6 shows the result of fitting 2 curves to the glow curve data. Table 4-2 summarises the resulting trap energies in each case. Although the fit to a single ramp rate looks more convincing, individual fits to other TSL glow curves done at the same or different ramp rates yield a wide range of values for E and s. For the Ca^{2+} doped sample shown in figure 4-5, the calculated trap energy for one fitted trap ranges in value from 0.47 to 0.56 eV, while the frequency factor varies from 7 x 10^3 to 7 x 10^5 s^{-1}. The basic difficulty arises from the strong correlation between the activation energy, E, and the frequency factor, s, in determining the glow curve shape. By introducing multiple ramp rates into the analysis, the correlation is decreased as the different ramp rates change the peak position and shape.

Number of Fitted Peaks	**Peak Number**	**Trap Energy (eV) Single GC**	**Trap Energy (eV) Multiple GC**
1	1	0.50	0.64
2	1	0.32	0.54
	2	0.69	0.63

Table 4-2: Summary of GCD parameters for peak fitting to $BaCl_2:Eu^{2+}$, Ca^{2+} using either one fitted peak or two and either normal GCD techniques or multiple ramp rate GCD (modified GCD).

The effect of making the trap energy and frequency factor parameters common amongst a collection of glow curves with varying ramp rates can best be seen in figure 4-7, which shows the effect of fitting two peaks to the sample of glow curves.

By using GCD modified to include several data sets of TSL experiments on the same sample done at different ramp rates, the goodness of fit for an overall set of experiments is reduced. The basis for constraining the trap energy and frequency factor parameters to be common amongst the different data sets is that the GCD process mirrors the physical reality that these properties of the traps within a material are independent of ramp rate.

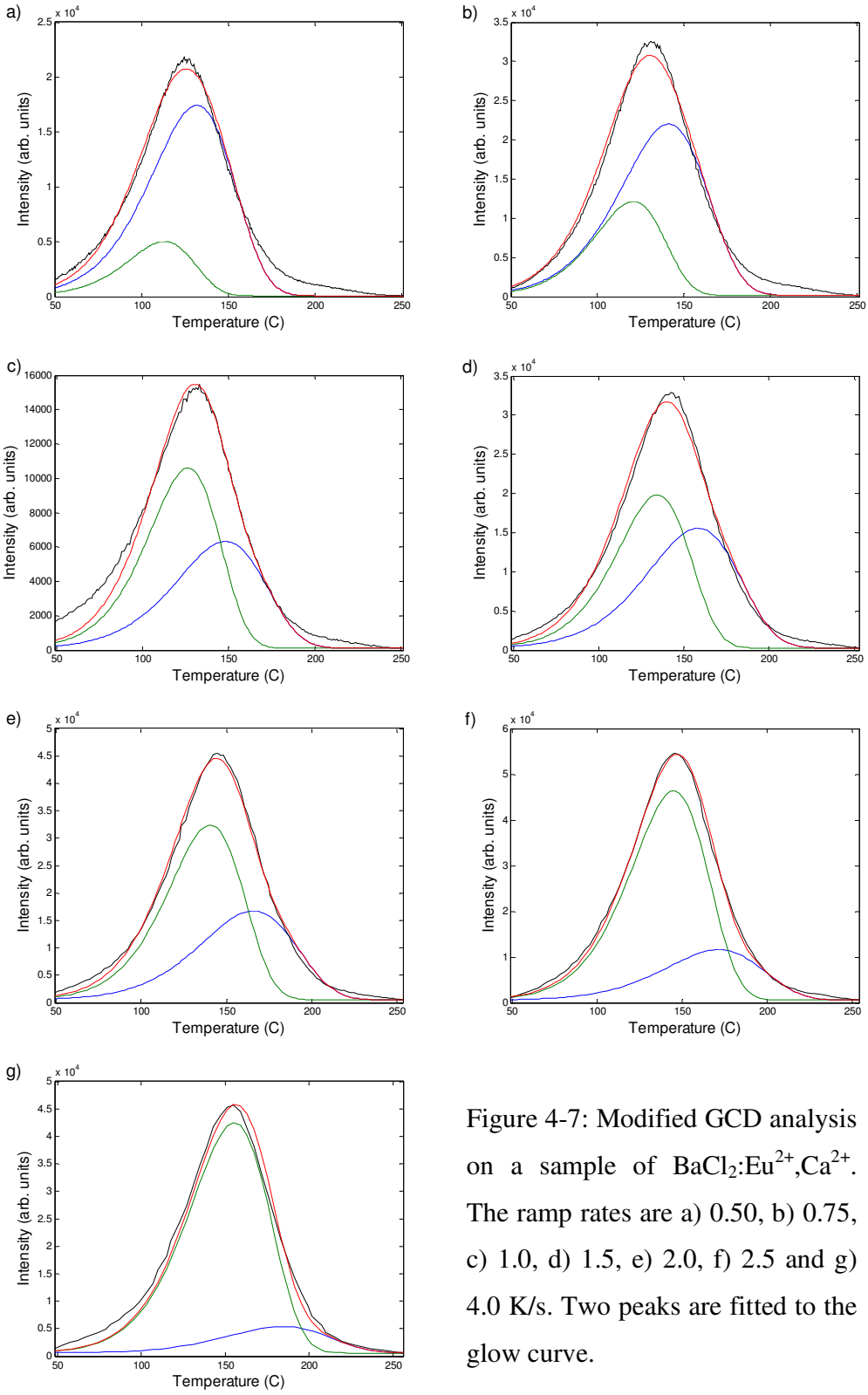

Figure 4-7: Modified GCD analysis on a sample of $BaCl_2:Eu^{2+},Ca^{2+}$. The ramp rates are a) 0.50, b) 0.75, c) 1.0, d) 1.5, e) 2.0, f) 2.5 and g) 4.0 K/s. Two peaks are fitted to the glow curve.

Examining the plots in figure 4-7, it is interesting to note that the lower temperature peak appears to increase in intensity relative to the higher temperature peak (the relative intensities were not constrained to be fixed). This may reflect the situation that the kinetics of the two defects involved are not independent of each other.

4.2.3 Trap lifetime calculations

When considering the afterglow effect seen in lithium-borate glasses produced at VUW, the lifetimes of the traps at room temperature is an important property. The lifetime is dependent on the trap energy, trap frequency factor and the sample temperature, as shown in equation (4-1).

A TSL measurement analyzed using GCD or modified-GCD techniques provides both frequency factor and trap energy information, though for GCD the frequency factor is calculated indirectly from the calculated energy and peak maximum parameters, along with the TSL heating rate. For the modified-GCD routines, the frequency factor is a fitting parameter along with the trap energy, since the temperature for peak maximum must be calculated for each different ramp rate.

Though the TSL discussed so far will give information only on traps that are stable at room temperature (since the irradiation was done at room temperature and the TSL measurements started from or just above room temperature), the lifetime information can provides clues as to what temperature range must be studied to examine traps that could be responsible for afterglows of the order of 10s of milliseconds.

Table 4-3 gives a summary of the calculated parameters for a variety of $BaCl_2:Eu^{2+}$ samples either with no additional doping or the indicated doping. The analysis is done using the modified GCD technique, and the lifetime calculations shown for temperatures of 0, 20 and 40 °C, indicated as τ_0, τ_{20} and τ_{40} respectively. The number

of peaks for each sample is the number required to give an average FOM for each glow curve of less than 5%.

Dopant	Peak Number	E (eV)	s (Hz)	τ_0 (s)	τ_{20} (s)	τ_{40} (s)
none	1	0.48	4.1×10^4	1.7×10^4	4.2×10^3	1.3×10^3
	2	0.50	7.3×10^3	2.7×10^5	6.2×10^4	1.7×10^4
	3	0.98	8.8×10^{10}	1.6×10^7	9.3×10^5	7.7×10^4
LiCl	1	0.64	2.1×10^6	3.5×10^5	5.5×10^4	1.1×10^4
	2	0.66	6.2×10^5	2.7×10^6	4.0×10^5	7.4×10^4
	3	0.75	1.3×10^8	4.6×10^5	5.3×10^4	8.0×10^3
$CaCl_2$	1	0.44	4.0×10^3	3.8×10^4	1.1×10^4	3.5×10^3
	2	0.61	1.3×10^6	1.4×10^5	2.3×10^4	5.0×10^3
	3	0.63	4.4×10^6	7.7×10^4	1.3×10^4	2.5×10^3

Table 4-3: Lifetime calculations for peaks in $BaCl_2:Eu^{2+}$ either with no additional dopant or doped with LiCl or $CaCl_2$. The peak fitting uses the modified GCD technique incorporating multiple ramp rate data.

As expected, the lifetimes for the TSL measurements made over temperature ranges exceeding room temperature are much longer than that could cause the afterglow effect. What the data does suggest is that the irradiation and subsequent TSL measurement should be performed at lower temperatures.

The TSL equipment used for the measurements so far described was therefore modified to operate from -50 °C to 450 °C. To achieve sub-room temperatures cooled dry-N_2 gas was passed over the sample. Due to equipment location and lack of portability, the cooling of the N_2 gas had to be done by passing the gas through copper piping immersed in a cooled isopropylalcohol bath. This technique was able to cool the sample to less than -50 °C, though the sample was maintained at -50 °C by the heating element of the TSL equipment. The gas was switched off at the same time the TSL experiment was begun, and since the natural warming rate of the

system was less than 1 K/s above -40 °C, the TSL experiment was begun at -40 °C with a ramping rate of 1 K/s, ensuring the temperature ramp was linear. Irradiation was performed while the sample was held at -50 °C.

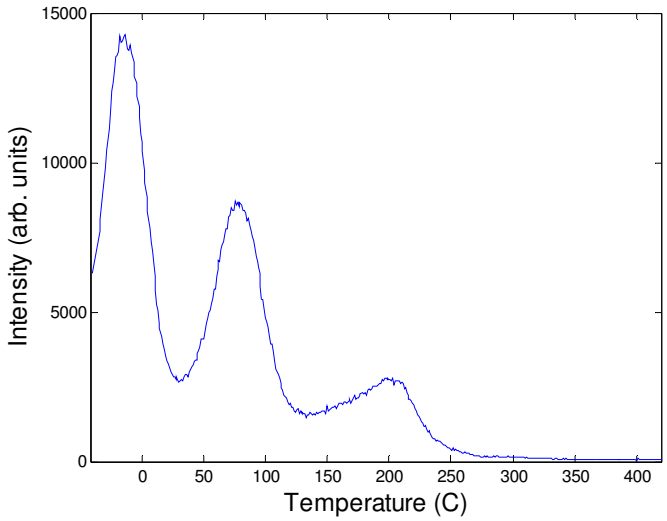

Figure 4-8: The glow curve for a sample of $BaCl_2:Eu^{2+}$, Na^+, measured over the temperature range from -40 °C to 420 °C at 1 K/s.

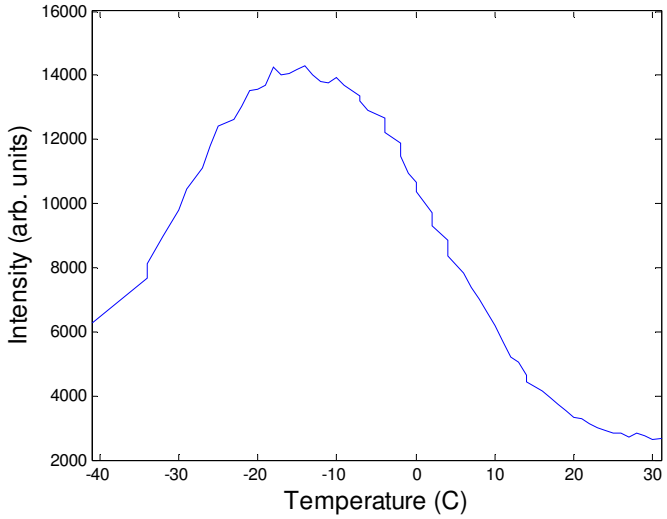

Figure 4-9: The -20 °C peak in the TSL of $BaCl_2:Eu^{2+}$, Na^+, measured at 1 K/s.

Typical TSL glow curves for $BaCl_2:Eu^{2+}$, Na^+ are shown in figures 4.8 and 4.9. It is immediately apparent that a new glow curve peak is evident below 0 °C corresponding to a trap which is not thermally stable at room temperature.

Though this data consists of the glow curve for only one ramp rate, an estimate of the lifetime can be made using normal GCD techniques. The main issue here is that the lifetime calculation is dependent on the frequency factor and trap energy, which represents two parameters obtained from one data set. The lifetime for the trap associated with this peak is found to be approximately 1.5 s at 20 °C, although this is subject to the uncertainties implicit in single curve analysis. This is approximately two orders of magnitude larger than what is expected for the afterglow effect, and indicates that this trap is not involved an the afterglow effect.

Considering this result, a new method for performing TSL at temperatures much lower than room temperature was required. This became the focus of further work, and as such there are no variable temperature ramp rate TSL measurements done on any samples using the regular TSL equipment.

4.3 Ultra Low Temperature TSL

Using a newly designed TSL technique and equipment, sub-room temperature TSL measurements were made. These are referred to as "LT-TSL" to distinguish from measurements made with the room temperature rig ("HT-TSL").

The motivation for these experiments came from the results of the HT-TSL experiments that suggested that the equipment was unsuitable for looking for traps with lifetimes at room temperature in the 10's of milliseconds range. This is not surprising since the HT-TSL equipment was originally designed for doing TSL experiments starting from room temperature. This means any glow curves measured would be from traps that are thermally stable at room temperature.

With the LT-TSL it is possible to perform TSL measurements over a range of approximately 25 – 380 K, though in practice all runs were done from 25 K through to 280 K. The technique relies on populating room temperature stable traps, and then at low temperatures (25 K) using a photo-transfer technique to populate the now stable low energy traps that quickly depopulate during sample irradiation at room temperature. Above 280 K, the room temperature stable traps begin to depopulate. This quickly saturates the measurement equipment, as there is a much larger concentration of electrons in deep traps compared to the shallow traps, and therefore the resulting TSL intensity is much larger.

4.3.1 $BaCl_2:Eu^{2+}$, Li^+

The most intensely studied sample was $BaCl_2$ doped with 5% LiCl and 0.2% $EuCl_2$. This is because Li^+ represents the most likely dopant when $BaCl_2:Eu^{2+}$ is grown inside lithium-borate glasses.

For all previous LT-TSL experiments, it was found that 100x analogue amplification of the PMT signal was generally required. For this sample though, the 100x amplification was found to be too large for most ramp rates, resulting in clipping. For all but the 0.5 K/min data, 10x amplification was used.

Figure 4-10 shows the data obtained from five different TSL experiments done on the $BaCl_2:Eu^{2+}$, Li^+ material. The LT-TSL equipment is limited to a maximum heating rate of 0.17 K/min, resulting in slower ramp rates overall when compared to the HT-TSL.

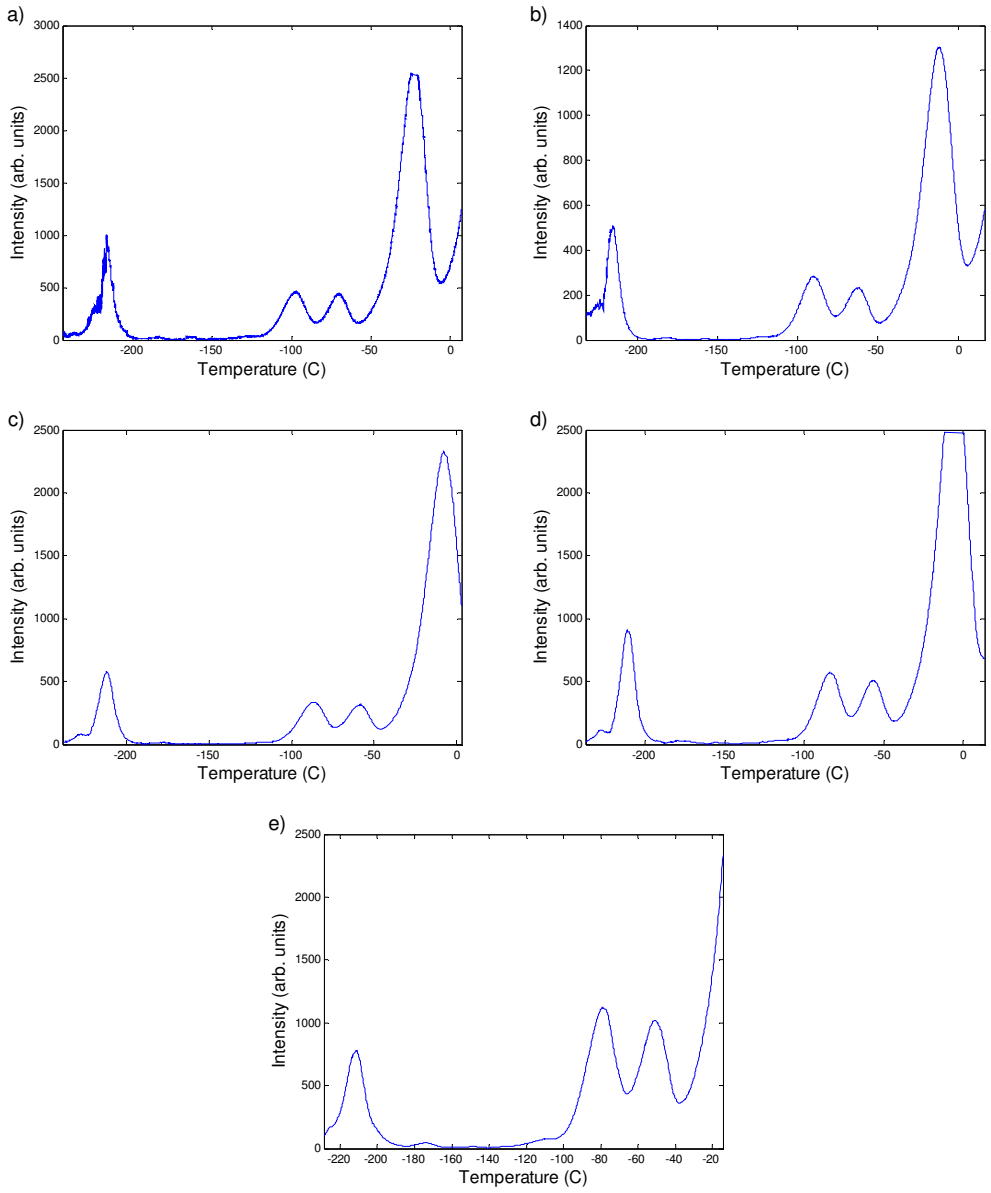

Figure 4-10: Glow curves of a sample of $BaCl_2:Eu^{2+},Li^+$, at ramp rates of a) 0.5, b) 2.5, c) 4.0, d) 5.0 and e) 10 K/min (0.0083, 0.033, 0.042, 0.067, 0.083 and 0.17 K/s respectively).

It appears from observation of the glow curves that the experiment is repeatable and consistent. This is important as it supports the validity of this technique for obtaining TSL curves. The features below -200 °C are difficult to analyse because the temperature ramp typically is not as stable as for the rest of the experiment. The

features above -200 °C are both well defined and interesting as it is suspected these can contribute to the afterglow seen during PSL readout.

The apparent low signal part of the glow curve between approximately -190 °C and -100 °C can be expanded, revealing some small peaks as shown in figure 4-11 for the 10 K/min data. This demonstrates the excellent signal to noise ratio available with this technique.

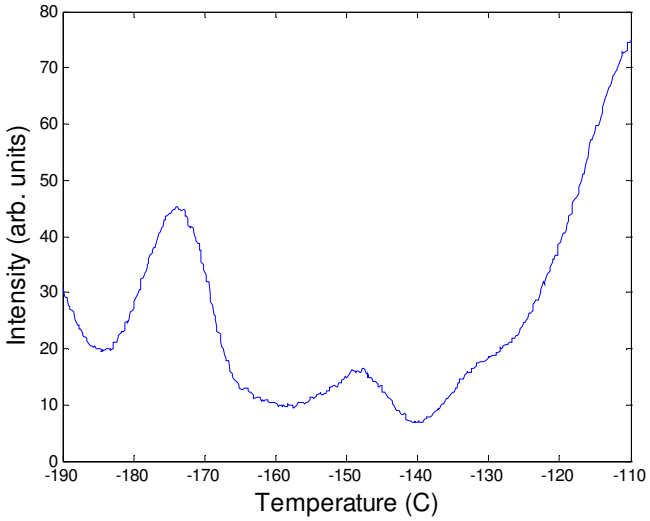

Figure 4-11: The low intensity section of the LT-TSL of BaCl2:Eu^{2+}, Li^{+}, between -190 and -100 °C.

Figure 4-12 focuses on the two well defined peaks between approximately -100 and -40 °C (for the 10 K/min data, the peaks are at lower temperatures for lower ramp rates). Normal GCD analysis gives an estimate of the associated trap lifetimes at 20 °C as shown in table 4-4.

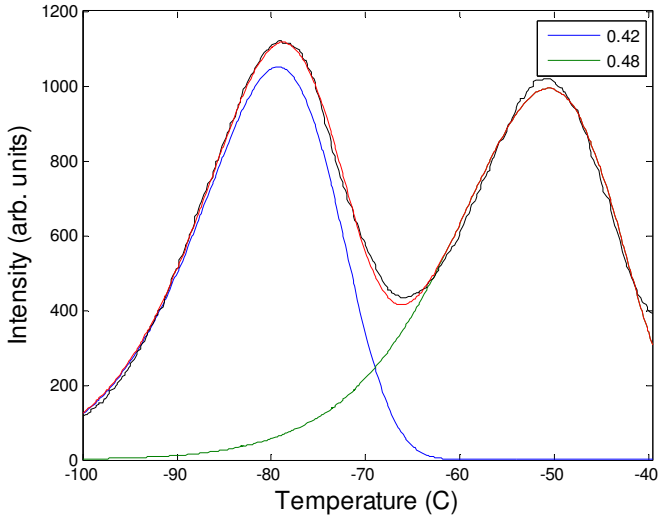

Figure 4-12: Peak fitting to the two peaks in $BaCl_2:Eu^{2+}$, Li^+ within the range of approximately -100 to -40 °C.

Peak	Trap Energy (eV)	Frequency Factor (Hz)	Trap Emptying Time Constant at 20 °C (ms)
1	0.42	2.2×10^9	3.0
2	0.48	1.1×10^9	41

Table 4-4: The calculated trap parameters for two of the peaks in $BaCl_2:Eu^{2+}$, Li^+, measured using the LT-TSL equipment.

This initial result is promising when considering the afterglow problem, as it suggests there are some significant traps that at room temperature would give decay lifetimes of the order of those seen in the lithium-borate imaging plates that had been tested earlier.

Further analysis requires incorporation of all the TSL data, acquired over different ramp rates. Each data set is reduced to cover only the two peaks analysed for the 10 K/min data, and the common E and s parameters are initially estimated from those from the same GCD analysis. As described in chapter 2, the only parameters unique to each data set are the peak intensities, and these are given starting values of the

same order as the apparent peak heights for each data set. The resulting fitted curves are shown in figure 4-13.

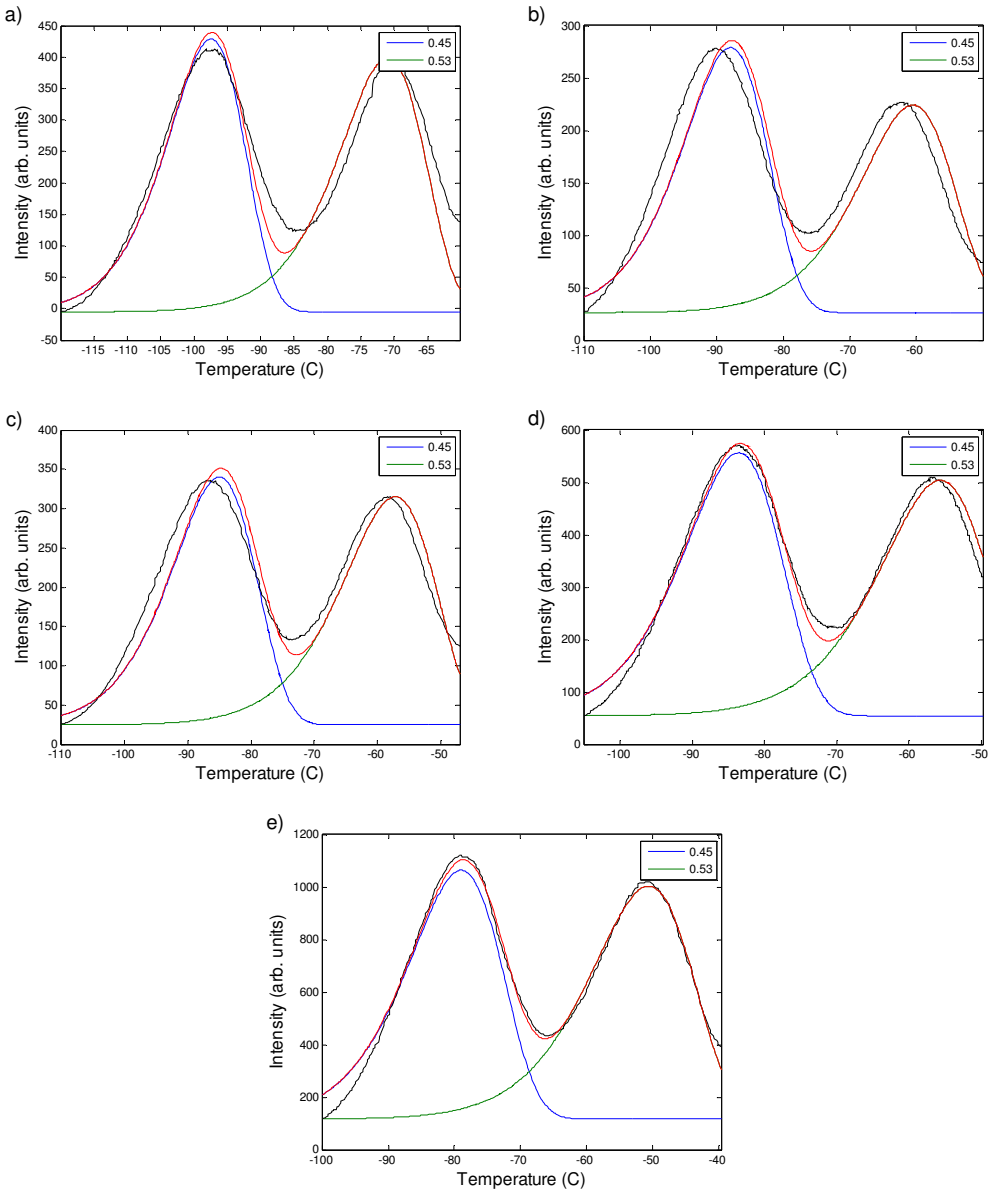

Figure 4-13: Modified GCD analysis on two of the peaks in $BaCl_2:Eu^{2+}$, Li^+. Each peak is fitted with 1 glow peak. The ramp rates were a) 0.50, b) 2.5, c) 4.0, d) 5.0 and e) 10 K/min.

Peak	Trap Energy (eV)	Frequency Factor (Hz)	Trap Emptying Time Constant at 20 °C (ms)
1	0.45	8.2×10^9	5.5
2	0.53	2.4×10^{10}	59

Table 4-5: The calculated trap parameters for two of the peaks in $BaCl_2:Eu^{2+}$, Li^+ measured with the LT-TSL equipment using the multiple GCD analysis technique.

The resulting peak parameters shown in table 4-5 are in reasonable agreement to the single glow curve analysis parameters from table 4-4. The results should of course be similar; though the multiple curve fitting results are expected to be more accurate as more data is available during analysis.

The results suggest that there are two traps within lithium co-doped $BaCl_2:Eu^{2+}$ that could be contributing to the afterglow affect seen during image read-out. Lithium is important as in LiBO glasses there is lithium in the environment during $BaCl_2$ crystal growth which may be taken up into the storage phosphor crystals.

4.3.2 $BaCl_2:Eu^{2+}$, Mg^{2+}

Several experiments were done on magnesium doped $BaCl_2:Eu^{2+}$ during the testing of the LT-TSL system. Magnesium is interesting to compare to lithium, both are small ions (~.74 Å for Li^+ compared to ~.89 Å for Mg^{2+}) but the lithium ion is monovalent and the magnesium ion is divalent. Since it is expected that these dopants substitute for Ba^{2+} in the crystals, it should be expected that the effects between the two should be reasonably different (as Li^+ is effectively introducing an extra -1 charge by substituting for a +2 cation).

The magnesium doped sample was opaque, and therefore the luminescence signal during these experiments was much lower than that for the lithium doped material, and 100x analogue amplification of the PMT signal was used for every measurement.

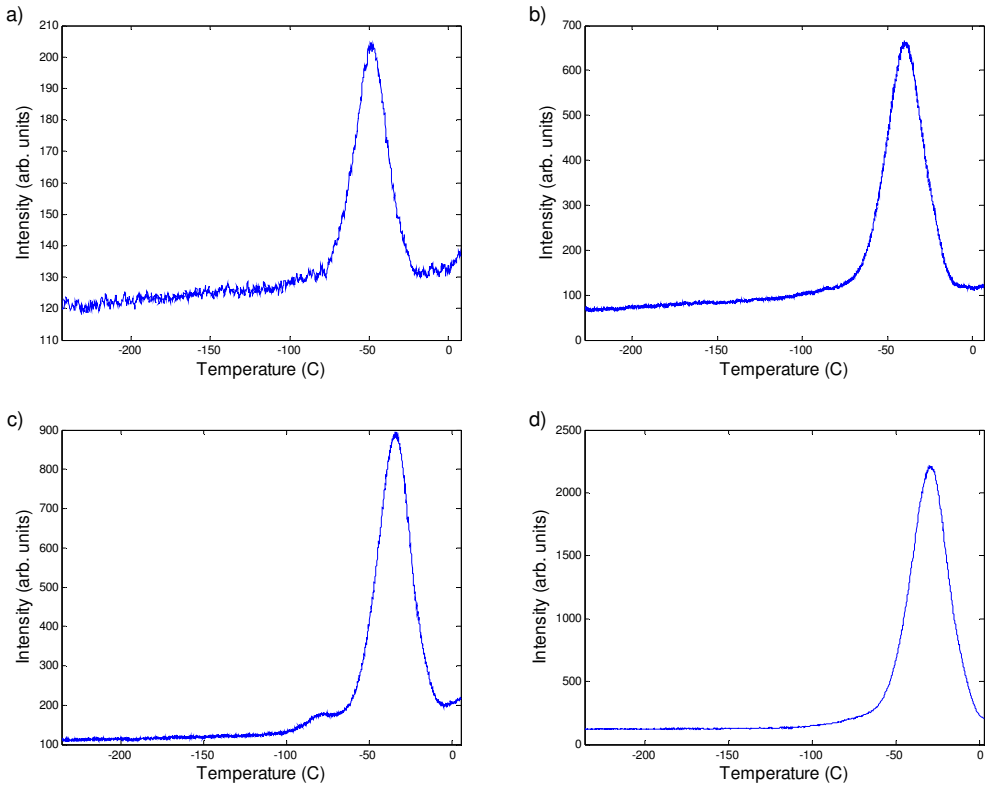

Figure 4-14: LT-TSL measurements on $BaCl_2$:Eu^{2+}, Mg^{2+} with ramp rates of a) 0.5, b) 1.5, c) 2.5 and d) 5.0 K/min.

Figure 4-14 shows the TSL data for several different temperature ramp rates. All show one predominant glow peak centred around -50 °C, (but whose peak temperature naturally varies depending on the ramp rate).

It is necessary to decide whether the large peak in the data is made up of a single glow peak or a superposition of more than one. Even the slowest ramp rate of 0.5 K/min shows only a single obvious peak, so it requires the glow curve deconvolution technique to determine whether one or two peaks provide the better fit.

Figure 4-15 shows the results of fitting one or two peaks to the 2.5 K/min data. Fitting two peaks provides a much better fit, and this is backed up by the figure of merit which is 6% for one glow peak and 0.6% for two.

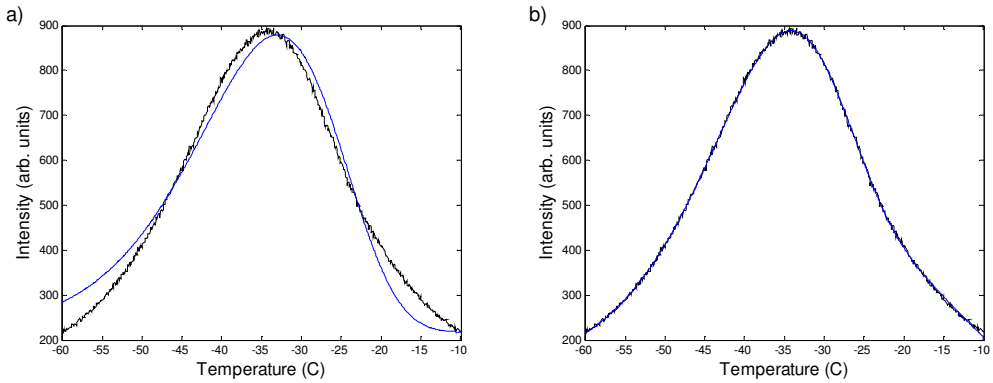

Figure 4-15: Fitted glow curve compared to measured glow curve for measurements made on $BaCl_2:Eu^{2+}$, Mg^{2+}, focusing on one peak with a) one fitted glow peak and b) two fitted glow peaks.

Using the parameters acquired for the 2.5 K/min data fitted with two glow peaks, figure 4-16 shows the result of using the modified GCD analysis on the collection of TSL data.

The properties obtained from the GCD fitting are summarised in table 4-6. As can be seen, the trap energies are typically higher than for the lithium doped material, and the corresponding lifetime at room temperature is significantly longer. It is expected that a trap emptying lifetime of the order of seconds will not cause a problem for image read-out, as the long lifetime means reduced afterglow intensity straight after laser stimulation and the long time means that the afterglow does not change much during the scan time, so may easily be subtracted as a constant background. Magnesium would only be present as an accidental impurity in the LiBO glasses.

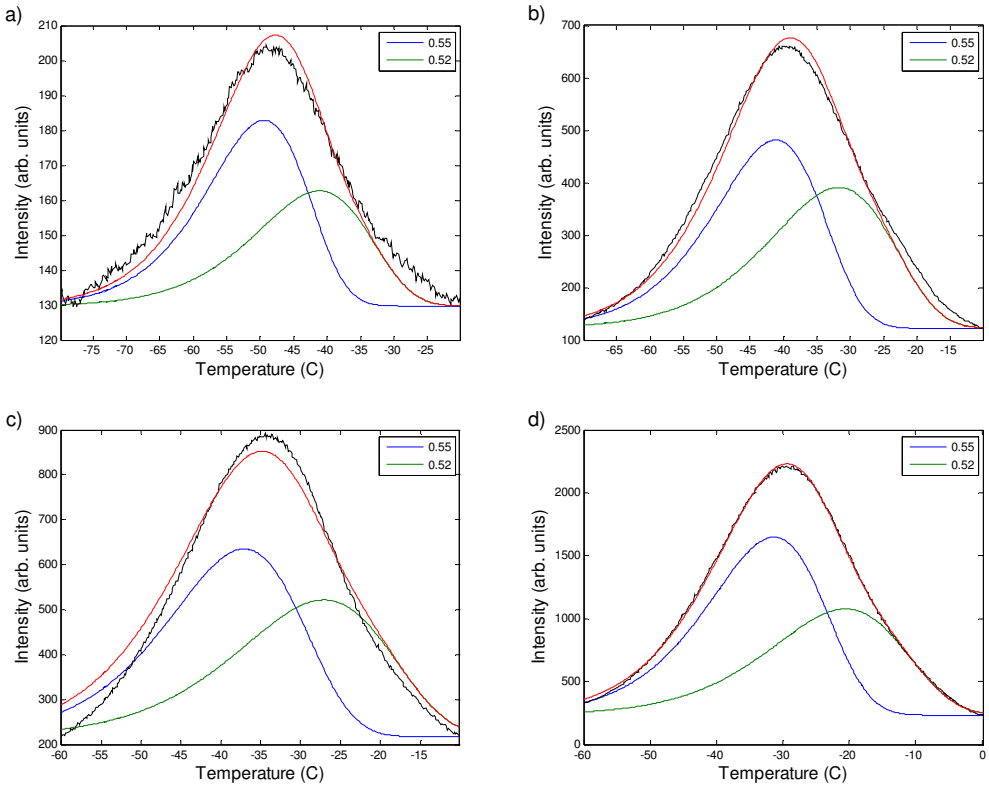

Figure 4-16: Two peak fitting to the significant glow peak in the LT-TSL of $BaCl_2:Eu^{2+}$, Mg^{2+}, for various ramp rates. Fitting is done using the modified GCD techniques.

Peak	Trap Energy (eV)	Frequency Factor (Hz)	Trap Emptying Time Constant at 20 °C (ms)
1	0.55	3.3×10^9	1000
2	0.52	2.3×10^8	4500

Table 4-6: Calculated trap properties from fitting two peaks to the main peak in the LT-TSL of $BaCl_2:Eu^{2+}$, Mg^{2+}.

4.3.3 $BaCl_2:Eu^{2+}$, Ca^{2+}

The final set of data is for $BaCl_2:Eu^{2+}$, Ca^{2+}. This data is shown in figure 4-17. It is interesting to observe that the TSL is a very different shape when compared to the other LT-TSL data.

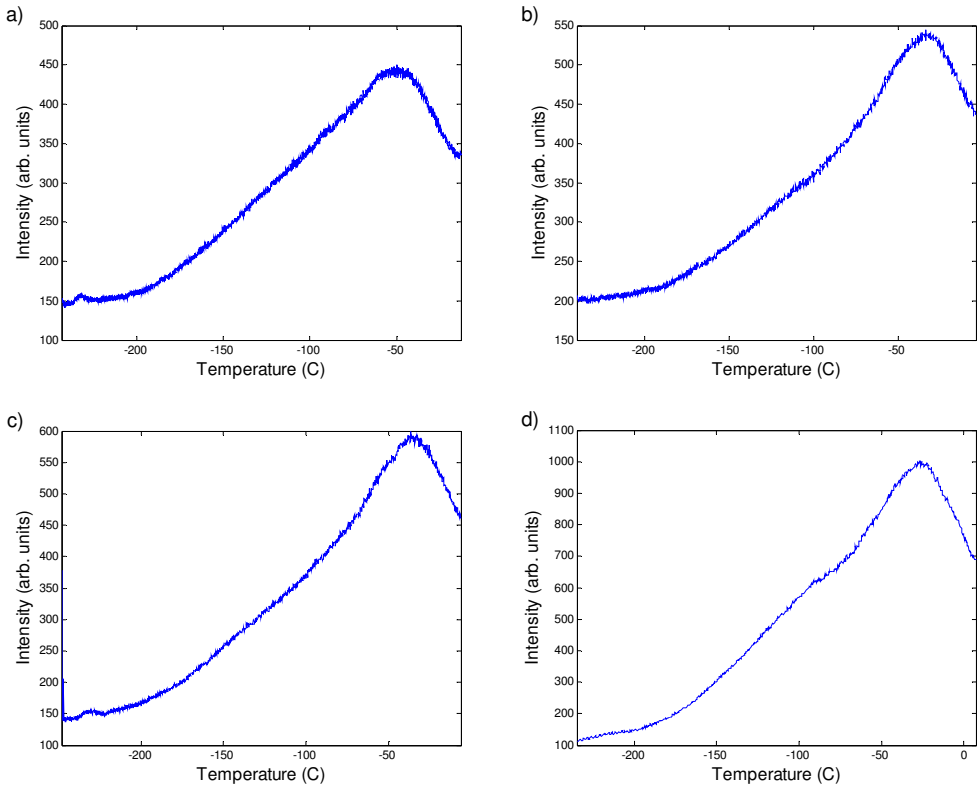

Figure 4-17: The measured glow curves for $BaCl_2:Eu^{2+}$, Ca^{2+} with ramp rates of a) 2.5, b) 5.0, c) 7.5 and d) 10 K/min.

TSL curve fitting using the MATLAB GCD routines was found to be inadequate when applied to this data. This stems from the unusual shape of the composite glow curve and the result was that the only fitting that gave results was with three fitted glow curves. Table 4-7 and figure 4-18 summarise the acquired TSL parameters after the three curve fitting.

Peak	Trap Energy (eV)	Frequency Factor (Hz)	Trap Emptying Time Constant at 20 °C (ms)
1	0.059	5.3×10^{-1}	20
2	0.11	1.4×10^{0}	43
3	0.23	1.7×10^{2}	31

Table 4-7: The fitted trap parameters for $BaCl_2:Eu^{2+}$, Ca^{2+}.

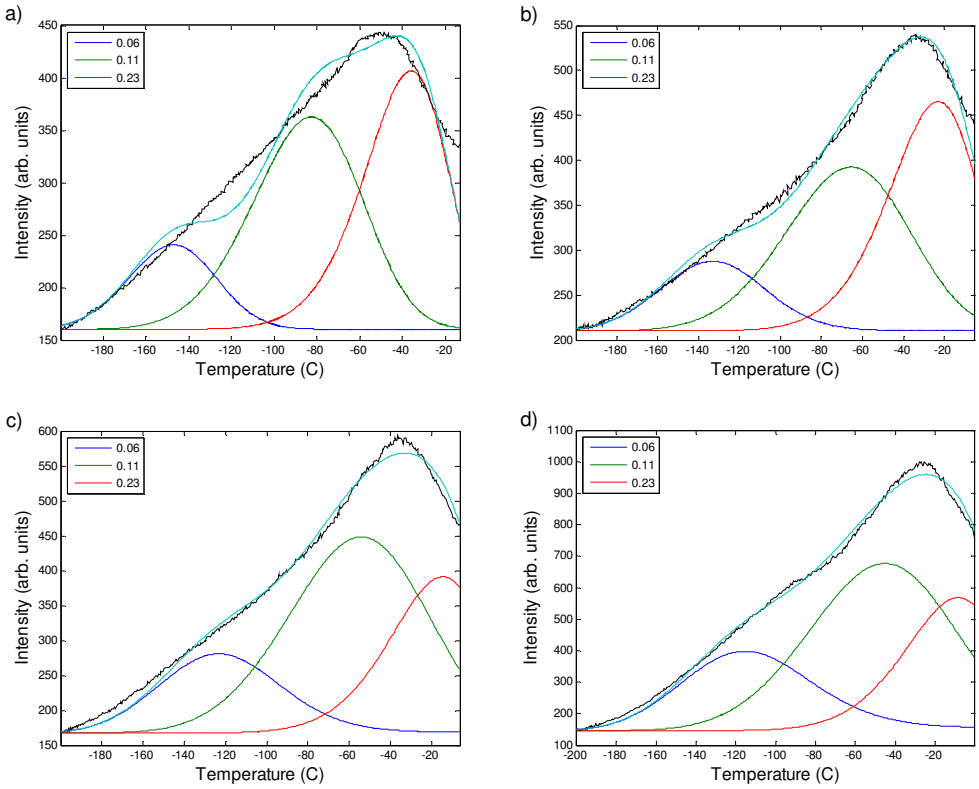

Figure 4-18: TSL of $BaCl_2:Eu^{2+}$, Ca^{2+} with 3 peak GCD curve fitting. The ramp rates are a) 2.5, b) 5.0, c) 7.5 and d) 10 K/min.

It can be seen that the frequency factors are very low when compared to the results for $BaCl_2:Eu^{2+}$, Mg^{2+} and $BaCl_2:Eu^{2+}$, Li^{+}. This suggests that the GCD curve fitting may not be working as it should with this data set, as frequency factors are generally expected to be much higher than the values obtained for this sample. However it is possible the low trap energies are evidence of a trap system which decays by phonon assisted quantum mechanical tunnelling rather than thermally activated mechanisms. Thermal bleaching techniques might allow for better peak resolution.

4.4 Peak Defect Assignment

4.4.1 High temperature TSL

It is challenging with the data obtained in this work to assign defect types within the crystal to the peaks that are observed in TSL. Previous work by Secu et al. found two main peaks in the TSL of $BaCl_2:Eu^{2+}$ [26]. The temperature range for the TSL in that work was from room temperature to 300 °C at 2 K/s. The temperatures of the peak maxima were found to be at 130 °C and 255 °C and the calculated activation energies were (1.05 ± 0.05) eV and (1.35 ± 0.05) eV respectively.

Secu et al. [26] assign the two TSL peaks to the two different F centre sites available in orthorhombic $BaCl_2$. These two sites are due to the two different Cl^- sites in $BaCl_2$, one with 4 nearest neighbours and the other with 5. It is assumed for this work that the site with 4 nearest neighbours will correspond to a lower trapping energy since the positive Madelung potential will likely be less; this F centre is labelled here F_4, whilst the other site with 5 nearest neighbours is labelled F_5.

Since the majority of the data obtained in this work was measured at a ramp rate of 1 K/s, an estimate of the peak position at the lower ramp rate is required for comparison of the data presented here with that of Secu et al. [26]. This can be done by using the glow curve equations of Kitis et al. [22] which are discussed in chapter 2. The following equation relates the trap properties to the ramp rate and glow curve maximum temperature.

$$\frac{\beta E}{kT_m^2} = s\exp\left(-\frac{E}{kT_m}\right) \tag{4-3}$$

Of the variables in (4.3), only β and T_m are expected to be different when the same material is measured for TSL using different ramp rates. E and s are properties of the trap within the material, and should be the same for the same material. Assuming this, it can be shown that for two experiments run at different ramp rates, the following ratio should apply.

$$\frac{\beta_1 T_{m2}^2}{\beta_2 T_{m1}^2} = \exp\left(-\frac{E}{k}\left[\frac{1}{T_{m1}} - \frac{1}{T_{m2}}\right]\right) \tag{4-4}$$

Here the subscripts 1 and 2 represent the parameters for the first and second TSL experiments. The equation cannot be solved analytically and therefore numerical methods are used. Using equation (4-4), the corresponding temperatures for the peak maxima if the experiments had been performed at ramp rates of 1 K/s are found to be at 122 °C and 242 °C.

Figure 4-19 shows the TSL measurement for a sample of $BaCl_2:Eu^{2+}$ measured at 1 K/s, indicating two obvious peaks. If it is assumed that there are two peaks present in this data, the two peak positions obtained are at 130 °C and 189 °C. The lower temperature peak seems to correspond to the Secu et al. [26] lower peak, though it occurs at a slightly higher temperature than the calculated peak temperature of 122 °C. The second peak does not appear to correspond to the higher temperature peak of 255 °C.

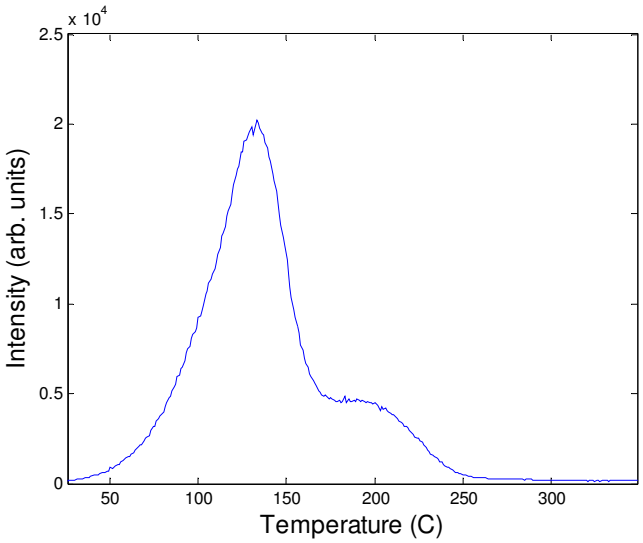

Figure 4-19: TSL glow curve of $BaCl_2:Eu^{2+}$. The measurement was performed at 1 K/s.

There are some data sets recorded here containing a peak at approximately the calculated temperature of 242 °C, two of these are shown in figure 4-20. Houlier et al. [27] suggest that only the F_4 sites are populated in their samples of $BaCl_2:Eu^{2+}$ after irradiation. It is possible that the F_4 sites are favourably created in $BaCl_2:Eu^{2+}$, and therefore the F_5 only shows in some samples.

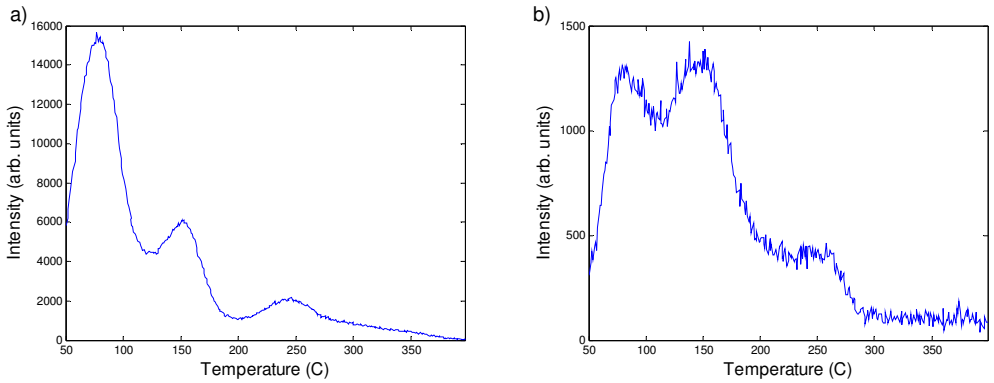

Figure 4-20: TSL glow curves for a) Rb^+ and b) K^+ co-doped $BaCl_2:Eu^{2+}$, measured at 1 K/s.

The 189 °C peak in figure 4-19 is difficult to explain in this context, since if the F_4 and F_5 centres are ascribed to different peaks, this one is still unidentified. Looking at alkaline doped $BaCl_2:Eu^{2+}$ is useful at this point. Figure 4-21 shows some examples of TSL experiments on samples of $BaCl_2:Eu^{2+}$, X^+, where X^+ is one of Na^+, K^+, Rb^+ or Cs^+. A common feature for these glow curves is a peak located between 125 and 225°C, though the exact position of the peak varies depending on dopant.

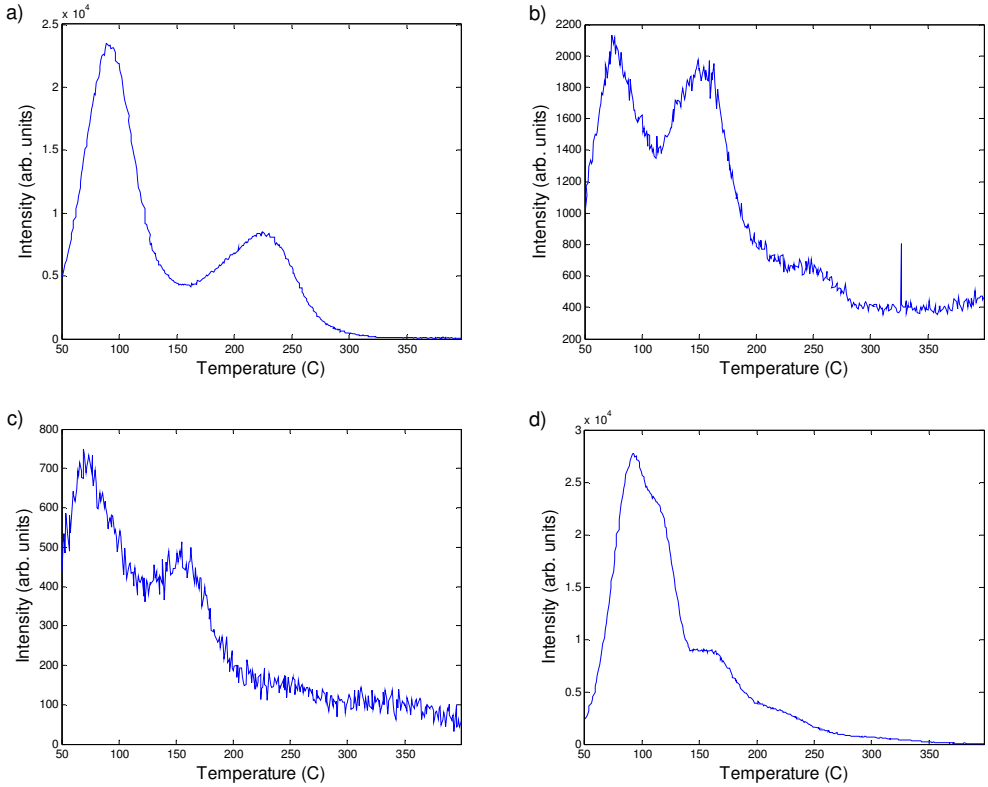

Figure 4-21: The TSL glow curves of alkaline co-doped $BaCl_2:Eu^{2+}$. The dopings are a) Na^+, b) K^+, c) Rb^+ and d) Cs^+. Measurements performed at 1 K/s.

It is assumed that the X^+ ion substitutes for Ba^{2+} for the alkaline ions listed previously (it appears that Li^+ may not fit this pattern, possibly due to the small size of the ion). In this case, a Cl^- vacancy with an X^+ as one of its nearest neighbours will have a significantly different potential when compared to an unmodified F centre, as the X^+ impurity will correspond to an effective -1 charge. The result is a

F_A centre, with the two possible centres labelled F_{A4} and F_{A5}. Here we assign the low temperature peak between 50 and 110 °C to the F_{A4} centre, and the peak between 125 and 225 °C to the F_{A5} centre.

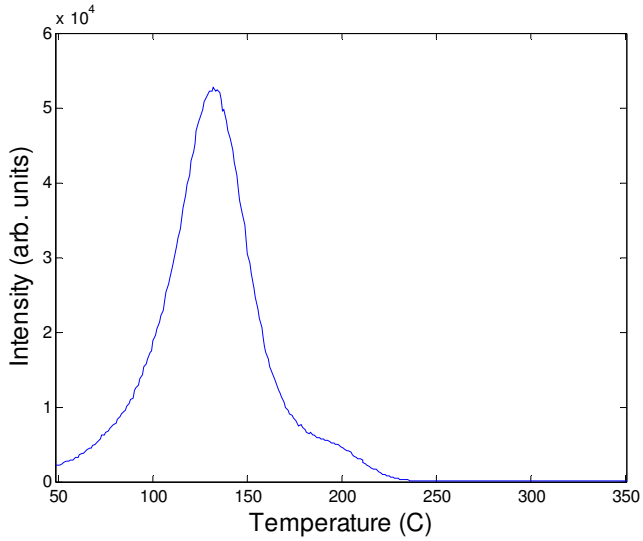

Figure 4-22: The TSL glow curve of $BaCl_2:Eu^{2+}$, Li^+, measured at 1 K/s.

Figure 4-22 shows the glow curve measured for $BaCl_2:Eu^{2+}$, Li^+. Unlike the other alkaline doped samples, there is no apparent peak in the region between 0 and 100 °C, and the glow curve resembles the $BaCl_2:Eu^{2+}$ glow curve. This could be due to the small size of the Li^+ ion resulting in it being unable to substitute for a Ba^{2+} ion, with the Li^+ ion instead taking up an interstitial position in the lattice.

It is possible that unintended impurities in the $BaCl_2:Eu^{2+}$ resulted in the presence of F_A centres that caused the peak at 189 °C in the $BaCl_2:Eu^{2+}$ TSL.

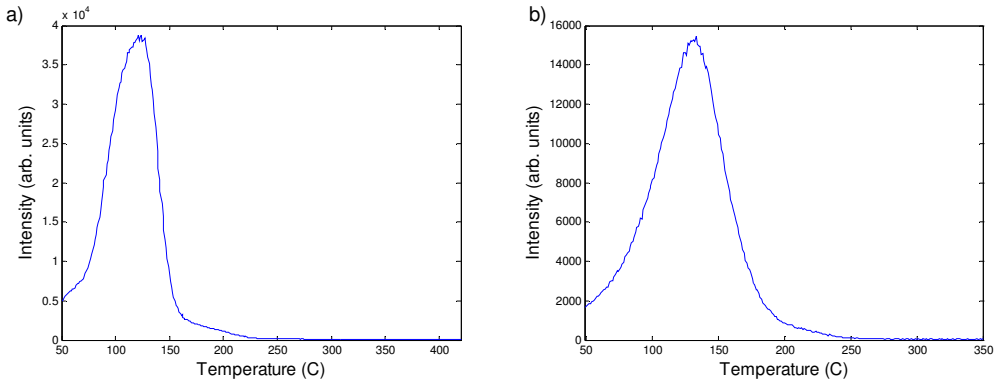

Figure 4-23: The TSL glow curves of a) Mg^{2+} and b) Ca^{2+} co-doped $BaCl_2:Eu^{2+}$. Measurements performed at 1 K/s.

Figure 4-23 shows glow curves of Ca^{2+} and Mg^{2+} doped $BaCl_2:Eu^{2+}$. There is only one obvious peak in both cases, though other peaks may be located within it. Since the intentional dopings in both cases are the same charge as Ba^{2+}, it is not expected that F_A centres would be formed. It is likely that any alkaline impurities present are in minority when compared to the intentional doping and therefore any F_A associated peak will be much smaller than F based peaks. Since it is expected that the F_A centres will have a lower trap energy compared to the corresponding F centre, the peak located between 125 and 225 °C is ascribed to the F_{A5} centre.

When considering the alkaline doped samples in figure 4-21, the largest peak in each case is at a relatively low temperature, less than or around 100 °C. Since these peaks are close to room temperature, it is expected that they correspond to traps which are not stable at room temperature. It seems likely that the peaks are associated with the F_{A4} centre, since the peak position appears to be dopant dependent.

The low temperature nature of the main peak in the X^- doped materials is interesting and has implications for the storage phosphor efficiency for samples containing alkaline impurities. This shall be discussed in more detail in chapter 5.

4.4.2 Low temperature TSL

The low temperature TSL data is difficult to ascribe defect types to as there is less data available compared to the HT-TSL data. Since the F centres have been associated with peaks present in the HT-TSL data, the LT-TSL glow curves require a different assignment. Figure 4-24 shows examples of the peaks present for the Li^+ and Mg^{2+} doped samples. Both data sets have a large peak above -50 °C, the Li^+ doped sample has this peak at approximately -11 °C while the Mg^{2+} sample has this peak at -35 °C.

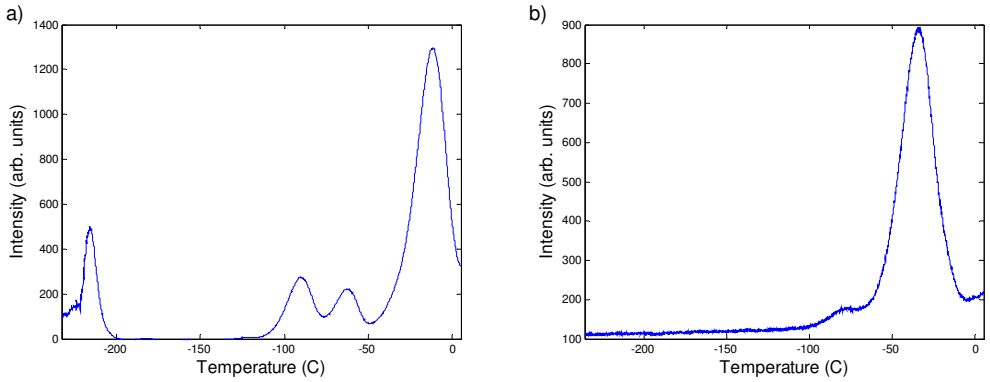

Figure 4-24: The LT-TSL glow curves of $BaCl_2:Eu^{2+}$ co-doped with either Li^+ or Mg^{2+}.

A possible cause for these low temperature peaks are complexes of vacancies with trapped electrons known as M centres. These have been studied in detail in alkaline halide crystals [28] but their presence in $BaCl_2$ is not confirmed. An M centre is a complex of two spatially associated vacancies and trapped electrons. Due to the proximity of the two trapped electrons to one another, the overall trapping energy for the first activation is reduced. During TSL, one of these electrons may be liberated, resulting in two vacancies, with an electron trapped at one of these. This can be labelled as a M^+ centre for the purpose of this discussion. An unoccupied vacancy corresponds to an effective +1 charge, and therefore the M^+ centre will correspond to a relatively deep trap. However, as the sample temperature increases, the M^+ centre is expected to disassociate into a vacancy and F centre. The F centre will then empty

at the normal temperature for F centres. In this way, no additional peak is expected from the M^+ centre.

For Mg^{2+} doped $BaCl_2:Eu^{2+}$, it is expected that the Mg^{2+} will not create F_A centres since it does not change the local electrical environment when it substitutes for a Ba^{2+} ion. Therefore, the peak present in the LT-TSL could correspond to an intrinsic M centre in $BaCl_2$. In Li^+ doped $BaCl_2:Eu^{2+}$, the Li^+ ion does change the local electrical environment by introducing an effective -1 charge if it substitutes for Ba^{2+}. There also exists the possibility that due to its small size the Li^+ ion does not substitute directly but takes up an interstitial position within the lattice. In both cases, it is likely that the effect of M centre trap energies will be relatively large and this helps to explain the multiple peaks in the LT-TSL of the Li^+ doped material. Just as F centres can be modified by adjacent dopants to give F_A centres, we can expect a variety of perturbed M centres, with the multiple possible site geometries for anion vacancies and an associated anion or cation substituting dopant.

4.4.3 Summary of peak assignment

It is important to note that the discussed peak assignment is a working model that needs to be tested and developed further. Table 4-8 summarises the peak assignment discussed in sections 4.4.1 and 4.4.2.

The F and F_A centres are associated with peaks that are stable at room temperature, and therefore some or all of these are important for storage phosphor effect. For $BaCl_2:Eu^{2+}$ with no other doping or impurity it is expected that the F_4 site will be responsible for trapping charges during irradiation, as the F_5 site appears to be unfavourably populated. When an alkaline impurity is added, it appears that F_{A4} and F_{A5} sites are dominant for trapping charges, and this could have an effect on storage phosphor efficiency. This is because the F_A trap energies are lower than the associated F trap energies. For K^+, Rb^+ and Cs^+, this appears to move the main storage peak normally associated with the F_4 centre to a thermally unstable energy.

This would imply that after irradiation the trapped charges can thermally empty from the traps, removing the latent image on the imaging plate before read-out can occur.

Co-Dopant	Temperature of Peak Maximum (°C)	Assignment
none	135	F_4
none	190	F_{A5}
Li^+	140	F_4
Na^+	95	F_{A4}
Na^+	230	F_{A5}
K^+	75	F_{A4}
K^+	160	F_{A5}
K^+	250	F_5
Rb^+	60	F_{A4}
Rb^+	155	F_{A5}
Rb^+	245	F_5
Cs^+	100	F_{A4}
Cs^+	150	F_{A5}
Mg^{2+}	125	F_4
Ca^{2+}	130	F_4

Table 4-8: Summary of peak assignment for peaks above 0 °C.

Experiments need to be done using optical bleaching to see if different peaks bleach at different rates under different wavelength light. This is important to check whether the different traps (F_4, F_5, F_{A4} and F_{A5}) in a sample are excited differently during PSL at the wavelength used by readout machines (633 nm).

The assignment of M centres to the sub room temperature peaks need to be tested using more data sets. This means more samples measured using the low temperature method to discover any patterns, especially between dopants with the same charge (i.e. Na^+ and K^+).

For future HT-TSL experiments, it is worth noting that though the signal-to-noise is better when longer irradiation times are used, peak resolution appears to decrease due to broadening of the peaks. Though GCD techniques can deal with some peak overlap while still giving useful results, overall the improvement in signal-to-noise is not large enough to justify the longer irradiation times.

Chapter 5

Results and Analysis: Storage Efficiency of $BaCl_2:Eu^{2+}$ with Co-Dopants

5.1 Motivation

The purpose of the photostimulated luminescence (PSL) measurements reported here was to measure the storage efficiency of the $BaCl_2:Eu^{2+}$ phosphors and determine how this changes with the addition of supplementary dopants.

PSL measurements made on glass ceramics imaging plates containing $BaCl_2:Eu^{2+}$ nano or microcrystals made at VUW showed a variation in the PSL efficiency for the same radiation dosage. It was thought that impurities may be entering the $BaCl_2$ crystallites from the surrounding glass matrix, or from contaminants during preparation, and that these contaminants altered the PSL efficiency. To test if contaminants could have significant positive or negative impact on the PSL efficiency, a number of additionally doped $BaCl_2:Eu^{2+}$ samples were produced and the PSL signal compared to undoped $BaCl_2:Eu^{2+}$. The beneficial or detrimental effect of the different dopants is expected to be useful for the design of improved glass ceramic imaging plates.

5.2 Preparation

Samples were prepared into pellets to provide, as best as possible, a consistent surface area to be exposed to the PSL measurements as described in chapter 3. These pellets were held in an airtight sample holder during measurements to prevent sample degradation due to hygroscopic effects.

Samples were bleached before irradiation using a red-filtered 60 W tungsten bulb at a distance of 10cm, to empty any occupied electron traps. The red filter was used to remove any UV light which may have a photogeneration effect.

Irradiation time was 30 s with 50 kV, 20 mA x-rays. After irradiation, samples were transported to the PSL equipment under black cloth to avoid any ambient light causing recombination before the PSL is measured. The PSL experimental set up is described in chapter 3.

5.3 Results

The PSL measurements for the various samples are shown in figure 5-1. The curves are displayed on a single log plot to show the relative differences between the PSL due to different dopants.

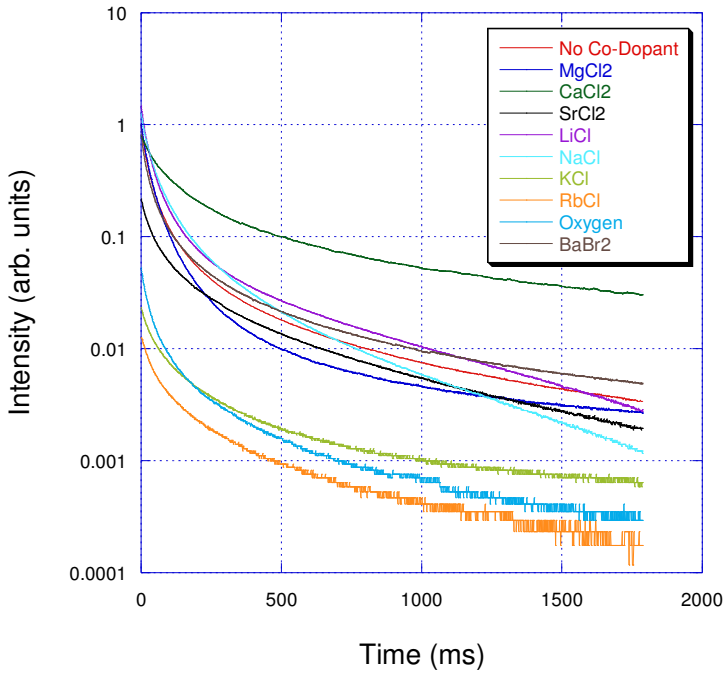

Figure 5-1: The PSL decay curves for $BaCl_2:Eu^{2+}$ co-doped with the labelled dopant.

Since none of the decays are linear on the log scale, the PSL process is not a single exponential. This is not surprising as it is expected that there will be several different electron traps within the material, both thermally stable and containing electrons to liberate during the stimulation process, and thermally unstable which may trap liberated electrons for a relatively small amount of time without photostimulation.

To analyse the data as it applies to storage phosphor operation requires integration of the area under the curve, so as estimate the total light output for a particular dose. To do this requires either curve fitting to get extract an approximation to the total area when the time axis is extended to infinity or approximating the total area by the measured area, and assuming that the truncation of the data does not cause significant errors.

For the curve fitting procedure, a number of exponentials are fitted to the data using the following formula:

$$I = \sum_i A_i \exp\left(-\frac{t}{\tau_i}\right) \tag{5-1}$$

Here the summing is over each individual exponential and A_i represents the t = 0 intensity due to term i and τ_i is the time constant for the decay of the ith exponential.

Integration shows that the total area under the decay curve is given via the fitted parameters as:

$$Area = \sum_i A_i \tau_i \tag{5-2}$$

The main problem with the fitting exponentials method of obtaining the total emission of the phosphor is that the number of exponential decays present can be ill defined.

Table 5-1 shows the results of a calculation of the total output for each dopant, averaged over each measurement made for the particular dopant.

Dopant	Area for Given Number of Exponentials		
	2	3	4
None	1.00	1.00	1.00
Li^+	1.15	1.18	1.21
Na^+	1.53	1.50	1.48
K^+	0.043	0.035	0.033
Rb^+	0.021	0.017	0.015
Mg^{2+}	0.31	0.27	0.26
Ca^{2+}	0.57	0.58	0.58
Sr^{2+}	0.84	0.82	0.82
Br^-	0.70	0.69	0.70
O^{2-}	0.051	0.043	0.040

Table 5-1: Calculated PSL output using equation 5-2, with 2, 3 or 4 exponentials fitted to the decay curve, normalised to the non co-doped case.

The other method for estimating the total light output of the sample is to simply calculate the area under the curve obtained from the experiment and not using any extrapolation methods to account for the tail. This method will tend to give an error roughly inversely proportional to the difference between initial and final measured values for the light intensity.

$$Area = \Delta t \sum_i y_i \tag{5-3}$$

Using this technique, the following values for the total emission are obtained. It is important to remember that these values will underestimate the total light output possible from the sample.

Dopant (+Eu^{2+})	Area
None	1
Li^+	1.21
Na^+	1.48
K^+	0.039
Rb^+	0.028
Mg^{2+}	0.27
Ca^{2+}	0.52
Sr^{2+}	0.82
Br^-	0.68
O^{2-}	0.050

Table 5-2: Calculated PSL output using equation (5-3).

This technique for calculating the area under the graphs gives the same results as the exponential fitting experiments within uncertainties. It is more important to note that the goal of the project was to check relative improvements or decline of the PSL effect when compared to undoped $BaCl_2$:Eu^{2+} so absolute values are not important.

5.4 Discussion

The results suggest some interesting results, especially for the introduction of alkaline impurities. The smaller alkaline ions of Li^+ and Na^+ showed an improved PSL efficiency, though this is relatively small; in both cases less than a 50%

improvement. In contrast to this, the larger alkaline ions of K^+ and Rb^+ showed a very significant reduction in PSL efficiency, reducing to less than 4% of the PSL efficiency of undoped $BaCl_2:Eu^{2+}$.

The alkaline earth ions show small reductions in PSL efficiency, which was most notable for the smallest ion in the group of Mg^{2+}. The overall efficiency increases going down the periodic table group, though this was only measured for three of the group members.

It is worth comparing the PSL results to the TSL results from chapter 4. The TSL measurements of alkaline doped materials, especially K^+ and Rb^+ showed a large peak at a temperature less than 100 °C. This peak would not be expected to be thermally stable at room temperature. This could mean that the main trap being populated during irradiation is this low temperature peak, and it is emptying between irradiation and PSL measurement, resulting in a much reduced output for K^+ and Rb^+ doped $BaCl_2:Eu^{2+}$. The Na^+ doped material has a higher peak temperature which could mean the peak is relatively stable at room temperature, and so the F_{A4} centre may be a good storage centre, resulting in the improved PSL for Na^+. This could be tested by running the PSL experiment below room temperature, and seeing if this significantly improves the PSL of K^+ and Rb^+ doped material.

Li^+ doped material also shows an improvement in PSL. The TSL shows no peak at 100 °C where an F_{A4} peak might be expected, or any between room temperature and 100 °C, which is either a result of the F_{A4} centre not existing or being of comparable energy to the F_4 centre, thus showing up as one peak. The reason for the absence of a F_{A4} centre could be due to the small size of the Li^+ ion, resulting in it being unable to substitute for Ba^{2+}.

The loss of PSL activity for K^+ and Rb^+ suggests that the higher temperature peak present in the TSL measurement, associated with a F_{A5} centre, is not optically active at the 633 nm wavelength of the stimulating light. This can be tested using TSL, and

bleaching the sample before making the TSL measurement. If the peak exists after bleaching it can be assumed it is not photosensitive.

The PSL of Mg^{2+}, Ca^{2+} and Sr^{2+} doped samples show 20 – 80% decreases in PSL efficiency when compared to undoped $BaCl_2:Eu^{2+}$. The cause of this is difficult to determine from TSL data, as these samples tend to show the same peak structure as undoped material.

The other dopants of Br^- and O^{2-} have not been measured using TSL, and so it is not possible to draw conclusions in these cases. It is interesting that the O^{2-} doped material appears to have a marked decrease in PSL efficiency, when O^{2-} is considered beneficial in other phosphor compounds for increasing PSL efficiency, for example $BaFBr:Eu^{2+}$ [1]. Br^- appears not to change the efficiency much, reducing it slightly when compared to undoped material. This could also be due to shifts in the optimal photoactivation wavelength, though this should be measured also.

Chapter 6

Conclusions and Future Work

This thesis describes the development of existing TSL equipment to improve versatility and accuracy, the characterisation of electron traps within $BaCl_2:Eu^{2+}$ and the effect of additional dopants on the trap properties. The effect of these dopants on the PSL efficiency of the $BaCl_2Eu^{2+}$ phosphors was also examined, with the goal of identifying impurities which could be used to improve the storage phosphor effect, while identifying which impurities might cause a detrimental effect

The various different experimental techniques used in this work are described in chapter 3. The existing TSL equipment ("HT-TSL") underwent redesign during this project to increase the accuracy by improving the linearity of the heating process and reducing the delay between successive optical measurements, and the versatility by modifying the operating range to allow for sub-ambient temperature TSL measurements. The PSL experiment was designed so that valid inter-sample comparisons could be made to compare the PSL efficiency of the different samples. This was done by standardising the irradiation dose given to the samples and the surface area and volume of the samples. Finally, a new TSL rig ("LT-TSL") was designed to allow for very low temperature TSL measurements (25 K – 280 K). Since the irradiation could not be done at these temperatures, a new technique was employed using a phototransfer process to populate the traps that were not thermally stable at room temperature and therefore not populated during sample irradiation.

There are still further improvements that could be made to the high temperature TSL equipment. Though the software and temperature control circuitry was modified to allow for sub-room temperature measurements, making these measurements is

reasonably difficult. Currently, cooled gas is passed over the sample to reduce the sample temperature, but the result is that the maximum temperature of the sample is approximately 150 °C when both gas flow and the heating element are on. This could be improved by redesigning the sample holder encasement, where the walls are cooled rather than the sample directly, so that the gas flow is not present directly over the sample. This should reduce the required heating power and allow for TSL measurements over most of, if not the entire, temperature range in one experiment without introducing transients.

Chapter 4 contains a TSL study of $BaCl_2:Eu^{2+}$, and the effect of additional dopants on the electron traps within the material. The two main goals of this chapter were to characterise if possible the different charge traps in the material, with special interest to the traps which are important in the storage phosphor application, and whether there are room temperature unstable traps which could be responsible for the afterglow effect.

Several different room temperature stable traps were found to be present in $BaCl_2:Eu^{2+}$, and these were sensitive to any additional dopants that were present. For the measurements made in this work, the F_5 peak reported in the literature [26] was rarely observed, though the F_4 peak was a common feature (refer to section 4.4 for explanation of peak defect labelling in this work). For alkaline doped materials, it was found that the peaks were shifted to lower temperatures by significant amounts, and it was suggested this is due to the formation of a majority of F_{A4} and F_{A5} traps, which are expected to have a lower energy than the respective F_4 and F_5 traps.

It was found that there are probably traps within $BaCl_2:Eu^{2+}$ when additionally doped with Li^+ which would contribute to the afterglow that was seen in the LiBO glasses produced at VUW. This experiment was performed using the LT-TSL rig which was custom designed for this work. LT-TSL measurements should be performed on $BaCl_2:Eu^{2+}$ with no additional dopants to check which peaks in the glow curve are due to Li^+ doping and which are intrinsic to the material. It is likely

that the peaks present in $BaCl_2:Eu^{2+}$, Mg^{2+} are the same as those that will be present in $BaCl_2:Eu^{2+}$ since Mg^{2+} and Ba^{2+} have the same charge, but this should be confirmed experimentally.

Another dopant to test is oxygen, present as the O^{2-} ion. This is because when grown in a LiBO glass, there is ample opportunity for oxygen ions to be taken up into the $BaCl_2$ crystals. It is difficult to introduce oxygen doping in a controlled fashion as barium based crystals containing oxygen (BaO and $BaNO_3$) melt at high enough temperatures to cause sample loss due to the evaporation of the $BaCl_2$. A method was trialled for this work of passing H_2O over a sample of $BaCl_2:Eu^{2+}$ whilst it was molten, with O^{2-} uptake being the desired result. This method was not tested to any extent and more research should be done to test its efficacy.

The working model for the structure of electron traps in $BaCl_2$ put forward in this work needs to be tested further. An important check that needs to be made is the optical sensitivity of the F_{A5} centre, which is apparent in alkaline doped material. If this trap is not optically active, then this would help to explain the lack of PSL in the K^+ and Rb^+ doped material, as the F_{A4} centre in these samples appears to be thermally unstable at room temperature. Optical bleaching experiments are relatively straight forward to do with the HT-TSL rig, as the optical fibre cable is capable of directing bleaching photolysis (either from high powered LEDs or from a monochromater)**.** After photo bleaching, if the F_{A5} peak is still present in the TSL glow curve, then the F_{A5} trap is not photoactive at the bleaching wavelength.

Further HT-TSL experiments should be done on the $BaCl_2:Eu^{2+}$ samples with different additional dopants using different ramp rates. This is simply to improve the understanding of the $BaCl_2$ defect structures and to obtain more accurate values for the trap properties. Currently only samples of $BaCl_2:Eu^{2+}$ with no additional doping, or Ca^{2+}, Mg^{2+}, Li^+ as the additional dopant have been measured using multiple ramp rates, and these should be extended to other co-dopants considered here. It seems that there are measurable changes in the F_A peaks in alkaline doped material with

different ramp rates, and it would be particularly helpful given the interest in ZBLAN:$BaCl_2$:Eu^{2+} storage phosphors where sodium doping is a real possibility, to make measurements on these, starting the TSL ramp from approximately 0 °C to ensure no thermal depopulation is occurring to the low temperature peak. It should also be noted that the 4 minute x-ray dose applied to the samples, though giving good signal to noise, seemed to cause some peak overlap which made GCD analysis difficult when compared to the measurements made with a 45 second dose. It is suggested future work is done with a smaller x-ray dose, between 45 and 60s. This is because the GCD technique appears to better handle increased noise than peak overlap.

The peak identification with particular defect structures should be further explored, as the defects within $BaCl_2$ are expected to be more complex than the alkaline halides from which the majority of defect research has been done. There are spectroscopic techniques for exploring defect structure in the alkaline halides such as ESR which may be applicable to $BaCl_2$ and this should be examined further.

The change in PSL efficiency of $BaCl_2$:Eu^{2+} with the introduction of different dopants was tested in chapter 5. Only two dopants gave an improvement in PSL (Li^+ and Na^+) though this was less than 50% in each case. The +2 cations showed a decrease in total output between 20% and 80%. Interestingly, both K^+ and Rb^+ showed a remarkable decrease in PSL efficiency. This could be due to the main PSL trap in $BaCl_2$ being moved to lower energies by the dopant, and therefore becoming thermally unstable at room temperature, resulting in depopulation before PSL measurements are made. Clearly these are ions to be avoided in any new glass ceramic design for storage phosphors based on barium chloride crystals.

Chapter 7

Appendix A

The CD included with this work contains the necessary files to run the TSL equipment at VUW. The files should be copied into the MATLAB working folder, often '\MATLAB\work'. The software represents a major overhaul of the TSL software that occurred during the term of this work, with contributions made to both the software improvements and the testing of the new system.

Appendix B

Included here is a copy of a paper published in the journal "Review of Scientific Instruments", titled "Thermoluminescence Apparatus Using PT100 Resistors as the Heating and Sensing Elements" [24].

The paper is a summary of the TSL equipment designed at VUW.

Thermoluminescence Apparatus Using PT100 Resistors as the Heating and Sensing Elements

J. W. Quilty,[1] J. Robinson,[1] G. A. Appleby,[2] and A. Edgar[1]
[1]*School of Chemical and Physical Sciences, Victoria University of Wellington, P.O. Box 600, Wellington, New Zealand.*
[2]*Department of Electronic Materials, Institute of Materials Science, Darmstadt University of Technology, Darmstadt 64287, Germany.*

A novel apparatus for obtaining thermoluminescence glow curves is described. Two standard PT100 precision resistors, which have a well-known dependence of resistance on temperature, are connected back-to-back to provide a sensing and heating element. The resulting hot finger has very low thermal mass, is non-reactive and inexpensive. With dry nitrogen gas-flow cooling, an operational range of -50 to 450 °C is achievable. A tailored control circuit which is easily calibrated drives the heating element and temperature ramps are implemented in software. The simple design permits the use of modularly interchangeable hot fingers for rapid measurement of many samples.

I. INTRODUCTION

Thermoluminescence is a well-established technique which has stimulated a number of instrument designs suited for applications in radiation dosimetry, geophysics, archaeology and biology (Luff and Townsend, 1993; Jones et al., 1992; Piters et al., 1993; Bibicu et al., 1996; Rhodes et al., 2000; Molina et al., 2002; Lyamayev, 2006). The crucial element of all thermoluminescence instruments is the heating element, typically a planchet or block heater. While the planchet heater has the advantage of a fast thermal response, both planchet and block heaters present design challenges in obtaining uniform temperature distribution across the sample and, as the temperature sensor is not in direct contact with the sample, precise sample temperature measurements during the heating cycle (Bibicu et al., 1996). Commercial thermoluminescence instruments offer good performance for typical applications in dosimetry, but are not necessarily appropriate in design or cost for fundamental research.

Faced with exactly these problems in measuring the thermoluminescence glow curves of x-ray storage phosphors, we developed a high-performance cost-effective thermoluminescence rig based around standard PT100 precision resistors as the heating and sensing elements. The resulting apparatus is driven by a hardware proportional-integral controller with the thermal ramp controlled in software by computer. The instrument also permits the measurement of x-ray induced photoluminescence at an arbitrary temperature within the operational range of −50 to 450°C during sample irradiation.

Measurement from temperatures below room temperature was a specific requirement of the design because determination of the thermoluminescence properties of x-ray storage phosphors at ambient temperature are often complicated by afterglow following irradiation. The afterglow originates from shallow traps which are of interest in themselves. Irradiation at, and measurement of glow curves from, room temperature cannot yield consistent measurements of low-lying traps. Reducing the sample temperature before irradiation and measurement permits characterisation of these traps.

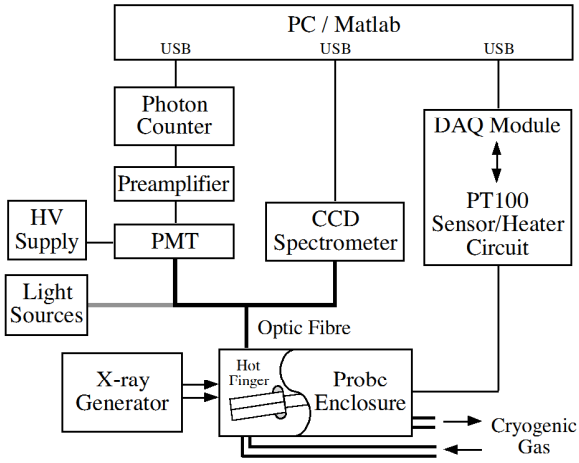

FIG. 1 System diagram of the thermoluminescence rig.

II. INSTRUMENTATION

The thermoluminescence rig is comprised of three elements: the heating and temperature sensing hardware, the detectors used to measure the luminescence and a computer to control and record the thermoluminescence glow curves in software. A system diagram is shown in Fig. 1 and the components are described below.

A. Sensing and Heating Element

The heater and sensor are miniature PT100 resistors of dimensions (width × length × height) 2 × 5 × 1 mm which are combined into a single interchangeable hot finger, shown in Fig. 2. The sample is placed on top of the

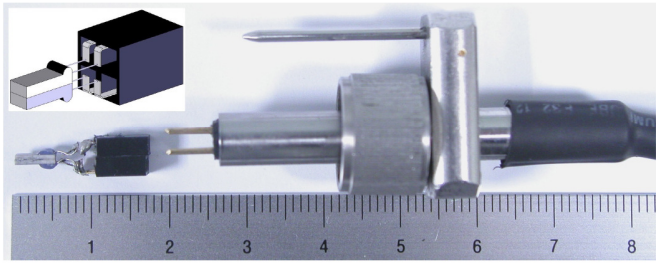

FIG. 2 PT100-based hot finger configuration. Two PT100 resistors are glued back-to-back with thermally conductive paint and soldered to modified 2.54 mm (0.1 in) pitch jumper connector blocks for use with the heater-sensor mount. The mount secures the hot finger for irradiation with the x-ray generator. Inset: schematic of the interchangeable PT100 hot finger.

sensor, which gives 10 mm^2 maximum available sample area. The relatively small sample area poses no significant problems for the measurement of storage phosphor materials, which typically exhibit strong thermoluminescence signals after x-ray irradiation. Silicone oil is used to ensure good thermal contact between the sample and the sensor; both powdered and solid samples may be mounted in this manner. This configuration possesses the distinct advantage that the sample and temperature sensor are in direct thermal contact, unlike the typical planchet heater in which a thermocouple is spot-welded to the bottom of the heating element and may not be at the same temperature as the sample due to thermal gradients and inhomogeneity across the sensor-heater-sample interfaces.

The hot finger is plugged into a simple mount and placed within a holder which is designed specifically for use on a Philips PW 1720 x-ray generator. The holder also provides an enclosed area with inlet and exhaust apertures to allow cooled nitrogen gas to be circulated over the heater-sensor head. Nitrogen gas is obtained from a high purity gas cylinder and passed through a copper coil which is immersed in pre-cooled isopropyl alcohol. The cooled gas is introduced to the heater-sensor head through the sample holder gas inlet. The gas flow also functions to reduce the hydration of hygroscopic samples.

With this configuration, static temperatures as low as −50°C are easily obtainable. The maximum temperature is dictated by both the choice of power supply and the hot finger thermal dissipation at high temperatures. With a little over 10 W power delivered to the heater, a maximum temperature greater than 450°C was achievable, giving an operational range of 500°between −50 and 450°C. Over this range, the PT100 sensor resistance changes by 183.87 Ω, from 80.31 Ω at −50°C to 264.18 Ω at 450°C. Due to the low thermal mass of the PT100 resistors, the system exhibits fast thermal response, taking less than 90 seconds to cool from 450 to 30°C without gas-flow cooling.

B. Digital Acquisition Unit

A Digital AcQuisition unit (DAQ) provides the necessary interface between the computer and the heater-sensor hardware, to read the voltage drop across temperature sensor and write the temperature setpoint voltage for the heater. The choice of DAQ influences some aspects of the sensor-heater circuit design, as noted in the following section.

A National Instruments USB-6900 DAQ was selected as a compact, readily available and cost-effective DAQ with up to 8 analog inputs. The temperature sensor resolution obtained with this DAQ varies from 0.028C/bit to 0.033C/bit between −50 and 450°C. The remaining analog input ports of the DAQ are connected to read the voltage at test points in the circuit for the purpose of self-diagnostic tests in software.

The setpoint voltage corresponding to the desired temperature, provided by the DAQ's analog output, gives a setpoint temperature resolution of 0.1°C over the operational range.

C. Sensor-Heater Circuit

Thermal control is provided by a calibrated proportional-integral circuit which compares the difference between a temperature set-point, generated in software and provided from the analog output port of the DAQ, and the temperature of the PT100 sensor. The difference controls a 30 V power supply connected to the PT100 heater element.

Figure 3 shows the circuit diagram for the sensor-heater hardware. The 2.5 V precision reference voltage from the DAQ, buffered through the U9 voltage follower, is used in the three branches of the circuit. From top to bottom these are (a) the sensor driving branch (b) the heater driving branch and (c) the sensor DAQ measurement branch.

1. Sensor Driving Branch

This part of the circuit is responsible for temperature measurement using the PT100 sensor resistor. The inverting amplifier U7 places a constant current of 2.083 mA (2.5 V/1.2 kΩ) through the PT100 sensor, which is connected as the feedback resistor across U7. Using an estimated dissipation constant of 0.25°C/mW for the PT100 resistor pair in the sample mount in air (IST AG), the self-heating due to the sensor current is 0.05°C at -50°and 0.16°C at 450°C.

The voltage drop across the PT100 sensor is measured by op-amps U4, U5 and U8 configured as a standard differencing amplifier (Horowitz and Hill, 1980) with unity gain, the output of which, at Test Point 1 (TP1), is provided to the heating and DAQ measurement branches of the circuit. Separate sensor current and voltage wires

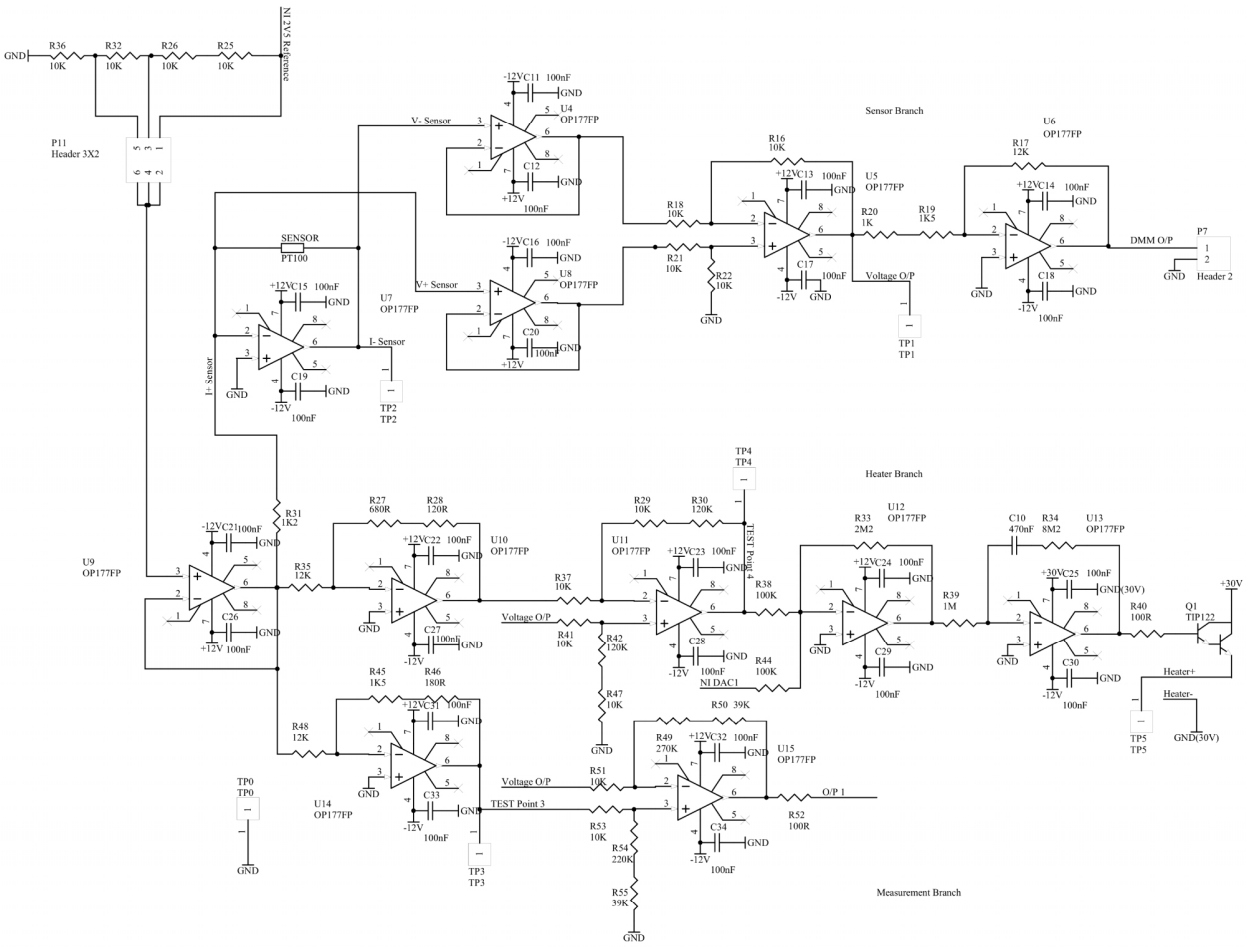

FIG. 3 Circuit diagram of the heater driver and temperature sensor module.

are used to eliminate stray resistances from the cabling as much as possible. The final op-amp in the sensor driving branch, U6, is configured as an inverting amplifier with gain $10/2.083 = 4.8$, thus scaling the sensor voltage such that 1 V corresponds to a sensor resistance of 100 Ω. This voltage is made accessible external to the unit at the DMM O/P port shown in Fig. 3, permitting independent direct reading of the PT100 resistance.

2. Heater Driving Branch

Thermal control of the sensor and sample are provided by the heater branch, which measures the difference between the sensor voltage and the setpoint voltage from the DAQ unit's analog output port and sets the heater voltage as appropriate.

Op-amps U10 and U11 convert the sensor voltage to lie within the range 0–(−5) V for comparison with the 0–5 V analog output from the DAQ. U10 provides a reference offset voltage equal to the voltage drop across the sensor at −50°C. This is is compared with the sensor voltage obtained from the sensor branch by op-amp U11, configured as a differential amplifier of gain 13, thus giving an output voltage at Test Point 4 (TP4) which is the sensor voltage scaled to the range 0–−5 V. Op-amp U12 is configured as a summing amplifier of gain 22, the inputs to which are the scaled sensor voltage and the DAQ analog output voltage representing the temperature setpoint; when the sensor temperature and the setpoint are the same, the output of U12 is 0 V.

Combined proportional-integral control is provided by U13, with the 0.47 s time constant in the feedback loop chosen based on the experimentally-determined response time of the sensor head. For ramp rates up to 5°C/s, overshoot and ringing due to the lack of differential control is less than ±0.05°C (see Section III Discussion).

The proportional-integral output voltage drives a TIP122 Darlington transistor Q1 which acts as a power amplifier to control the heater current. The heater power supply provides +30 V maximum across the PT100 heater resistor, giving a maximum current around 370 mA and maximum power just under 11 W. A separate ground is used for the heater power supply to avoid

the problem of ground loops superimposing a signal from the heater on the temperature sensor voltage.

3. DAQ Measurement Branch

This branch, comprised of op-amps U14 and U15, is used to offset and scale the sensor voltage for connection to the DAQ analog input. The inverting amplifier U14 produces an offset reference voltage of which is compared to the sensor voltage from the sensor branch by the differential amplifier U15. The differential amplifier gain gives an output voltage range of -5 to +5 V for the temperature range -50 to 450°C. This voltage is connected directly to the first analog input of the DAQ for readout by the software.

D. Optical Detectors

Two detectors were used with the hot finger: a photomultiplier tube (PMT) and a charge-coupled device (CCD) spectrometer. In our case, the PMT used was a Peltier-cooled Electron Tubes Limited 52 mm 9558QB PMT with a Stanford SR445A preamplifier and a Stanford SR400 two-channel gated photon counter, while the CCD spectrometer was an Ocean Optics USB2000 optimised for fluorescence measurements. The photomultiplier possesses excellent sensitivity over a wide wavelength range, but provides only a wavelength-integrated measurement. Wide band filters were used with the PMT to remove unwanted signal due to black body radiation at high temperatures. In contrast, the CCD provides a wavelength-resolved measurement over 340–1025 nm at a resolution (full width at half maximum) of 8 nm, but is about 100 times less sensitive than the PMT. A typical result obtained with the USB2000, from an x-ray storage phosphor $BaMgF_4:Eu^{2+}$ after x-ray irradiation at 50 kV/20 mA, is shown in Fig. 4.

An optic fibre was used to pipe the thermoluminescence signal to the detectors and permits the interchangeable use of one or, with the use of a bifurcated fibre, both detectors simultaneously. It also provides a desirable thermal and chemical isolation between the detectors and the sample. Typically, a single B&W Tek FPC Series Fibre Patch Cord of length 1.5 m, diameter 1 mm, numerical aperture 0.22 (field of view 25°) and rated for UV was used with the system. The optimal fibre-to-sample distances for sample extents 3–5 mm are thus 7–11 mm. Similar to previously described thermoluminescence apparatus using optic fibre coupling (Rhodes et al., 2000), there is no net advantage to using coupling optics between the sample and the fibre.

E. Photostimulation and Photobleaching Capability

The bifurcated optic fibre also permits the optical connection of a light source to the sample for either photostimulated luminescence measurements or photobleaching. This system was tested with two types of light source: high-intensity light emitting diodes (LEDs) and a miniature 1/4 metre focal length monochromator with a high-intensity incandescent light source. Philips Luxeon high-power LEDs of wavelength 470, 530, and 625 nm and spectral width at half peak maximum of 20–35 nm (Philips Lumileds) were typically used for selective trap photobleaching.

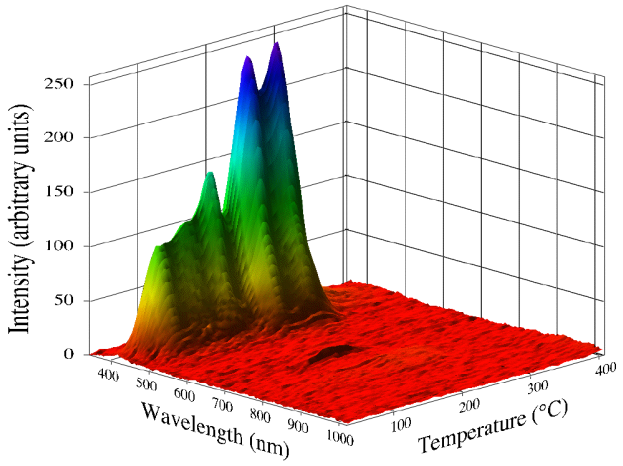

FIG. 4 The thermoluminescence glow surface of the x-ray storage phosphor $BaMgF_4$ obtained with the USB2000 spectrometer.

Measurement of photostimulated luminescence is possible with either of the PMT or CCD detectors, with a suitable filter at the detector end of the fibre necessary to remove the stimulation signal. Photobleaching does not require simultaneous detection and there is no requirement for optic filtering at the detector.

F. Control Software

Software running on a standard PC controls the heating ramps and measurement of the sample temperature and thermoluminescence. The routines were implemented in MatLab, but there is no reason why the software could not be implemented in a lower-level compiled language. The USB-6009 DAQ controlling the heater-sensor hardware was connected via the USB interface, while the Stanford SR400 Photon Counter and Ocean Optics USB2000 spectrometer were controlled via serial interfaces connected to the PC with USB-to-serial converters; the instruments were addressed in software by use of the NI-DAQmx drivers and the serial interface driver provided by the MatLab Instrument Control Toolbox.

Controlling the temperature ramp from software provides significant advantages in flexibility of the measurement and in a simpler sensor-heater circuit than a microcontroller-based system. A drawback of this approach is that the relatively slow execution speed

and single-threaded execution of the MatLab routines pose problems in the production of smooth temperature ramps. These problems were addressed by updating the temperature setpoint from a Matlab timer function and independently acquiring data from the PMT and CCD detectors. All operations run asynchronously. The temperature setpoint function may be called at any arbitrary interval; 0.1 s — a temperature update frequency of 10 Hz — was found to be an adequate update rate for temperature ramps up to 5°C/s, the maximum ramp rate tested. The temperature ramp setpoint is calculated adaptively based on the time of update execution as the period between executions can not be guaranteed to match the desired period due to Matlab's single-thread only execution environment.

Steady-state temperatures initially achieved for a given setpoint were offset by up to -1 to +1°C over the operational temperature range of -50 to 450°C due to minor residual non-linearity of the instrument. A quasi-steady-state calibration curve was obtained by running a temperature ramp at a very slow ramp rate and calculating the deviation from the setpoint. A cubic-spline interpolation of this calibration curve was then used as a lookup table to apply an appropriate offset to the setpoint in software. The calibrated steady-state deviation from the desired temperature was found to be better than ±0.05°C.

The routines were written to be modular, permitting their use in MatLab scripts. Experimental profiles involving heating or cooling to specific temperatures, holding the sample temperature constant for an arbitrary time, waiting for the thermoluminescence signal to fall below a specific level, as well as repeated temperature ramps with measurement, are thus easily constructed. In common with some previous instrument designs (Molina et al., 2002; Lyamayev, 2006), the production of arbitrary temperature ramps for more sophisticated glow curve deconvolution, such as the fractional glow technique, is also possible.

III. DISCUSSION

To ensure that the instrument provides an accurate measurement of thermoluminescence glow curves, comparison of glow curves measured from a standard thermoluminescence dosimetry material with previously published curves is advisable and in this respect the LiF-based TLD-100 dosimetry material is a natural choice. A glow curve obtained from a powdered sample of TLD-100 after irradiation with x-rays, generated at 50 kV/20 mA and filtered through the 0.65 mm aluminium front face of the probe mount, is shown in Fig. 5. This curve shows good agreement with a TLD-100 glow curve measured over a wavelength range of 410–430 nm with an optical filter by Yazici *et al.* (Yazici et al., 2001). The most intense TLD-100 peak at 215°C coincides within 2°C, the others within 5–7°, which is reasonable agreement given the differences in sample annealing, irradiation (x-ray vs. beta ray) and glow curve measurement (wavelength integrated vs. filtered for maximum transmittance at 420 nm). A thin solid sample of TLD-100 was also measured and the same glow curve obtained.

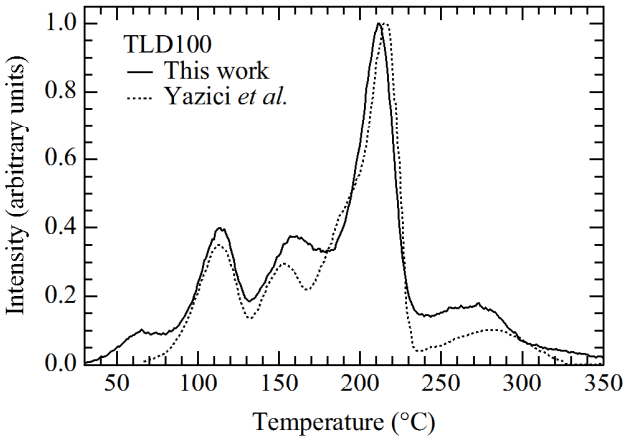

FIG. 5 A glow curve obtained from TLD100 (black line) compared with a glow curve measured by Yazici *et al.* (Yazici et al., 2001).

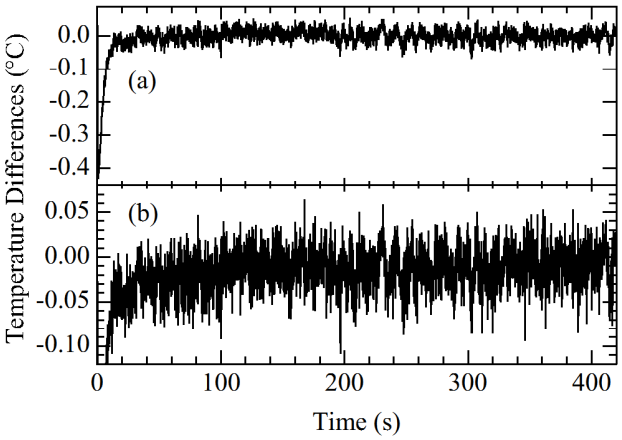

FIG. 6 (a) The residual difference between the temperature ramp and a linear fit (b) the deviation of the sensor temperature from the previous setpoint temperature.

It must be noted that the PT100 resistor itself exhibits a thermoluminescence signal, which visible in Fig. 4 as a weak peak, narrow in wavelength and broad in temperature, appearing just below 700 nm between 100 and 200°C. This weak instrumental artefact poses little problem in practice and, if necessary, can be completely removed by an appropriate optical filter or by coating the PT100 with a thin layer thermally conductive black paint, without adversely affecting the desired thermoluminescence.

The linear ramp performance of the instrument is shown in Fig. 6 for a 1°C/s ramp from 30 to 450°C. The detailed performance may be seen in the residual from a linear fit to the data between 20 and 420 s (50 and

450°C) and the temperature deviation from the previous setpoint measured at the time the setpoint is updated (every 0.1 s for this measurement). The sensor temperature initially lags the setpoint, due first to the unavoidable response time of the system and subsequently to the lack of differential control in hardware, but decreases to below −0.1°C within 8 s, corresponding to a sub-linear ramp temperature interval from 30–38°C. The slope of the linear fit gives the average ramp rate, and was found to be $1 \pm 5 \times 10^{-6}$ °C/s, while the residual of the linear fit shows an average deviation of only 0.02°C. Figure 6(b), the deviation from the setpoint, gives the instantaneous deviation of the sensor temperature from the linear setpoint ramp. After the initial sub-linear response, the linear ramp achieved falls below the ideal 1°C/s linear ramp by -0.01°C on average. This constant deviation is predominantly a function of the ramp rate, arising from the system response time, and averages -0.1°C for a 5°C/s ramp. The ramp performance of our system thus compares very favourably to that of conventional heater systems (Bibicu et al., 1996; Rhodes et al., 2000; Molina et al., 2002; Lyamayev, 2006).

For ramp rates greater than 1°C/s, where the sub-linear deviation progressively dominates the performance, a factor of three reduction of the deviation magnitude was easily obtained by adding an empirically-determined offset to the temperature setpoint at each update. The flexibility of the design also permits the use of the voltages from the sensor and diagnostic test points to provide more sophisticated manipulation of the instrument's performance.

IV. CONCLUSIONS

A high-performance instrument for measuring thermoluminescence glow curves has been developed, based around standard PT100 resistors as both sensing and heating elements. The linear ramp performance of the instrument is excellent, with typical average linear ramp rates within a few parts in 10^6 of the desired rate and a deviation of less than 0.05°C (less than 0.1%) over the majority of the ramp. While this particular instrument has been optimised for the measurement of thermoluminescence from x-ray storage phosphors, other materials which exhibit thermal or optically stimulated luminescence and may be suitably prepared for mounting on the hot finger can also be measured. The apparatus thus might also be usefully applied to the measurement of samples in the fields of geophysics and archaeology.

V. ACKNOWLEDGMENTS

The authors gratefully acknowledge the assistance of Mr. J. McClymont with the electronics hardware and Mr. S. Rogers with the preparation of the manuscript. This work was financially supported by the New Zealand Foundation for Research, Science and Technology.

References

B. J. Luff and P. D. Townsend, Measurement Science and Technology **4**, 65 (1993), URL `http://dx.doi.org/10.1088/0957-0233/4/1/011`.

S. C. Jones, J. A. Sweet, D. L. Fehl, B. R. Sujka, D. W. Vehar, and R. L. Westfall, Review of Scientific Instruments **63**, 4898 (1992), URL `http://dx.doi.org/10.1063/1.1143544`.

T. M. Piters, W. H. Meulemans, and A. J. J. Bos, Review of Scientific Instruments **64**, 109 (1993), URL `http://dx.doi.org/10.1063/1.1144423`.

I. Bibicu, S. Calogero, and L. Diamandescu, J. Phys. III France **6**, 475 (1996), URL `10.1051/jp3:1996135`.

M. W. Rhodes, S. Wanwilairat, T. Vilaithong, and W. Hoffmann, Review of Scientific Instruments **71**, 2053 (2000), URL `10.1063/1.1150577`.

P. Molina, M. Santiago, E. Caselli, M. Lester, and F. Spano, Measurement Science and Technology **13**, N16 (2002), URL `http://dx.doi.org/10.1088/0957-0233/13/1/405`.

V. I. Lyamayev, Measurement Science and Technology **17**, N75 (2006), URL `http://dx.doi.org/10.1088/0957-0233/17/12/N01`.

IST AG, *Datasheet for Platinum Temperature Sensors*, Innovative Sensor Technology IST AG, Industriestrasse 2, CH-9630 Wattwil, Switzerland (2003), URL `http://www.ist-ag.com/english/products/temp/platin.html`.

P. Horowitz and W. Hill, *The Art of Electronics* (Cambridge University Press, 1980).

Philips Lumileds, *Luxeon Star Technical Datasheet*, Philips Lumileds Lighting Company, 370 West Trimble Road, San Jose, California, 95131 USA (2006), URL `http://www.luxeon.com/products/luxeon`.

A. N. Yazici, Z. Öztürk, and M. Bedir, Turkish Journal of Physics **25**, 333 (2001).

References

1. Von Seggern, H., *Photostimulable x-ray storage phosphors: a review of present understanding*. Brazilian Journal of Physics, 1999. **29**(2): p. 254-268.
2. Rowlands, J.A., *The physics of computed radiography.* Phys Med Biol, 2002. **47**(23): p. R123-66.
3. Spaeth, J.M., *Recent developments in X-ray storage phosphor materials.* Radiation Measurements, 2001. **33**(5): p. 527-532.
4. Spaeth, J.M., et al., *X-ray storage phosphors.* Radiation Effects and Defects in Solids, 1995. **135**(1-4): p. 1-10.
5. Schweizer, S., et al., *Photostimulated luminescence in Eu-doped fluorochlorozirconate glass ceramics.* Applied Physics Letters, 2003. **83**: p. 449-451.
6. Appleby, G.A., et al., *Structure and neutron imaging characteristics of lithium borate–barium chloride glass-ceramics.* Nuclear Instruments and Methods in Physics Research A, 2006: p. 424–430.
7. Appleby, G.A., et al., *Lithium borate glass ceramics as thermal neutron imaging plates.* Current Applied Physics, 2006. **6**: p. 389-392.
8. Appleby, G.A., et al., *Photostimulated luminescence from $BaCl_2:Eu^{2+}$ nanocrystals in lithium borate glasses following neutron irradiation.* Applied Physics Letters, 2006. **89**: p. 101902-1 - 101902-3.
9. Appleby, G.A., *New materials for radiation imaging*, in *School of Chemical and Physical Sciences*. 2006, Vicotria University of Wellington: Wellington.
10. Shannon, R.D. and C.T. Prewitt, *Effective ionic radii in oxide and fluorides.* Acta Crystallographica, Section B: Structural Crystallography and Crystal Chemistry, 1969. **25**(Pt. 5): p. 925-46.
11. Brackett, E.B., T.E. Brackett, and R.L. Sass, *The crystal structures of barium chloride, barium bromide, and barium iodide.* The Journal of Physical Chemistry, 1962. **67**: p. 2132 - 2135.
12. Schweizer, S., et al., *Photostimulable defects in nano-crystallites in fluorozirconate glasses.* Phys. Stat. Sol. (a), 2005. **202**(2): p. 243-249.

13. Vij, D.R., ed. *Luminescence of solids*. 1998, Plenum Press: New York.
14. Bøtter-Jensen, L., S.W.S. McKeever, and A.G. Wintle, *Optically Stimulated Luminescence Dosimetry*. 2003, Amsterdam: Elsevier Science B.V.
15. Takahashi, K., et al., *Mechanism of photostimulated luminescence in europium(2+)-activated barium fluoride halide (BaFX, where X = Cl, Br) phosphors.* Journal of Luminescence, 1984. **31-32**(1): p. 266-8.
16. Von Seggern, H., et al., *Physical model of photostimulated luminescence of x-ray irradiated europium(2+)-doped barium fluoride bromide (BaFBr).* Journal of Applied Physics, 1988. **64**(3): p. 1405-12.
17. Iwabuchi, Y., et al., *Mechanism of photostimulated luminescence process in BaFBr:Eu2+ phosphors.* Japanese Journal of Applied Physics, Part 1: Regular Papers, Short Notes & Review Papers, 1994. **33**(1A): p. 178-85.
18. Sunta, C.M., et al., *A critical look at the kinetic models of thermoluminescence: I. First-order kinetics.* Journal of Physics D: Applied Physics, 2001. **34**(17): p. 2690-2698.
19. Sunta, C.M., et al., *A critical look at the kinetic models of thermoluminescence-II. Non-first order kinetics.* Journal of Physics D: Applied Physics, 2005. **38**(1): p. 95-102.
20. Randall, J.T. and M.H.F. Wilkins, *Phosphorescence and electron traps. I. Trap distribution.* Proc. Roy. Soc. (London), 1945. **A184**: p. 365-89.
21. Garlick, G.F.J. and A.F. Gibson, *The electron-trap mechanism of luminescence in sulfide and silicate phosphors.* Proceedings of the Physical Society, London, 1948. **60**: p. 574-90.
22. Kitis, G., J.M. Gomez-Ros, and J.W.N. Tuyn, *Thermoluminescence glow-curve deconvolution functions for first, second and general orders of kinetics.* Journal of Physics D: Applied Physics, 1998. **31**(19): p. 2636-2641.
23. McKeever, S.W.S., et al., *OSL sensitivity changes during single aliquot procedures: computer simulations.* Radiation Measurements, 1997. **27**(2): p. 75-82.
24. Quilty, J.W., et al., *Thermoluminescence apparatus using PT100 resistors as the heating and sensing elements*. 2007, AIP. p. 083905.

25. Bos, A.J.J., et al., *Effects of cooling and heating rate on trapping parameters in magnesium- and titanium-doped lithium fluoride (LiF:Mg,Ti) crystals.* Journal of Physics D: Applied Physics, 1992. **25**(8): p. 1249-57.
26. Secu, M., et al., *Photostimulated luminescence in $BaX_2:Eu^{2+}$ (X = Br, Cl) x-ray storage phosphors.* Radiation Effects and Defects in Solids, 2002. **157**(6-12): p. 957-962.
27. Houlier, B., *Localization of the F centers in barium chloride and bromide crystals.* Journal of Physics C: Solid State Physics, 1977. **10**(9): p. 1419-29.
28. Seitz, F. and D. Turnbull, eds. *Solid State Physics*. Vol. 16. 1964, Academic Press Inc.